Durham University

Durham E-Theses

High resolution X-ray diffraction and topography of Bragg case interferometers

Kokkonis, Panagiotis

How to cite:

Kokkonis, Panagiotis (1994) *High resolution X-ray diffraction and topography of Bragg case interferometers*, Durham theses, Durham University. Available at Durham E-Theses Online: http://etheses.dur.ac.uk/5841/

Use policy

The full-text may be used and/or reproduced, and given to third parties in any format or medium, without prior permission or charge, for personal research or study, educational, or not-for-profit purposes provided that:

- a full bibliographic reference is made to the original source
- a link is made to the metadata record in Durham E-Theses
- the full-text is not changed in any way

The full-text must not be sold in any format or medium without the formal permission of the copyright holders.

Please consult the full Durham E-Theses policy for further details.

Academic Support Office, The Palatine Centre, Durham University, Stockton Road, Durham, DH1 3LE
e-mail: e-theses.admin@durham.ac.uk Tel: +44 0191 334 6107
http://etheses.dur.ac.uk

DURHAM UNIVERSITY
Physics Department
(1994)

High Resolution X-ray Diffraction and Topography of Bragg case Interferometers

By Panagiotis Kokkonis

The copyright of this thesis rests with the author.
No quotation from it should be published without
his prior written consent and information derived
from it should be acknowledged.

A thesis submitted for the degree of Master of Science

No part of this thesis has been submitted for a degree elsewhere.
Except where acknowledged, the work is original.

ACKNOWLEDGEMENTS

I would like firstly to thank my parents, Γιαννης και Μαρια Κοκκωνη, for the continuous financial and emotional support without which this thesis would not have been possible. Δεν υπαρχουν λογια να σας πω "ευχαριστω".

I also like to express my gratitude to Prof. B.K.Tanner. It has been a pleasure for me to work under his supervision, in his very well organised group, and to have always prompt advice or help.

It is difficult to express the depth of my feelings to Csilla Szabo. Her contribution in my English as well as in the quality of my work and life in Durham was immeasurable.

I also owe to thank Dianne Hughes for all her help, Anna Tzovantari for her coffees, Panagiotis Giannakos for his hunting, Maria Farsari for her reference letters, Mary Kilitziraki for dancing with me, Adonis Giolas et al. for his sports influence, Despina Liakakou for her Indie films, Vicki Malandraki for her moral advises, Euaggelos Gianutsos for his late drings, Dr. E. Zoidis for laughing, Hara Toli for her printings, Theodora Ioannidou for her silence, and Mirela Cuculescu for her baklavas.

Finally I wish to acknowledge Dr. John Hudson and all the members of the research group and the technical staff for their support and friendship and my two teachers in the University of Ioannina for their trust in my potential.

Contents

Abstract

Symbols used

1 High Resolution X-ray Diffraction and Topography 1

1.1 Diffraction 1

a) Double Crystal (Axis) Diffraction 2

b) Triple Axis Diffraction 6

c) Applications 8

1.2 Topography 12

a) The Berg-Barrett method 13

b) The Lang's technique 13

c) Double Crystal Topography 16

d) Synchrotron Radiation Topography 19

2 Dynamical Theory 21

2.1 "Classical" Dynamical Theory 22

2.2 The Takagi-Taupin Equations 29

2.3 The Solution of Takagi-Taupin Equations 32

2.4 Results from the Dynamical Theory 35

3 Bragg case Interferometer 37

4 Experiments 46

4.1 Diffractions 48

4.2 Topography 53

5 Conclusions 58

Reference 62

Abstract

In the first chapter a brief overview of the principles and techniques of high resolution X-ray diffraction and topography is presented. Since the best analysis of the measurement is given by simulating the experimental results with predictions based on Dynamical theory, a short description of the Dynamical theory and its results has been attempted in the chapter 2. This is followed by an extended literature review of the Bragg case interferometer (chapter 3).

After that, the Double Crystal Diffraction and Topography experiments -chapter 4- have been described. Great effort had been made in fitting experimental and theoretically predicted curves.

The major target of the experiment was to detect change of the diffracted reflectivity resulting from "separator" layer thickness changes in an interferometer structure sample of InGaAs/AlGaAs on GaAs. No detectable variation appeared in the thickness of the "separator" layer showing that the layer thickness varied by less than one atomic spacing across the wafer. Discussion of the results is presented parallel to the description of the experimental work.

Symbols used

a_{o}	lattice parameters of the substrate
a_{r}	lattice parameters of the layer
$a_{//}$	lattice constant parallel to the interface
$a_{\perp}$	lattice constant perpendicular to the interface
m	lattice mismatch
m^{*}	effective mismatch
ν	Poisson ratio.
θ_{B}	Bragg angle
ϕ	angle between the substrate Bragg planes and the specimen surface plane
$\vec{D}$	electric displacement
χ	susceptibility
e	electronic charge
c	velocity of light
V	unit cell volume
F_{h}	structure factor
λ	wavelength
$\vec{k}$	wavevector
$\cos X_{mh}$	polarization factor
FWHM	full width at half maximum
ML	monolayer

Chapter 1

High resolution X- Ray Diffraction and Topography

High resolution X-ray Diffraction and Topography are now widely accepted techniques for the study of semiconductor devices. In the following pages will be presented a brief abstract about the techniques' principles and a short review of the methods.

1.1 Diffraction

In X-ray Diffraction experiments involve illumination of a sample with an X-ray beam. The incidence angle of the beam is varied around the Bragg angles of the layers of the sample in order to obtain the diffraction profile of the sample (rocking curve). As every layer has possibly a different lattice parameter the diffraction profile will contains several peaks. Every peak appears at the angle that satisfies the Bragg condition for the corresponding layer.

In single axis diffractometry the Full Width at Half height Maximum (F.W.H.M.) of the Bragg peak is determined by:

i) the collimator geometry,

ii) the source size and

iii) the spectral width of the characteristic line in the X-ray spectrum and it is also limited by the angular divergence of the incident beam. For these reasons the angular resolution becomes crude.

a) Double Crystal Diffraction

For high resolution double axis (or double crystal) diffractometry, D.C.D., is generally used. In the (+n,-n) parallel mode of DCD, (Figure 1.1) a reference crystal is used from the same material as the specimen. After placing the reference crystal parallel to the sample the result will be a *hkl, -h-k-l* reflection. In this case the diffraction is non dispersive in wavelength (or in energy).

Since the two crystals are parallel, made of the same material they will both be expected to satisfy the same Bragg conditions. That means, that if a beam fulfils the Bragg conditions for the reference crystal it will satisfy the same Bragg condition for the specimen crystal as well. In the same way different wavelengths will be diffracted under different conditions at different Bragg points. It is worth noting that even a small displacement of some arcsec from the angle that satisfies the Bragg condition might result in losing the peak.

In order to have a better resolution result a small range of the spectrum of X-rays has been used. The $K\alpha$ line is the one that is used as it maximises the intensity. According to the conditions mentioned before there is a simultaneous diffraction of the $K\alpha_1$ and $K\alpha_2$.

For non-uniform crystals the sample should be examined in the smallest possible parts. Therefore a smaller size of beam is needed in order to limit the broadening of the rocking curve. A slit can be placed between the two crystals for eliminating the $K\alpha_2$ line. When a perfect crystal is examined the slit does not affect the FWHM of the rocking curve. However, when crystals contain sub-grains of comparable size with the beam area the FWHM can be a significant function of beam size.

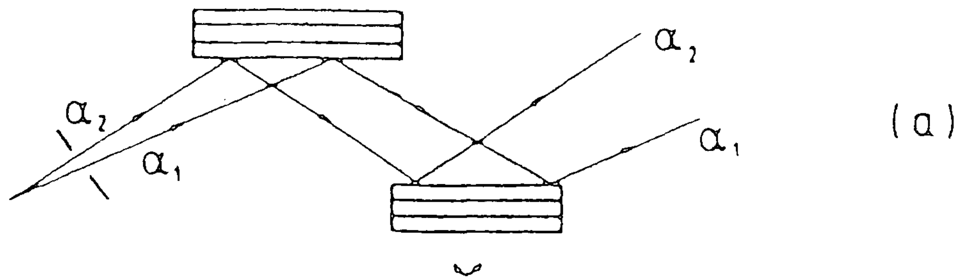

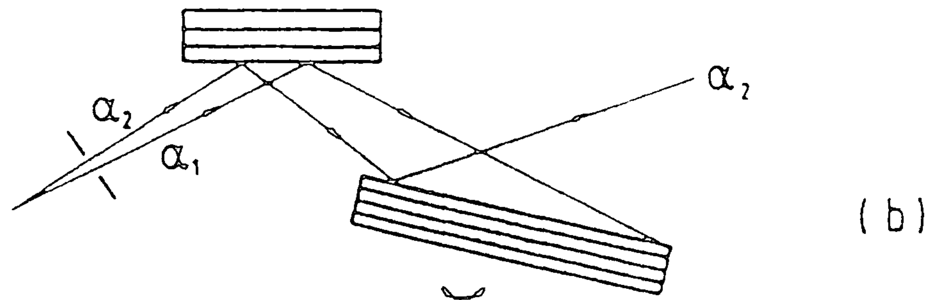

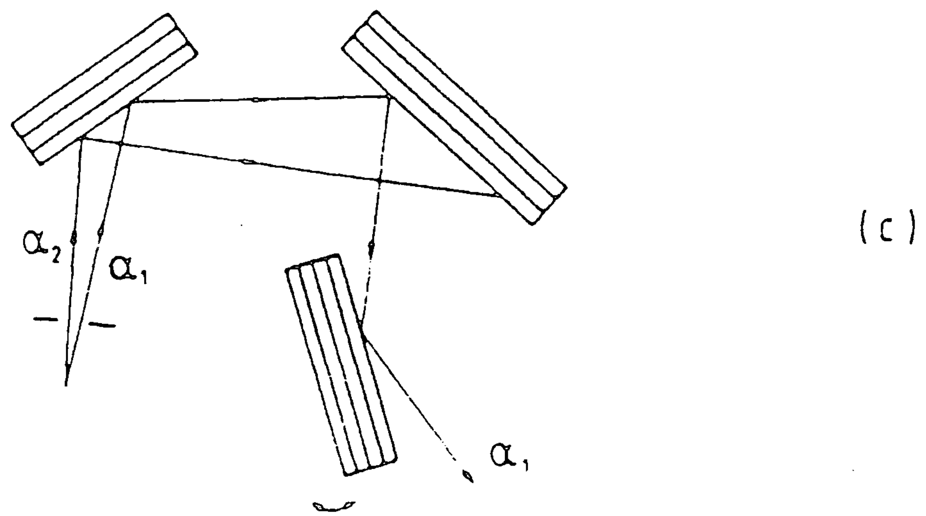

Figure 1.1:
(a) The *(+n,-n)* geometry double crystal arrangment with identical Bragg plane spacing for the reference and specimen.
(b) The *(+n,-m)* mode with different reference and specimen Bragg plane spacing
(c) The monochromatic *(+n,+n,-m)* setting.

(After Tanner)

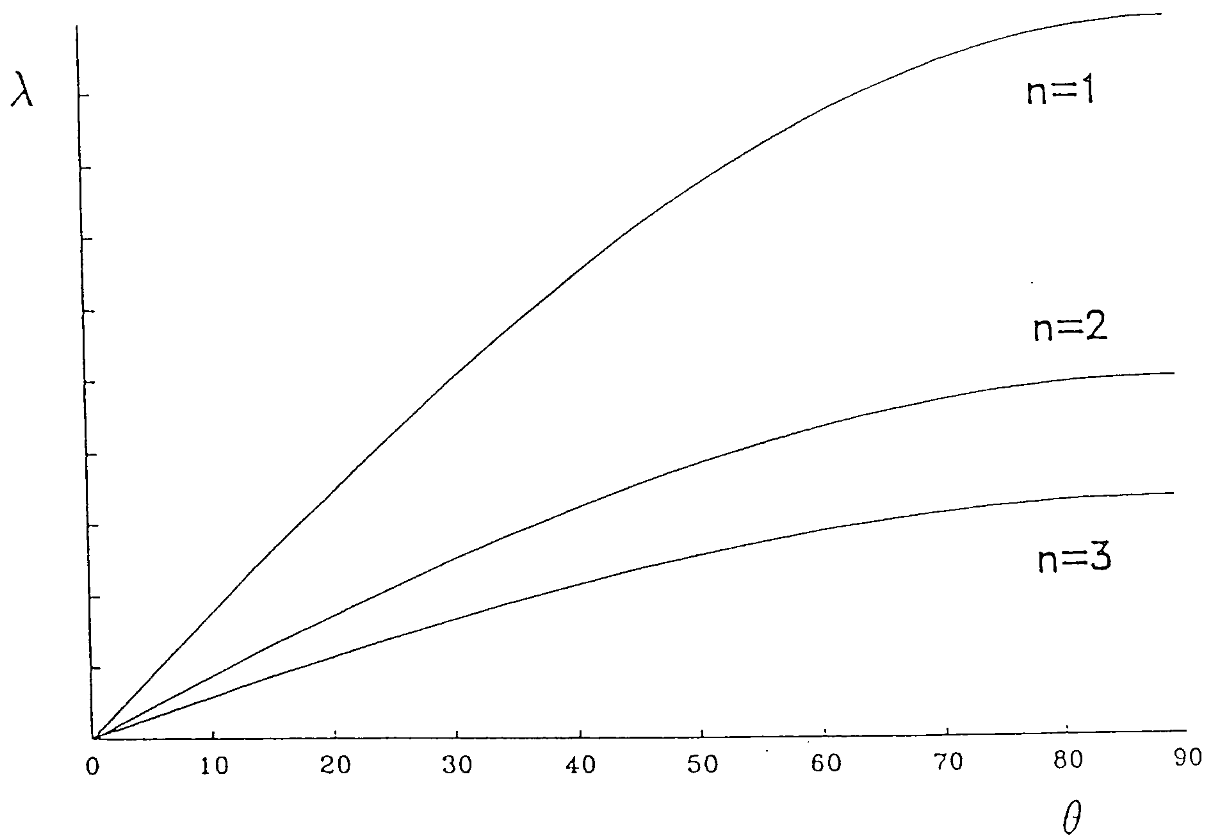

Figure 1.2(i):
The Bragg law for the first three orders of diffraction.

(After Hudson)

Finally, the growth of an epitaxial layer with different lattice spacing from the substrate leads to a mechanical bending of the wafer and to a curvature of the sample. Because of that curvature, a misorientation appeared at the lattice planes across the specimen; and that misorientation leads to a broadening of the rocking curve. The broadening therefore, is a function of the width of the beam in the incident plane.

In conclusion,

IF

the crystals are not curved,

the Bragg planes are perpendicular to the incidence (scattering) plane,[1]

and the crystals are perfect,

THEN

the FWHM is just the mathematical correlation, (of the two plane waves reflecting ranges) which may be calculated using dynamical theory.

It should be noted that the FWHM is a function of:

i) material

ii) reflection

iii) wavelength band

Typically FWHM is about 10 arcsec at 004 reflection λ =1.54Å in III-V compounds.

For finding the exact point of $K\alpha_1$ and $K\alpha_2$ we can use a dental film or a X-ray sensitive detector at the specimen position. However, sometimes both $K\alpha_1$ and $K\alpha_2$ are employed with a consequent 50% improvement of intensity.

By using DuMond diagrams - which are graphical representations of Bragg's law (Figure 1.2*(ii)*) very accurate calculations can be done. Since the two crystals are parallel, both made of the same material the two DuMond diagrams are the same and so the curves overlap. Thus we get diffraction from all the wavelengths and the role of the collimator is just to limit this range. In

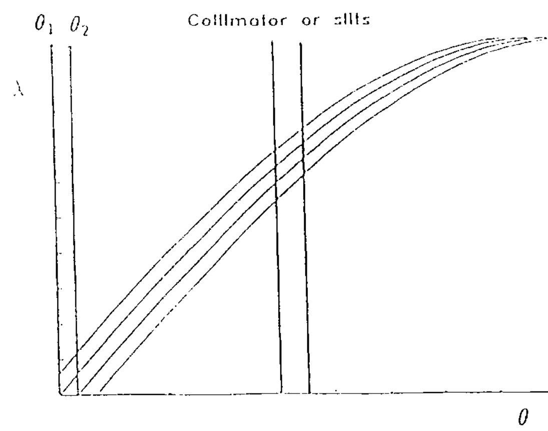

a) The parallel (+n, -n) setting. $\theta_1 = \theta_2$.

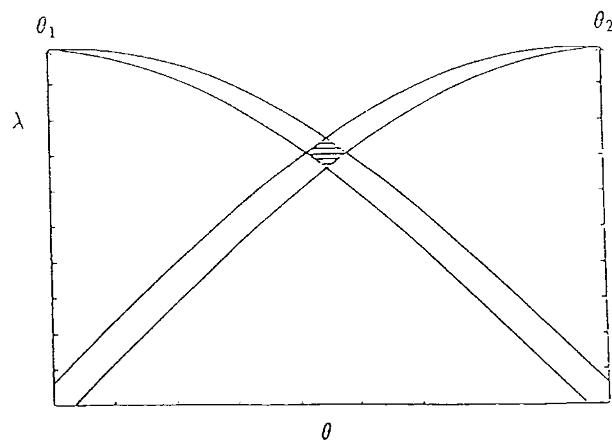

b) The antiparallel (+n, +n) setting. $\theta_1 = \theta_2$

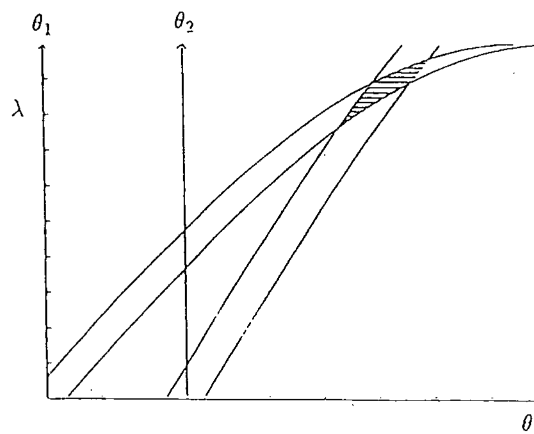

c) The parallel (+n, -m) setting. $\theta_1 \neq \theta_2$.

Figure 1.2(ii):
DuMond diagrams for various diffractometer settings.

(After Hudson)

that case the reference crystal does not act as a monochromator.[2] The angular range results from the convolution of the two perfect crystals reflecting curves.

In a (+n,-n) setting a signal-to-noise of at least 10^{-4} can be managed. Care must be taken to shield the scatter from the reference crystal. This can be achieved by using a small aperture between the reference and the specimen crystal, so that there will be no line of sight between the detector and the collimator. Furthermore, we can take better results in signal-to-noise by using a proportional counter in place of an scintillation detector. It should also be noted that use of a slit in front of the detector to improve signal-to-noise can lead to a change in the FWHM of the rocking curve in an imperfect crystal.

If the lattice parameter of the specimen and the reference crystal differ, known as (+n,-m) mode, then the DuMond diagrams differ as well, and of course complete overlap, as in (+,-) mode, does not occur. The DuMond diagrams intersect at a point which moves rather slowly with angle of misorientation.

Then, the FWHM will be broadened because in this case different wavelengths satisfy the Bragg condition at different angles at the specimen with respect to the reference crystal. The rocking curve broadens by an angle $\delta\theta$ given by:

$$\delta\theta = |\tan\theta_1 - \tan\theta_2| (\delta\lambda/\lambda) \qquad (1.1)$$

where,

θ_1 , θ_2 are the Bragg angle of the specimen and of the reference crystal respectively

$\delta\lambda$ is the bandwidth of the X-ray spectrum passed by the collimator (this is the approximate wavelength difference between $K\alpha_1$ and $K\alpha_2$ lines). Consequently the quantity $\delta\lambda/\lambda$ is the fractional spread in wavelength of the X-rays reaching the specimen. For $CuK\alpha$, if both $K\alpha_1$ and $K\alpha_2$ are present

$\delta\lambda/\lambda = 2.5\times10^{-3}$ whereas when only $K\alpha_1$ is present $\delta\lambda/\lambda = 2.6\times10^{-4}$, which is the intrinsic width of the $K\alpha_1$ line.

Note that the angular broadening of the rocking curve is zero when $\theta_1 = \theta_2$. Furthermore, the $\delta\theta$ can be quite large only for modest differences in lattice parameter when θ_1 and θ_2 become greater than 45°.

In order to optimise an experiment we must choose the Bragg plane spacing of the reference crystal to be close to that of the specimen but the most important is to have a highly perfect reference crystal.[3] Finally the specimen and the reference crystal must be adjusted so that the incident plane contains both incident and diffracted beams. By using GaAs as a reference and InP as a specimen crystal (or vice versa) the broadening of a CuKα beam at 004 reflection is about 17arcsec. This means tripling of the rocking curve width and reducing of the sensitivity to mismatch of an epilayer to about 150 ppm[3].

In order to reduce the effect of dispersion we can use a second reference crystal(Figure 1.3). Settings like $(+\ n,\ +\ n',\ -\ m)$ or $(+\ n,\ +\ n,\ -\ m)$ although they do not totally eliminate the wavelength dispersion, act as true monochromators. The first crystal produces a small angular divergence beam, which contains a range of wavelengths. A very narrow part only, of this wavelength band will satisfy the Bragg condition in the second crystal. So the beam after the second crystal will be limited in angular and wavelength spread. By placing the specimen in a *-m* setting the region of overlap in DuMond diagrams is very small.

This mode has a very high angular sensitivity to strain. The diffracted intensity even for a small angular misorientation of the specimen will be zero. This mode can produce a high angular resolution rocking curve for an arbitrary lattice parameter specimen.

The problem is that we can only use this mode for diffractions with Bragg angle of the order of 30°. Then the diffractometer body has to be at an angle of 120° with respect to the x-ray tube housing. By using a $(-\ n,+\ n,+$

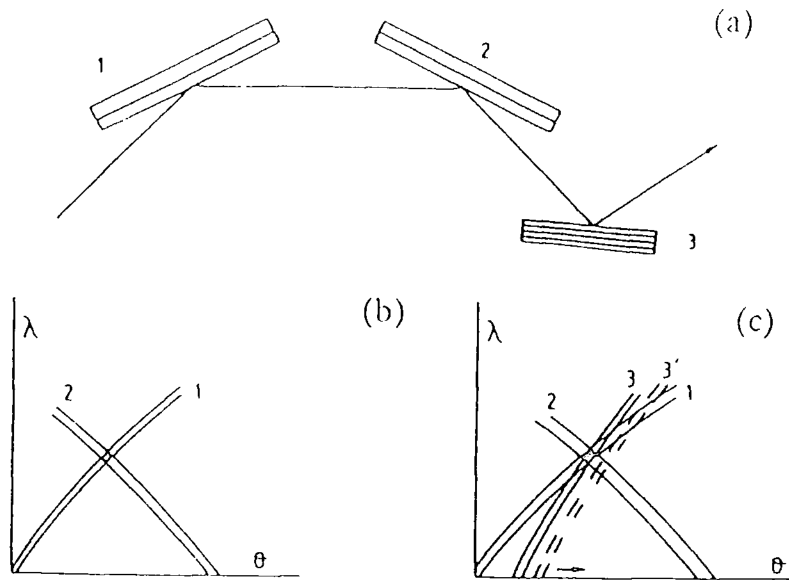

Figure 1.3:
(a) The *(+n,+n,-m)* setting showing true beam monochromatization
(b) The DuMond diagram for the first two reflections.
(c) The DuMond Diagram for all the three reflections. The dotted line 3' corresponds to the specimen crystal anguralrlydisplaced.No overlap, and hence diffracted intensity, results from a very small rotation as in the *(+n,-m)* setting Figure1.2(ii)

(After Tanner)

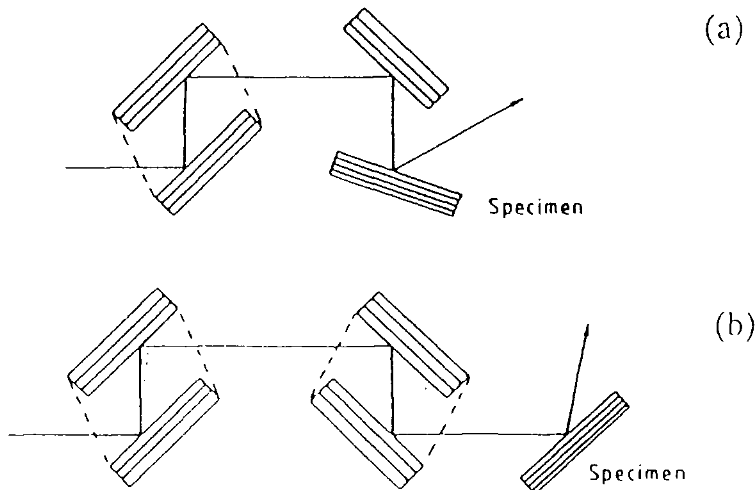

Figure 1.4:
(a) The *(-n,+n,+n,-m)* setting giving a convenient beam geometry and high, dispersion-free, sensitivity to lattice strain.
(b) The four reflection *(-n,+n,+n,-n,-m)* setting giving collinear incident and conditioned beams.

(After Tanner)

n, − m) setting the diffractometer is aligned at the same angle as the single reference reflection of the *(+ n, − m)* setting is. The *(− n, + n, + n, − n, − m)* setting (Figure 1.4) which DuMond (1935) first described has the attraction that the conditioned beam is always colinear with the incident beam. This means that we can change the monochromator reflection or wavelength without realignment of the specimen. The above setting with which many scientists have worked is now commercially available.[4-8]

While that setting removes the broadening due to dispersion (when the reference and the specimen have different lattice parameters), it does not eliminate the broadening due to the specimen curvature. Finally, using that mode we can eliminate the tails of the rocking curves. A lot of attempts have been made in order to create collimators which have certain advantages, like the convenience in the scattering geometry, or like the elimination of tails of the angular and wavelength distribution[1].

b) Triple Axis

By placing an analyser crystal before the detector we have a result that is known as Triple Axis Diffractometry (T.A.D.)[9-11](Figure 1.5). The analyser crystal has the same axis with the specimen, but it is scanned independently of that. A channel-cut Si or Ge analyser crystal is usually suitable for a big range of experiments. While in D.C. Diffraction the scattering is integrated over all angles, (along a line in reciprocal space), in T.A. Diffraction the scattering from the specimen is analysed as a function of angle; and this way the specimen is mapped in a plane in reciprocal space(Figure 1.6).

Thus, diffuse scattering can be separated from coherent scattering and more general scattering from various sources can be easily distinguished. Scattering due to a defect or scattering from a rough surface occurs in different direction in space from that for the perfect crystal. Strain or mismatch can be

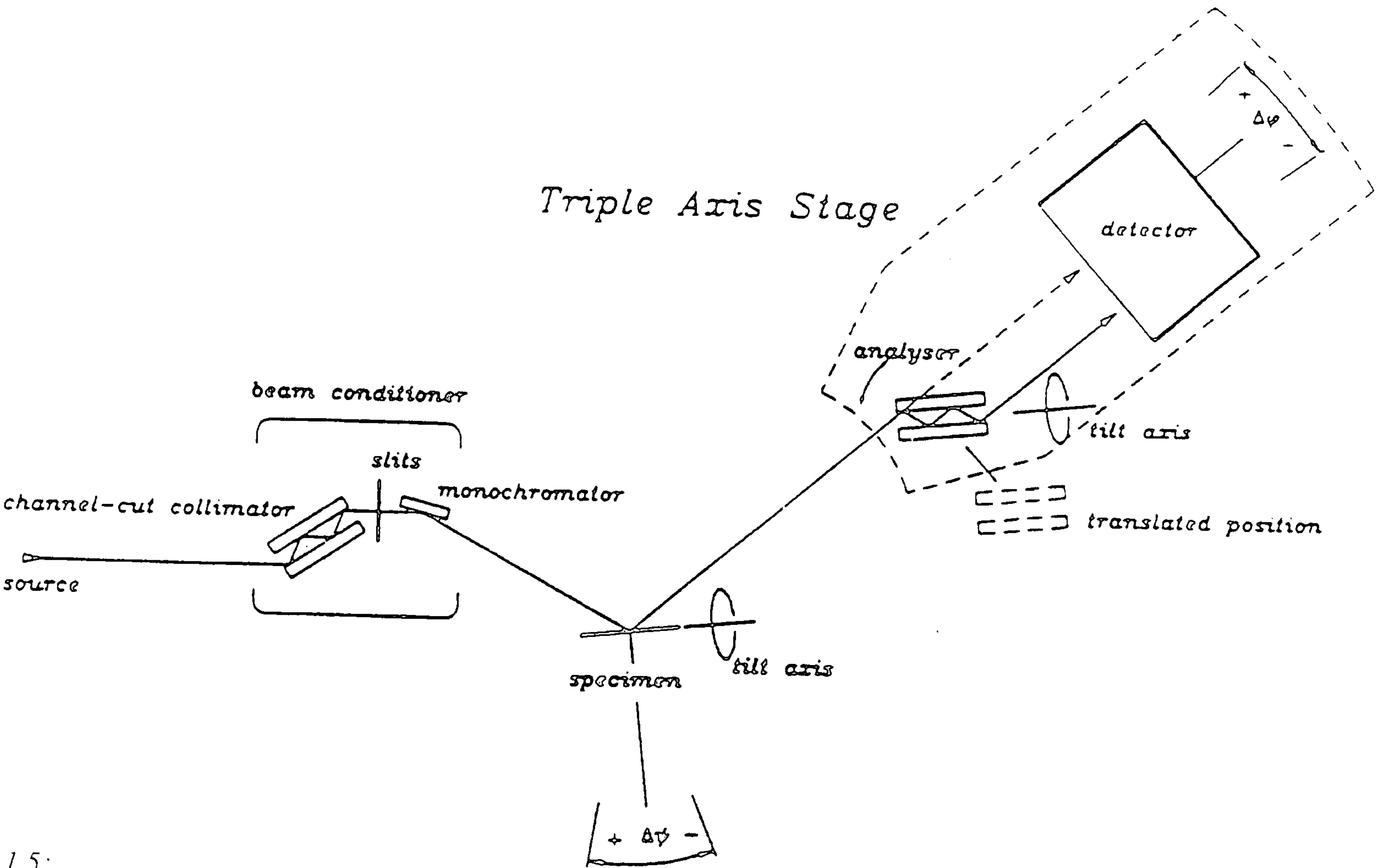

Figure 1.5:
Geometry of triple axis diffractometry.

(After Tanner)

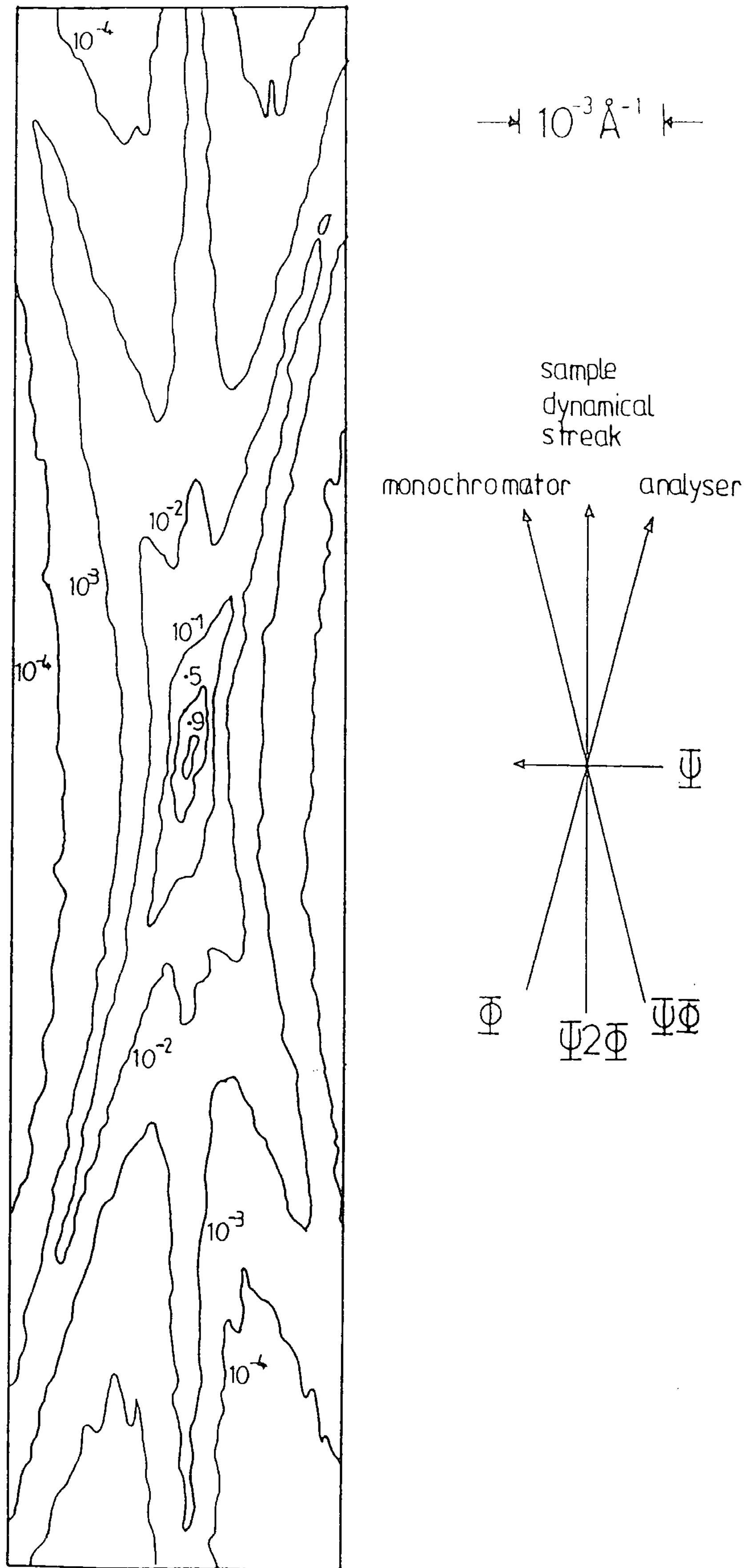

Figure 1.6:
Triple crystal diffractometer contour map in reciprocal space with *Si(111)* monochromator, sample and analyser crystals and a focussing (+1,-1,+1) configuration. CuKα_1, $\theta_m=\theta_s=\theta_\alpha=14.22°$

(After Ryan 1986)

separated from tilt or mosaic spread and therefore the effect of wafer curvature is eliminated. Especially, it is possible to determine independently the Bragg plane tilts and dilations. The above distinction is very difficult in D.C.D.

In T.A.D. if the rocking curves are only recorded by scanning the specimen, they will only produce a measure of the tilt. But if the analyser is stepped around the specimen for each angular position of it, a map of the scattering will be provided; which will actually be a map of the reciprocal space. Integration along a line in reciprocal space discloses the tilt free quasi-double-axis rocking curve.

The signal-to-noise is better than the one of the D.C.D; because the fluorescence of the specimen is eliminated by the additional Bragg reflections from the analyser. Zaumseil et al.[12] managed to take measurements with signal-to-noise in the order of 10^6:1.

The scientific results from this technique were progressively satisfactory. By using glancing incidence geometry, a single quantum well of thickness less than 20nm was readily visible.[13,14] By fitting the rocking curves, structural data about ultra thin layers were more detectable. Fewster,[15] by using TAD and a four reflection monochromator, removed the effect of the curvature and detected interference fringes from a multi-layer (1517 layer AlAs/GaAs, very curved) which would not be observed in DCD. He[16] also managed to remove a lot of the parasitic scatter by using a channel-cut-crystal as analyser.

The only disadvantage of TAD, apart from the complexity of the setting up of the apparatus is the increase in the time for the collection of the data. The above assertion is logical since more data to be collected needs more time.

c) Applications

X-ray high resolution diffraction techniques can provide - accurately or not, directly or not - almost all the information about an epitaxial grown semiconductor sample. We can have, for example, data about:

- the lattice mismatch
- the composition
- the thickness
- the lattice tilt between epilayer and substrate
- the lattice coherency
- the substrate and the layer perfection
- the wafer curvature
- the composition and the thickness variation etc.

Details about the above can be found in many review papers.[17-20]

A typical rocking curve is shown in figure 1.7 where we can see the peak of the substrate and the peak of the layer. The separation of these peaks is related to the different lattice parameter. That is measured by using the lattice mismatch m:

$$m = \frac{a_r - a_o}{a_o} \qquad (1.2)$$

where a_o and a_r are the lattice parameters of the substrate and the layer respectively in bulk form.

When tetragonal distortion is present -unrelaxed layer- the dimension of the unit cell of the layer becomes $a_o \times a_o \times c$, where c is the dimension perpendicular to the interface.

The apparent mismatch m^* is then:

$$m^* = \frac{c - a_o}{a_o} \qquad (1.3)$$

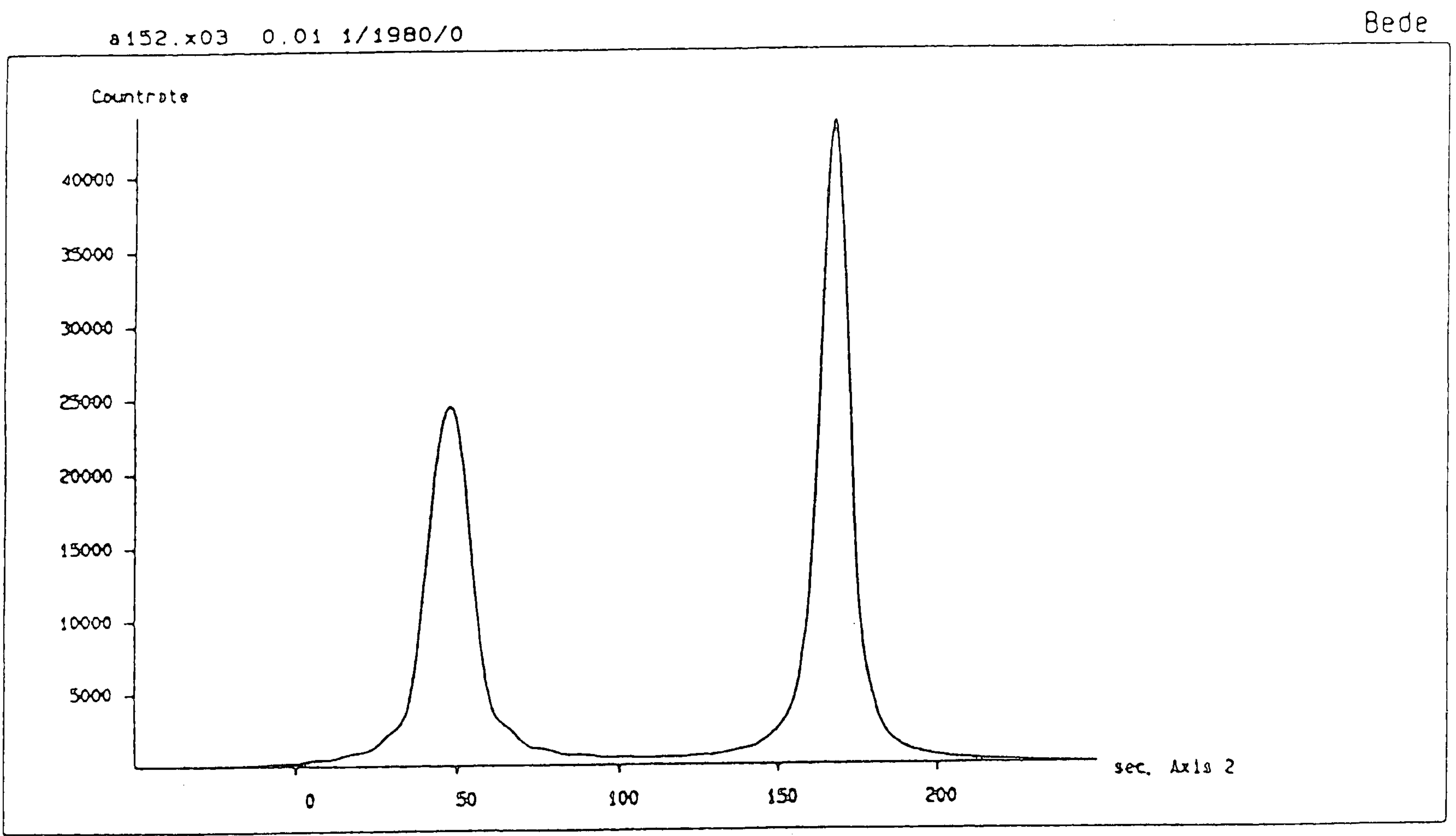

Figure 1.7:
Experimental rocking curve of a 1.45 micron thick layer of $Al_{0.35}Ga_{0.65}As$ on GaAs

(After A.Turnbull, Durham University)

m and m^* are related by:

$$m^* = m\frac{(1+\nu)}{(1-\nu)} \tag{1.4}$$

where ν = Poisson ratio.

In a symmetric reflection the relationship between peak separation and mismatch is found from differentiating Bragg's law.

$$m^* = \frac{\Delta d}{d} = -\cot\theta_B \Delta\theta \tag{1.5}$$

where θ_B is the Bragg angle and

$\Delta\theta$ is the rocking curve peak separation.

Once m is found, the composition of ternaries can be calculated by using Vegard's law (the lattice parameter varies linearly with composition). In order to determine the composition of a quaternary layer, the problem is more complicated and additional information is required[20].

If the layer is thinner than 0.5 mm the determination of m^* by using differentiation of Bragg law is not so accurate. As we will see in Chapter 3 the maximum of the layer peak shifts significantly as the thickness is reduced.

Also the measurement of the peak separation is insensitive to accurate tilt adjustment[21].

In reflections where the Bragg planes are asymmetrical with respect to the specimen surface we can extract information about the lattice parameter parallel to the surface; and hence about the coherence of the layer.[22,23].

Consider that ϕ is the angle between the substrate Bragg planes *(hkl)* and the specimen surface plane. The X-ray beam is incident either at the angle of $(\theta_B+\phi)$ or of $(\theta_B-\phi)$ to the sample surface.

If $d\phi$ is the misorientation between the Bragg planes of substrate and layer and $d\theta_B$ is the difference in Bragg angle of layer and substrate, then the peak separation is $(d\theta_B+d\phi)$ for the high angle of incidence (glancing exit) and $(d\theta_B-d\phi)$ for the low angle of incidence (glancing incidence). Rocking curves

which are recorded using both beam paths can provide $d\theta_B$ and $d\phi$ from the equations:

$$d\theta_B = \frac{d\theta_i + d\theta_e}{2}$$
$$d\phi = \frac{d\theta_i - d\theta_e}{2} \tag{1.6}$$

$d\theta_i$ and $d\theta_e$ are measured separations in the glancing incidence and glancing exit of rocking curves respectively.

The parameter a and c of the layer can be calculated from the equations:

$$\cos(\phi + d\phi) = \left[c^2 \frac{(h^2 + k^2)}{a^2 l^2} + 1 \right]^{1/2} \tag{1.7}$$

$$\sin(\theta_B - d\theta_B) = \frac{\left[h^2 + k^2 + \frac{a^2 l^2}{c^2} \right]^{1/2}}{2a} \tag{1.8}$$

If the (001) Bragg plane of the substrate is misoriented by ϕ with respect to the substrate surface, then the Bragg peak of the substrate appears in two different angles while the sample is rotated about an axis normal to the specimen surface. The maximum difference that we can have is then 2ϕ (Figure 1.8). This method is very accurate and is used for the determination of the disorientation of the layer as well.

The thickness of the layer can be determined by various methods. The relative height of the layer and the substrate peak can give significant information about the thickness of a single layer. However, it is preferable to compare the integrated areas under the peaks as the above areas are not related with tilt misalignment.[24,25] In order to determine the thickness of a thin layer we can make use of the Bragg case interference phenomenon and the Pendellosung oscillations (see Chapter 3).

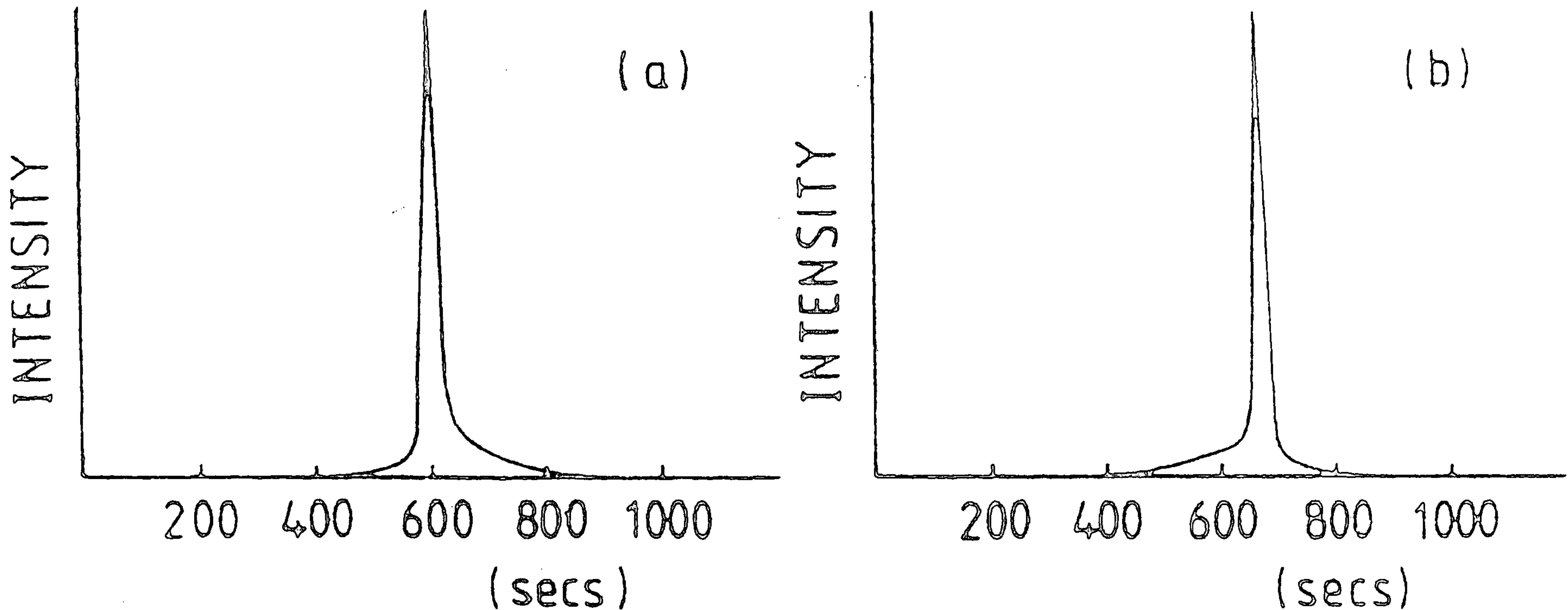

Figure 1.8:
Epitaxial layer misoriented by 100s with respect to a GaAs substrate 2°off (001). 004 reflection.
Rotation angle (a) 0°, (b) 180°

(Courtesy S.J.Miles)

The only method that can provide accurate results is by simulation of the experimental rocking curves with the theoretical curves until a close fit is obtained. The theoretical curves are mathematical calculations based on the Dynamical theory (see Chapter 2). Variable quantities (as sample curvature, crystal quality, layer composition) can be obtained from such studies.

The full width at half height maximum of a substrate or of a layer provides us with a measurement of substrate perfection.[26-30]

As it has been mentioned before, the curvature of the sample leads to the broadening of the peaks; and by using a small diameter collimator (0.5-1 mm) and a slit between the reference crystal and the specimen the above aberration can be reduced. If we use a scanning stage, we can have a map where the position of the Bragg peak will be a function of the position of the beam on the sample (see figures 4.8, 4.13 in Chapter 4). That will provide us with a direct measurement of the wafer curvature. In the same way, using a point by point measurement of rocking curves, a map of either mismatch or composition variation or layer thickness can be drawn.

1.2 Topography

X-ray Diffraction Topography is a technique which provides a two-dimensional map of the distribution of the defects in a crystal. This is managed by recording the spatial distribution of the intensity of the diffracted beam from the specimen. This method is extremely useful, particularly for crystal growth studies and for quality control of crystals.

We can say that Diffraction Topography is the X-ray cousin of Transmission Electron Microscopy but is not so widely used as the T.E.M. since a long exposure time is needed and highly perfect single crystals are required for resolution of individual defects.

Generally the spatial resolution of the technique is limited by

i) the weak scattering

ii) the instrument geometry

iii) the film resolution.

There are several reviews of the x-ray topography in the literature.[1-5]

There are two appearances of an X-ray image. The Orientation contrast and the Extinction contrast. The Orientation contrast is geometrical while the Extinction contrast arises principally from the different scattering power around the defects.

In the following pages an attempt will be made to describe briefly the methods of

a) Berg-Barrett

b) Lang

c) Double Crystal

d) Synchrotron Radiation Topography

a) The Berg-Barrett method

On the basis of Berg's early work Barrett extended that method which is one of the oldest ones. In figure (1.9) the two types[6,7] of the method are represented.

i) The Berg-Barrett Reflection Technique.

ii) The Berg-Barrett Transmission Technique known as Barth-Hosemann.

This general method of Berg-Barrett is widely used for reflection in which high dislocation density materials are examined. One great advantage of this method is that no expensive or high-precision components are required. Because of the wide source, compared to the specimen, the accuracy of the specimen position is not critical. The Bragg reflection is visible within an angular range of 1°.

The negative points of Berg-Barrett Topography are that it is relatively insensitive to orientation contrast on one hand, and particularly the bad resolution, due to the polychromatic x-ray on the other hand.

b) Lang's technique

This is a very sensitive technique to both extinction and orientation contrasts and is perhaps the best known among the transmission x-ray topographies. There are two types of Lang topography:

i) section topography[8]

ii) projection topography[9]

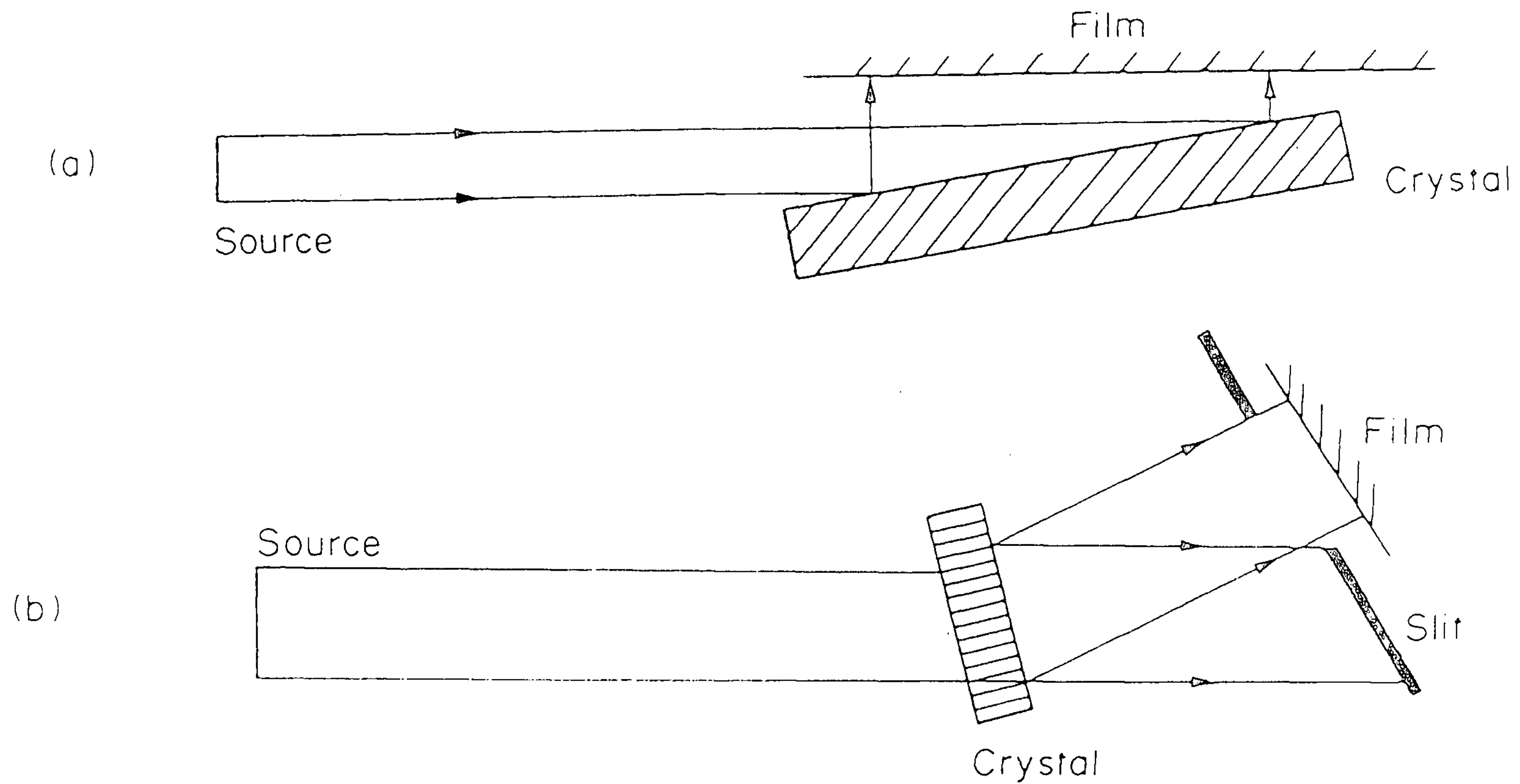

Figure 1.9:
a) Reflection Berg-Barrett technique of topography.
b) Transmission Berg-Barrett (Barth-Hosemann) technique

(After Tanner)

i) Section topography

In this method, which is the most basic, the specimen crystal and the recording film are stationary so only a part of the crystal is investigated each time; therefore section topography is not suitable for a general examination.

Apart from the stationary set up it is important to notice that an incident beam is collimated into a narrow ribbon (by a slit about 10 μm in width). Obviously the image is only a narrow "section" of the specimen (Figure 1.10).

Despite the mentioned disadvantage section topography is remarkably useful for crystals in which the defects are uniformly distributed or have certain symmetries. If the Bragg angle is not too small, from the image of the section topography, valuable information can be taken about the flow of energy within the crystal and direct depth information can also be gained about the defects present. The latter one is explained by Gerward and Lindegaard with a step scanned section topography.[10]

Finally more information can be taken by simulating the image to a high level of detail. [11]

ii) Projection Topography

With Projection Topography a two-dimension map of the defect structure through the whole crystal is recorded. In this technique which is the best known among all topographies, the specimen crystal and the film are scanned together across the ribbon beam. (Figure 1.11-The slit is typically 200 μm wide)

Because the image width is typically a few microns, an individual dislocation can be resolved if the dislocation density is less than 10^4 cm^2; above this, rocking curve broadening becomes apparent.

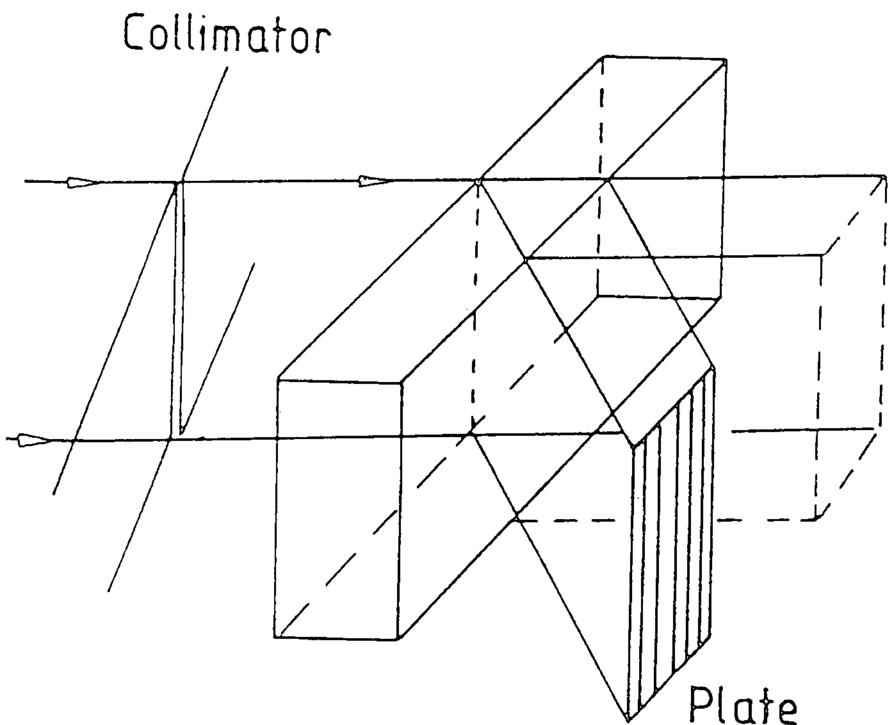

Figure 1.10:
(left) Section topography arrangment.
(right)Section topograph showing denuded zone in heat-treated silicon wafer.
(Courtesy P.J.Halfpenny, GEC Hirst Research Center)

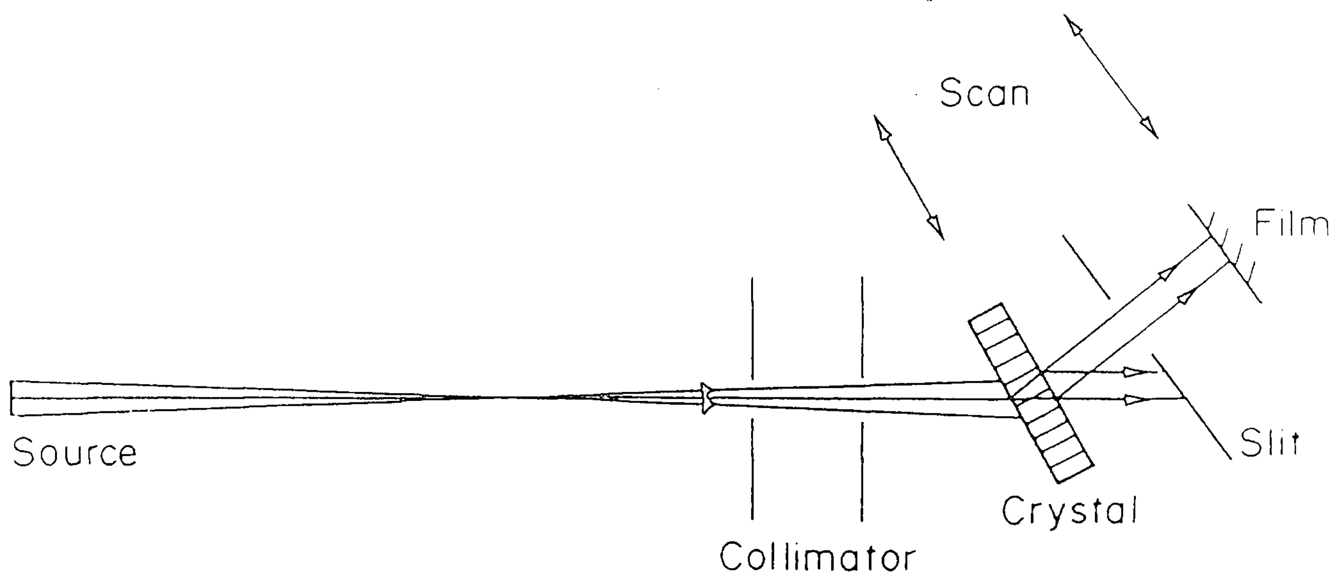

Figure 1.11:
Lang's transmission technique.
Section topographs correspond to the stationary situation.
Projection topographs are taken by scanning crystal and film across the beam.
(After Tanner)

Integration in time of projection topography results in a topography equivalent to the one taken by the Berg-Barrett method, where the integration is in space.

Unfortunately by using projection topography we lack information (such as energy flow within the crystal) that section topography can provide. Of course scanning of the section topography results in the projection topography and one often stops at a point on a projection topograph and examines the small region chosen with the aid of series of section topographs.

In order to do it one needs to tune the collimating slits width. For the section, described above, the slit width is about 10 μm and for projection topographs is approximately 200 μm.

Another way to determine the position, especially the depth of the defects, is to take stereo pairs of projection topographs. This works well only for low absorption and it is not sensitive. However, for a qualitative quick scan in a large area the method is satisfactory. A similar method was developed in 1965: to use a single reflection but to take two topographs rotated $\pm 8°$ about the diffraction vector. As it is obvious, those two methods are available only for thick crystals.[12]

The most common complaint about X-ray topography is the long exposure time. The photographic method while giving excellent resolution and contrast, is very slow and not available for dynamic experiments in which the defect configuration varies on a time scale of seconds and minutes.

For semiconductors, where high resolution is not needed, use of fast but low resolution film permits a projection topograph to be taken in about a half an hour. In the same way medium resolution topography can be used to screen semi-insulating GaAs substrates for detect uniformity.

Apparently the best improvement in speed without losing resolution is the curved crystal technique[13]. Complete topographs can be recorded in a few

minutes time. Unfortunately, it can only be applied to thin plates of brittle material and has not been used extensively.

Very small exposure times can be achieved by using synchrotron radiation topography, as will be described later.

There is a review article of Green[14] concerning viewing systems which had been developed until 1971 and a more recent one written by Cringean and Tanner[15] published in 1986. But day by day new viewing techniques appear. Now the common opinion is that the X-ray topography is not particularly slow, but observing high resolution X-ray topographs in real time, such as electron microscopists do regularly, has not been accomplished yet.

c) Double Crystal Topography

Theoretically Single Crystal Topography is sensitive to detect strains of an order of 1 part in 10^5 but in practice it is very insensitive to show variations of lattice parameter until they become of the order of one part in 10^3. Therefore Double Crystal Topography is used which is able to detect long range strain. In DCT sensitivities of parts in 10^{-8} - 10^{-10} are possible in the best silicon.[16]

It is worth noting that the contrast in single crystal topography arises principally from the different scattering power around the defect (i.e. extinction contrast), while at DCT the contrast is geometrical. (i.e. orientation contrast) [17]

The Double Crystal method of topography, which was developed by Bond and Andrus[18] and Bonse and Kappler[19], is not very widely used but has the advantage that it can be derive deasily from the DCD instrument by the replacement of the pinhole collimator by a large aperture slit. According to the name of the method it is obvious that two Bragg reflections are needed.

In Double Crystal Topography similar mode of reflections, similar rules and conditions are used as used in Double Crystal Diffraction. One type of double crystal topography is where a (+,-) parallel setting is applied, and as it is mentioned above, it is important to have the Bragg planes of the two crystals parallel, and the two crystals of equal lattice spacing.

Again, the method is non dispersive in wavelength. By the examination of the DuMond diagrams we can predict approximately the local image of a defect. For a local misorientation in the specimen, the local part of the curve is misplaced and no region of overlap occurs for any wavelength, so a local loss of the intensity appears. In the same way for a dilation the DuMond diagram, changes locally and the angular range over which simultaneous diffraction occurs, is very narrow and may be as low as 0.1 second of arc.(Figure1.12)

A very important thing in studying Double Crystal Topography is that the image must be considered as arising from defects in both crystals. Fortunately, in the laboratory the reference crystal is quite far from the photographic plate and thus, defects from this crystal appear to be blurred, so they are usually not troublesome. This is not the case with synchrotron radiation. Of course, we can always distinguish the defects from the two crystals by rotating by 90° of one of the crystals. That simple trick was first done by Hart[20] in DCT of LOPEX silicon.

For high resolution topography as happens with the Diffractometry, it is crucial to ensure that the tilt between the Bragg planes is small and also the same material is used for both of the crystals. However, in such topographs the images of dislocations appear very broad as high contrast is obtained from the small strains present far from the dislocation core. Therefore, the DCT is not very useful for studying crystals with high dislocation densities.

Although the (+,-) parallel setting is not dispersive to wavelength, unfortunately, it is angular dispersive and for that reason images from the same defect but from different wavelengths are formed at different points of the film.

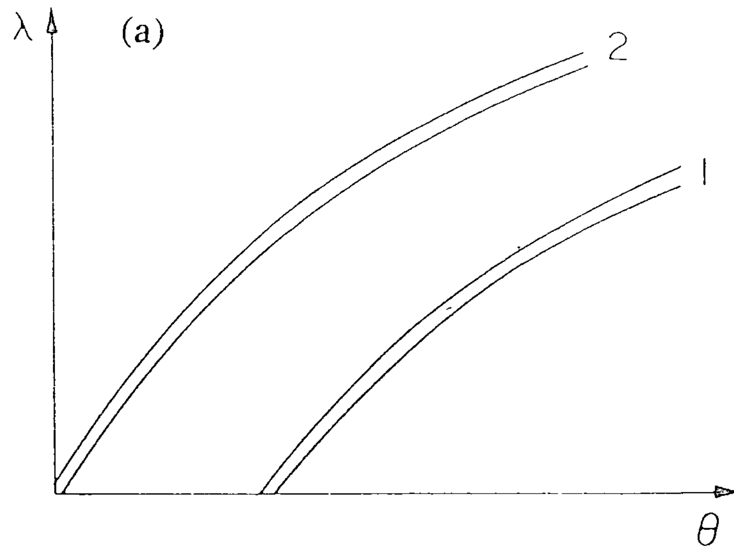

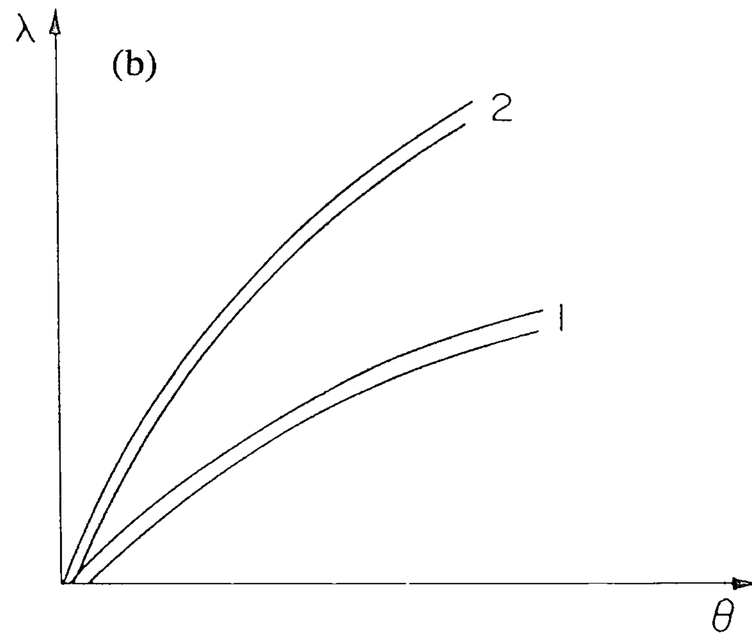

Figure 1.12:
a)DuMond diagram corresponding to local rotation of the lattice in the second crystal.
b)DuMond diagram corresponding to local dilation in the second crystal.
(After Tanner)

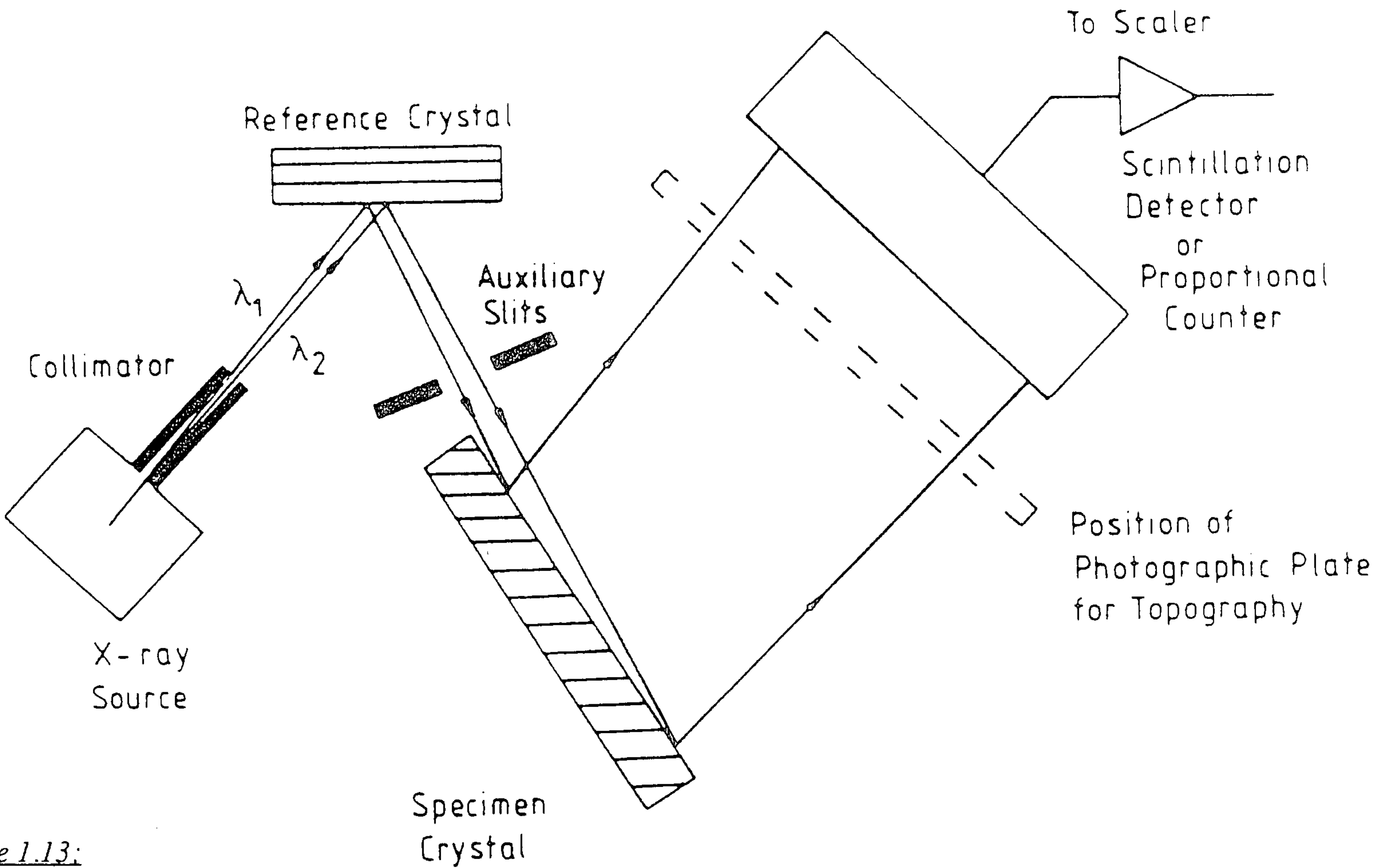

Figure 1.13:
Schematic diagram of the arrangment for double crystal diffractometry and topography. An asymmetrically cut reference crystal may further expand (or compress) the beam.

(After Tanner)

That problem is usually solved by using different materials at the two crystals (thereby introducing some dispersion) As happens in the (+,+) setting the wavelength is limited in the (+n, -m) mode, and therefore the angular sensitivity is reduced. As it is obvious, the (+n, -m) setting is a very flexible technique.

The (+,+) setting (equal Bragg plane spacing and non-parallel Bragg plane) was first exploited by Kohra and his co-workers[21] and developed by Nakayama [22]. In that mode we can have an image of quite large misorientation without loss of intensity. The angular sensitivity is the same as in the Lang technique but the defect contrast is complex and therefore the mode is not so widely used.

Use of an asymmetric reflection results in expansion of the beam in order to cover the whole of the specimen area. Such beam expansion is commercially available. The use of asymmetric reflections in collimators is studied by Kikuta and Kohra[23] and Kikuta[24]. By taking two measurements - the second is done by rotating the specimen about its surface normal (if nearly a symmetry axis) - we can distinguish tilts and dilation.[25,26]
By using a triple axis formation only the tilts can be detected immediately.[27]

Very accurate measurements of relative lattice parameter can be managed by introducing multiple Bragg reflection in a DC arrangement. Hart[28] in 1969 succeeded in getting a precision of one part in 10^9 by using two crystals cut from the same block of silicon. In the first version, two X-ray sources were used, but recent arrangements have been designed with the use of only one source.

A very interesting phenomenon appeared when the crystal contains regions of misorientation greater then the rocking curve width. Then a stripe of contrast is obtained from that part of the crystal. If we step the specimen with respect to the reference crystal and expose on the same part of the film, a "zebra pattern" of contours will be built up[27,29].

Double Crystal Topography in the reflection geometry gives better defect contrast than the reflection type of projection topography. Of course, projection topography is normally used in transmission geometry which is inappropriate for studying defects in epitaxial layers. For incident angles of less than 10° the technique is very sensitive to near surface defects.

d) Synchrotron Radiation Topography

A large melt-grown compound semiconductor crystal contains effective misorientation much larger than the rocking curve width. Furthermore, if defects over the whole crystal must be detected by using the above methods it is obvious that multiple exposures are necessary. Finally it is well-known that the exposure time is unacceptably long for a slow, high resolution recording. Using synchrotron radiation topography, all these problems can be solved.

Based on a method developed by Guinier and Tennevin[30] and Tuomi, Naukkarinen and Rabe[31] performed the first synchrotron topography experiments in 1974.

If an electron is constrained to a circular orbit, it emits electromagnetic radiation in a cone form tangential to the electron orbit. That radiation is the synchrotron radiation. The beam appears with a small angular divergence (10^{-4} radians for 5 GeV) It is polarised in the plane of the orbit and the spectrum of the radiation extends from the ultraviolet to the X-ray region.

By placing the crystal in a beam of synchrotron radiation we can record the image of the diffracted beam on ILFORD L4 plate in a time of some seconds. It is highly remarkable that every crystal lattice plane will select a particular wavelength for diffraction *(Laue pattern)*. The image that we obtain is a number of "spots". Each "spot" is a different image of the crystal.

The size of the beam is adjustable and can be relatively wide. Therefore, scanning of the crystal is not required. The only adjustment we need at the set up is to adjust the crystal orientation (approximately 1°) in order to select the approximate wavelength required in any particular diffraction.

Problems appear when the specimen is far from the recorded medium. Then a mixture of extinction and orientation contrast exists and it is difficult to disentangle them. Furthermore, the extinction contrast is sometimes complicated if more than one diffraction order contributes to the image.

Double Crystal Synchrotron Radiation Topography was performed for experiments in this thesis. A Si crystal was used as a reference crystal. The wavelength was λ=1.541Å, the beam size was a rectangle of 40 mm×15mm and the range of the beam current was about 130mA.. For the above condition and using ILFORD L4 photographic plates the exposure time for high resolution topographs was 10 min.

In conclusion

the basic *advantages* of the method are:

- huge beam size
- small exposure time
- tuneability of wavelength and polarisation independently
- extremely easy to perform

The disadvantages of the method are:

- need of synchrotron
- the contrast of the defects is sometimes more complicated than that of the other techniques

Despite the fantastic results from the Synchrotron Topography today the challenge is to bring the topography methods back to the laboratory.

Chapter 2

Dynamical Theory

The most accurate technique for the characterisation of crystals with x-ray is the theoretical prediction of the results and the comparison with the measurements. Simulation can be performed at a basic level using kinematical theory, but there exists a more powerful method, namely the dynamical theory.

In the kinematical theory we have to assume that the amplitudes of the scattered waves are small compared to the incident wave amplitude. A complete view of kinematical theory can be found in a great number of books.[1] For small crystals (where the scattered amplitude is negligible compared with the incident amplitude) or for heavily deformed crystals having a mosaic structure, the kinematical theory works satisfactorily.For a perfect single crystal, though, we need a theory to take into account multiple scattering and depletion of beam energy, such as dynamical theory does with time consuming calculations.

The two theories have a simultaneous attendance in the progress of simulation. Moreover the main concepts, for example the structure factor, are common to both theories In 1987 Bartels[3] used dynamical theory calculations for the substrate intensity and that of kinematical for the layer intensity. In 1986 Tapper and Ploog[4] employed Petrashen's semi-kinematical theory. The full dynamical theory in the Takagi-Taupin formalism is the one that is widely used

today by most of the scientists. For a full description of the dynamical theory one should refer to the books of James (1948)[1] and Pinsker (1978).[2]

2.1 The "Classical" Dynamical Theory

We assume that the electric displacement vector in vacuum is a plane wave.

$$\vec{D} = \vec{D}_o(\vec{r})\exp\{i[\omega_o t - 2\pi\Phi_o(\vec{r})]\} \tag{2.1}$$

where $\Phi_o(\vec{r}) = \vec{k}_o \cdot \vec{r}$ and $|\vec{k}_o| = \frac{1}{\lambda}$

In a general case $\vec{D}$ satisfies the wave equation in a vacuum:

$$\vec{\nabla}^2 \vec{D} + \frac{\omega_o^2}{c^2}\vec{D} = 0 \tag{2.2}$$

Considering spherical waves for which the radii of curvature are much larger than the wavelength λ, we have :

$$|\vec{\nabla}\Phi_o| \approx \frac{1}{\lambda}\left[1 + 0\left(\frac{\lambda^2}{R^2}\right)\right] \tag{2.3}$$

$0\left(\frac{\lambda^2}{R^2}\right)$ are negligibly small terms of higher orders of λ/R

For a nearly plane incident wave we will get

$$\vec{\nabla}\Phi_o = \vec{k}_o + \Delta\vec{k}_o \tag{2.4}$$

Therefore from (2.3) we have

$|\vec{k}_o| = \frac{1}{\lambda}$, $|\Delta\vec{k}_o| = R^{-1}$

When we take a Bragg-reflection inside the crystal, first of all, we have to solve Maxwell's equations in a periodic medium.

$$\vec{\nabla}\cdot\vec{E} = 4\pi\rho \tag{2.5}$$

$$\vec{\nabla}\cdot\vec{H} = 0 \tag{2.6}$$

$$\vec{\nabla}\times\vec{E} = -\frac{1}{c}\frac{\partial\vec{H}}{\partial t} \tag{2.7}$$

$$\vec{\nabla}\times\vec{H} = \frac{1}{c}\left(\frac{\partial\vec{E}}{\partial t} + 4\pi\vec{J}\right) \tag{2.8}$$

where

$\vec{B} = \mu\vec{H}$ and $\vec{D} = \varepsilon\vec{E}$

By taking the curl of both sides of the (2.7), we obtain:

$$\vec{\nabla}\times\left(\vec{\nabla}\times\vec{E}\right) = -\frac{1}{c}\vec{\nabla}\times\frac{\partial\vec{H}}{\partial t} = -\frac{1}{c}\frac{\partial}{\partial t}\left(\vec{\nabla}\times\vec{H}\right) \tag{2.9}$$

We know that $\varepsilon = 1 + \chi$ and $\chi << 1$

$$\left(\frac{1}{\varepsilon} = (1+\chi)^{-1} = 1 + (-1)\cdot\chi + \frac{(-1)(-2)\chi^2}{2!} + \cdots \cong 1-\chi\right)$$

then

$$\vec{E} \cong (1-\chi)\vec{D} \tag{2.10}$$

From (2.8) , (2.9) , (2.10) ,

$$\vec{\nabla}\times\vec{\nabla}(1-\chi)\vec{D} = -\frac{1}{c^2}\frac{\partial^2 \vec{D}}{\partial t^2} = -\frac{1}{c^2}\left(-\omega^2\vec{D}\right) = \frac{\omega^2}{c^2}\vec{D}$$

$$= \frac{4\pi^2\nu^2}{\lambda^2\nu^2}\vec{D} = \frac{4\pi^2}{\lambda^2}\vec{D}$$

so

$$\vec{\nabla}\times\vec{\nabla}\times(1-\chi)\vec{D} = \frac{4\pi^2}{\lambda^2}\vec{D} \tag{2.11}$$

Furthermore, susceptibility can be expanded as a Fourier series, reflecting the periodic structure of the crystal lattice, so that

$$\chi = \sum_m \chi_m \exp\left(2\pi i\vec{h}\cdot\vec{r}\right) \tag{2.12}$$

where $$\chi_m = -\frac{e^2\lambda^2}{\pi mc^2 V}F_m \tag{2.13}$$

where

e = electronic charge

λ = wavelength

m = electron mass

c = velocity of light

V = unit cell volume

F_h = structure factor

For the general case of an absorbing crystal

$$\chi_o = \chi_{or} + \chi_{oi} \quad , \quad \chi_h = \chi_{hr} + i\,\chi_{hi} \tag{2.14}$$

The wavefield in the crystal can be expressed as a Bloch wave.

$$\vec{D} = \sum \vec{D}_m \exp\left(-2i\pi\vec{k}_m \cdot \vec{r}\right) \tag{2.15}$$

where $\vec{k}_m$ are linked by the Laue condition :

$$\vec{k}_m = \vec{k}_o + \vec{h}_m \tag{2.16}$$

and

$$\vec{k}_o = \vec{\nabla}\Phi_o \tag{2.17}$$

Substituting (2.12) and (2.15) into (2.11) will give[5]

$$\sum_g \left\{\chi_{m-g}\left(\vec{k}_m \cdot \vec{D}_g\right)\vec{k}_m - \chi_{m-g}\left(\vec{k}_m \cdot \vec{k}_m\right)\vec{D}_g\right\} = \left\{k^2 - \vec{k}_m \cdot \vec{k}_m\right\}\vec{D}_m \tag{2.18}$$

If we draw a sphere of radius k, in reciprocal space, then the condition of Bragg reflections is that the sphere will cut a reciprocal lattice point and the origin. For the x-ray case the curvature of this Ewald sphere is large, therefore the probability of more than two points being cut by the surface of the sphere is very small.

As we did before, we need to consider two beams: one transmitted and one diffracted.

The equation (2.15) then becomes

$$\vec{D} = \vec{D}_o \exp\left(-2\pi i\vec{k}_o \cdot \vec{r}\right) + \vec{D}_h \exp\left(-2\pi i\vec{k}_h \cdot \vec{r}\right) \tag{2.19}$$

and the system will be reduced to:

(m=h)

(g=0) $\chi_h(\vec{k}_h \cdot \vec{D}_o)\vec{k}_h - \chi_h(\vec{k}_h \cdot \vec{k}_h)\vec{D}_o$

(g=h) $+\chi_o(\vec{k}_h \cdot \vec{D}_h)\vec{k}_h - \chi_o(\vec{k}_h \cdot \vec{k}_h)\vec{D}_h$

$$= \{k^2 - \vec{k}_h \cdot \vec{k}_h\}\vec{D}_h \qquad (2.20)$$

(m=0)

(g=0) $\chi_{\bar{h}}(\vec{k}_o \cdot \vec{D}_h)\vec{k}_o - \chi_{\bar{h}}(\vec{k}_o \cdot \vec{k}_o)\vec{D}_h$

(g=h) $+\chi_o(\vec{k}_o \cdot \vec{D}_o)\vec{k}_o - \chi_o(\vec{k}_o \cdot \vec{k}_o)\vec{D}_o$

$$= \{k^2 - \vec{k}_o \cdot \vec{k}_o\}\vec{D}_o \qquad (2.21)$$

where $k^2 = |k|$

$k = |\vec{k}|$ and $\vec{k}$ = wavevector in vacuum

χ_h , $\chi_{\bar{h}}$ are the Fourier components of the susceptibility corresponding to the reciprocal lattice vector and its inverse.

It should be noted that $\vec{k}_o \cdot \vec{D}_o = \vec{k}_h \cdot \vec{D}_h = 0$

(the electric displacements are always transverse)

We can write now the system as :

$$k^2 C\chi_{\bar{h}} D_h \quad + \{k^2(1+\chi_o) - \vec{k}_o \cdot \vec{k}_o\}\vec{D}_o \quad = 0 \qquad (2.22)$$

$$\{k^2(1+\chi_o) - \vec{k}_h \cdot \vec{k}_h\}\vec{D}_h \quad + k^2 C\chi_h D_o \quad = 0 \qquad (2.23)$$

where $C = \hat{D}_o \cdot \hat{D}_h = \begin{cases} 1 & \text{for } \sigma \text{ polarization} \\ \cos 2\theta_B & \text{for } \pi \text{ polarization} \end{cases}$

θ_B = Bragg angle

and for a non trivial solution

$$\begin{vmatrix} k^2 C\chi_{\bar{h}} & k^2(1+\chi_o) - \vec{k}_o \cdot \vec{k}_o \\ k^2(1+\chi_o) - \vec{k}_h \cdot \vec{k}_h & k^2 C\chi_h \end{vmatrix} = 0 \tag{2.24}$$

We can write :

$$\alpha_o \alpha_h = \frac{1}{4} k^2 C^2 \chi_h \chi_{\bar{h}} \tag{2.25}$$

where

$$\alpha_o = \frac{1}{2k}\left\{\vec{k}_o \cdot \vec{k}_o - k^2(1+\chi_o)\right\} \tag{2.26}$$

$$\alpha_h = \frac{1}{2k}\left\{\vec{k}_h \cdot \vec{k}_h - k^2(1+\chi_o)\right\} \tag{2.27}$$

The equation (2.25) is the equation of the dispersion surface and is the fundamental equation linking $\vec{k}_o$ and $\vec{k}_h$ in the crystal. Each wavevector within the crystal must lie with its tail on the dispersion surface. A representation of this surface will be shown in the next few lines.

We draw two spheres of radius k around the point O and H respectively as in Figure 2.1. The point of intersection, L is called *Laue point.* Now we draw two new spheres of radius nk , where n is the refractive index. (note for x-rays n <1). These spheres represent points corresponding to waves far from the exact Bragg condition.

As we can see in Figure 2.2 :

AB and A'B' are arcs of the spheres of radius k

CD and C'D' are arcs of the spheres of radius nk

The tie-point P is the position of a point corresponding to an allowed pair of wave vectors.

$\vec{k}_o = \vec{PO}$

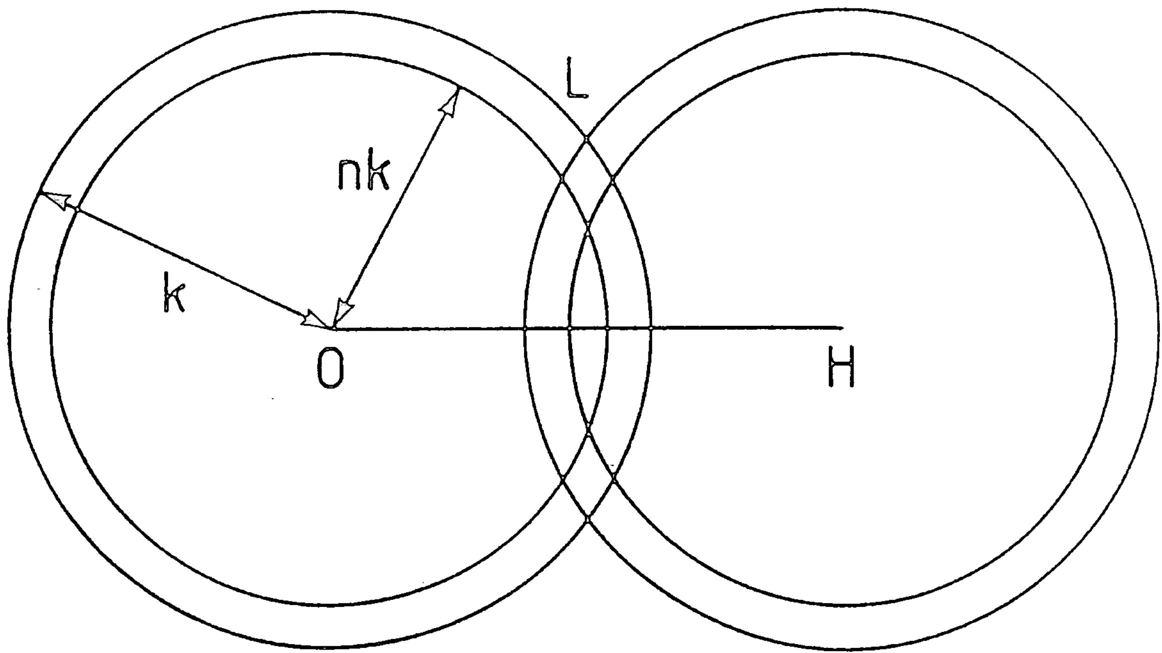

Figure 2.1 : Spheres in reciprocal space about lattice points O and H

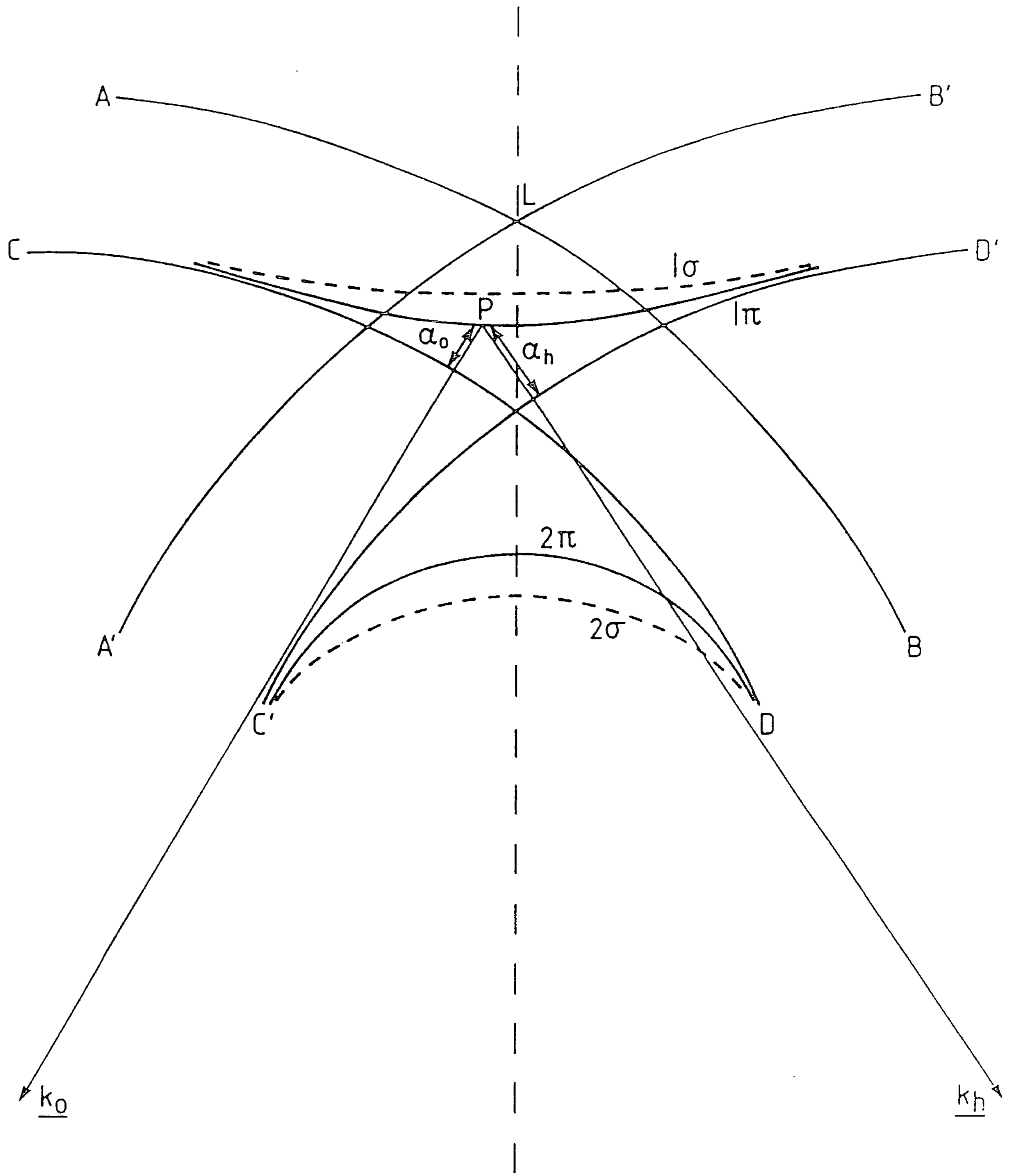

Figure 2.2 : The dispersion surface construction, (After Tanner)

$\vec{k}_h = \vec{PH}$

α_o and α_h are perpendicular distances from the point P to spheres CDand C'D'.

The equation (2.25) (dispersion surface) is a hyperboloid of revolution about OH and its projection onto the plane of the paper is a hyperbola which is split into two branches, (1) and (2). Each branch will be split into parts,

one corresponding to σ - polarisation,

and one to π - polarisation.

The dispersion surface is a very meaningful concept. It determines that the allowed wavevectors can be shown, also that the direction of energy flow is perpendicular to the dispersion surface, and furthermore, it determines the amplitude ratio of the component plane waves in the Bloch wave.

2.2 The Takagi-Taupin Equations

The above approach works well for a perfect crystal and plane wave, but generally $\vec{k}_o$ and $\vec{h}_m$ are functions of the coordinates. For each point in the crystal the vector $\vec{h}_m$ can be determined.

If the planes in a crystal, denoted by n_m are regarded as a continuous function of the co-ordinates which take integral values on each plane *m* we will find:

$$\vec{h}_m = \vec{\nabla} n_m \tag{2.28}$$

$$\vec{\mathrm{D}} = \sum_m \vec{\mathrm{D}}_m \exp(-2i\pi\Phi_m) \tag{2.29}$$

$$\Phi_m(\vec{r}) = \Phi_o(\vec{r}) + n_m(\vec{r}) \tag{2.30}$$

Where

$$\begin{aligned} \vec{k}_o \cdot \vec{r} &= \Phi_o & \vec{k}_o &= \vec{\nabla}\Phi_o \\ \vec{k}_m \cdot \vec{r} &= \Phi_m & \vec{k}_m &= \vec{\nabla}\Phi_m \\ \vec{h}_m \cdot \vec{r} &= n_m & \vec{h}_m &= \vec{\nabla} n_m \end{aligned} \tag{2.31}$$

Calculating the left hand side of the equation (2.11) and using the equation (2.2), (2.12) and (2.28) we get

$$\frac{4\pi^2}{\lambda^2} \sum_m \vec{\mathrm{D}}_m \exp(-2\pi i \Phi_m) = \vec{\mathrm{A}} \tag{2.32}$$

where $\vec{\mathrm{A}}$ is a function in terms of varying magnitude.

Neglecting small terms (see Pinsker, 1978) we obtain

$$\alpha_m \vec{D}_m - \sum_h \chi_{m-h} \vec{D}_h \cos X_{mh} + \frac{i\lambda^2}{\pi}\left(\vec{k}_m \vec{\nabla}\right)\vec{D}_m = 0 \qquad (2.33)$$

Where

$\cos X_{mh}$ is the polarization factor

α_m is the variable representing the angular departure from the Bragg condition. It is taken as :

$$\alpha_m = k_o^{-2}\left[h_m^{\,2} + 2\left(\vec{k}_o \cdot \vec{h}_m\right)\right] = \lambda^2\left(\frac{1}{d_m^2} - \frac{2\sin\theta_m}{\lambda d_m}\right) \qquad (2.34)$$

and approximately :

$$\alpha_m = 2\Delta\theta_m \sin 2\theta_m \qquad (2.35)$$

Both d_m and $\sin \theta_m$ are co-ordinate dependent.

For propagation of x-rays in a perfect crystal we have to solve this system in first order partial derivatives. The variable α_m is calculated to allow for local deformations at any point in the crystal. For the two-beam case we need only consider $m=0$, $m=h$

Allow $\vec{s}_o$ and $\vec{s}_h$ to be unit vectors in the direction of the incident and diffracted beam respectively, then

$$\vec{s}_o = \lambda\vec{k}_o \qquad \vec{s}_h = \lambda\vec{k}_h \qquad (2.36)$$

and for any point on the reflection plane

$$\vec{r} = s_o\vec{s}_o + s_h\vec{s}_h \qquad (2.37)$$

Then the system (2.33) is reduced to

$$\frac{i\lambda}{\pi}\frac{\partial \mathrm{D}_o}{\partial s_o} = \chi_o \mathrm{D}_o + C\chi_{\bar{h}} \mathrm{D}_h$$

$$-\frac{i\lambda}{\pi}\frac{\partial \mathrm{D}_h}{\partial s_h} = (\chi_o - \alpha_h)\mathrm{D}_h + C\chi_h \mathrm{D}_o \tag{2.38}$$

where

$$C = \cos \mathrm{X}_{oh}$$

We can include the polarisation factor C in the values χ_h and $\chi_{\bar{h}}$ by adding the symbols σ and π, so that

$$\chi_h^\sigma = \chi_h^\pi \left(|\cos 2\theta|\right)^{-1} \qquad \chi_{\bar{h}}^\sigma = \chi_{\bar{h}}^\pi \left(|\cos 2\theta|\right)^{-1} \tag{2.39}$$

2.3 The Solution of the Takagi-Taupin Equations

Equation (2.38) are known as the Takagi-Taupin equations and we can use them to calculate the reflectivity of a given crystal in the Bragg case. We will assume that the incident wave is plane, and that the variations in diffracted intensity will only be a function of depth. The amplitude ratio of the incident and diffracted beams is required.

$$\gamma_o = \sin \ i$$
$$\gamma_h = -\sin \ e \tag{2.40}$$

i,e, the angles of incidence and reflection regarding the surface normal

For an asymmetric reflection γ_o and γ_h are not equal.

$$b = \frac{\gamma_o}{\gamma_h} \tag{2.41}$$

For a symmetric Bragg case reflection b = -1

The depth below the surface z is given by

$$z = s_o\gamma_o + s_h\gamma_h \tag{2.42}$$

Then (2.38) will become

$$\frac{i\lambda}{\pi}\gamma_o \frac{\partial D_o}{\partial z} = \chi_o D_o + C\chi_{\bar{h}} D_h$$

$$\frac{i\lambda}{\pi}\gamma_h \frac{\partial D_h}{\partial z} = (\chi_o - \alpha_h) D_h + C\chi_h D_o \tag{2.43}$$

In general χ_h and $\chi_{\bar{h}}$ are not equal in a non-centosymmetric crystal such as the zinc-blend structure except in special cases (such as the *00l* reflection).

Let X be the complex reflection coefficient

$$X = \frac{D_h}{D_o} \tag{2.44}$$

Then

$$\frac{dX}{dz} = \frac{1}{D_o}\frac{\partial D_h}{\partial z} - \frac{D_h}{D_o^2}\frac{\partial D_o}{\partial z} \tag{2.45}$$

substituting into (2.43) we arrive at

$$\frac{dX}{dz} = \frac{i\pi}{\lambda\gamma_o}\left\{C\chi_{\bar{h}}X^2 + \left(\chi_o - \frac{\gamma_o}{\gamma_h}\chi_o + \frac{\gamma_o}{\gamma_h}\alpha_h\right)X - C\frac{\gamma_o}{\gamma_h}\chi_h\right\} \tag{2.46}$$

If the crystal contains compositional variations, α_h will be a function of the depth z below the surface. If the crystal is divided into a number of laminae of constant composition, we can solve the equation analytically for each lamina and match the complex amplitude ratios at each boundary in order to attain the reflectively at the surface.

The equation (2.46) can be written as

$$\frac{dX}{dz} = iD\left[AX^2 + 2BX + E\right] \tag{2.47}$$

where $D = \frac{\pi}{\lambda\gamma_o}$,

$A = C\chi_{\bar{h}}$,

$B = (1-b)\frac{\chi_o}{2} + \alpha_h\frac{b}{2}$,

$E = -Cb\chi_h$.

Equation (2.47) can be written now as

$$\frac{dX}{dz} = iDA\left[\left(X + \frac{B}{A}\right)^2 - \frac{B^2}{A^2} + \frac{E}{A}\right] \tag{2.48}$$

After solving this equation we obtain

$$X = \frac{k\sqrt{BB-EA} + i(Bk+E)\tan\left(D\sqrt{BB-EA}(z-W)\right)}{\sqrt{BB-EA} - i(Ak+B)\tan\left(D\sqrt{BB-EA}(z-W)\right)} \tag{2.49}$$

Assuming that the reflectively is known at a depth $W$and $X(W) = k$.

The boundary condition is that $k = 0$ at a point deep inside the substrate.

$$k \to 0, (z-W) \to \infty$$

$$\tan(a+ib) \xrightarrow[b\to\infty]{} i \qquad \text{if } \operatorname{Im}\sqrt{BB-EA} < 0$$

$$\tan(a+ib) \xrightarrow[b\to-\infty]{} -i \qquad \text{if } \operatorname{Im}\sqrt{BB-EA} > 0$$

We can write

$$X = -\left\{\frac{B + \sqrt{BB-EA}\,Sign\left[\operatorname{Im}\left(\sqrt{BB-EA}\right)\right]}{A}\right\} \tag{2.50}$$

For calculating the reflectivity at the substrate, the equation (2.50) is used. This value serves as a boundary condition for the first epitaxial layer. For calculating the reflectivity at the surface of the layer, the equation (2.49) will be employed, and the process repeated for all the layers in the structure. Finally the intensity ratio R is calculated from :

$$R = \frac{|X|^2}{|b|} \tag{2.51}$$

2.4 Results from the Dynamical Theory

A detailed treatment of the dynamical theory gives a number of important results.

- The full width at half maximum of the Bragg reflection peak is given by

$$\text{FWHM} = \frac{2C(\chi_h \chi_{\bar{h}})^{1/2}}{\sin 2\theta_B}\sqrt{\frac{|\gamma_h|}{\gamma_o}} \tag{2.52}$$

- The integrated intensity of a single crystal rocking curve is given by

$$I = \frac{8}{3}|C|\frac{\chi_h}{\sin 2\theta}\sqrt{\frac{|\gamma_h|}{\gamma_o}} \tag{2.53}$$

(In case of neglected absorption)

Note, that for the dynamical theory the intensity is proportional to the structure factor, unlike for the kinematical theory where intensity is proportional to the square of the structure factor.

- The refractive index of the crystal causes a shift in the position of the Bragg peak compared to the position from the Bragg law. The mentioned shift is given by

$$\Delta\theta = \frac{|\chi_o|}{2\sin 2\theta}\left(1 + \frac{\gamma_h}{\gamma_o}\right) \tag{2.54}$$

When two wavefields propagate within a crystal then oscillations known as Pendellösung fringes appear on the rocking curve. The angular spacing of the Laue case Pendellösung fringes is given by :

$$\delta\theta = \frac{\lambda(\gamma_o|\gamma_h|)^{1/2}}{Ct(\chi_h \chi_{\bar{h}})^{1/2}} \tag{2.55}$$

where t is the thickness

The length $\frac{\lambda}{C}\sqrt{\frac{\gamma_O|\gamma_h|}{\chi_h\chi_{\bar{h}}}}$ is known as the extinction distance and corresponds to the separation of the maxima of the wavefield excited within the crystal due to the interference of the two Bloch waves propagating in the crystal.

- Finally, the thickness fringe period for Bragg case is:

$$\delta\theta = \gamma_h \frac{\lambda}{(t\sin 2\theta_B)} \tag{2.56}$$

and is independent of scattering power.

Chapter 3

Bragg case interferometer

As seen from recent achievements of the Double Crystal Diffractometry; the study of the perfection or composition measurements of closely lattice matched epitaxial layers is now commonplace. The devices that attract most attention today consists of complicated structures with many and thin layers. Diffraction profiles from such structures are extremely complex and the only way to interpret such rocking curves is by simulations[1].

The effects that occur in diffraction from such layers are similar to the analogous optical interference effects. For example, oscillations can be detected in the wings of a single epitaxial layer peak - known as Bragg case Pendellösung oscillations - which are subsidiary interference maxima. Rocking curves like that, have been reported by many scientists [2-4]. The period of the subsidiary oscillations can be used to give a direct measurement of the layer thickness. The equation for Bragg case Pendellösung fringes[4] is given by:

$$\delta\theta = \frac{\lambda \sin(\theta_B + \phi)}{t \sin 2\theta_B} \tag{3.1}$$

where t is the layer thickness

λ the X-ray wavelength

θ_B the Bragg angle

and ϕ the angle between the Bragg plane and the crystal surface

In this chapter the similar phenomenon that is observed in an ABA structure (where a thin layer of composition B is sandwiched between two layers of composition A) will be expounded. For a short X-ray wavelength, such as used for X-ray crystallography this kind of structure acts as a Bragg case X-ray interferometer.

Such sandwiches occur quite commonly in quantum well devices and semiconductor lasers; where device performance (e.g. threshold current) depends on how accurately the thickness of the layers is manufactured. In addition current interest in strained layer systems for high electron mobility transistors has led to a large number of studies of the rocking curves of extremely thin InGaAs layers sandwiched between GaAs or AlGaAs layers. Today, Bragg case interferometry is commonly thought of as a very strong method for industrial quality control of these structures.

X-ray interferometry is not a new idea; the first X-ray interferometer (Bonse and Hart, 1965[6]) was fabricated from highly perfect silicon and operated in Laue geometry. Later in 1983 Barbee and Underwood[7] used a solid state Fabry-Perot etalon which worked in the soft X-ray region.

The most important interference effect is the modulation of the basic peak which in some cases leads to peak splitting. There are two types of fringes with different periods in that modulation. The one corresponding to the thickness of the cap layer A and the other corresponding to the thickness of the layer B (interference fringes). A direct method of thickness measurement of both of the layers can be provided by using equation (3.1).

The apparent period corresponding to the cap layer shows a slight divergency from the Bragg case Pendellösung period.[8]. In figure 3.1 we can see that the gradient is not corresponding to the Pendellösung spacing. This arises because of the beating of the two periods when cap and layers thickness become nearly equal. Use of Fourier transformation techniques[20] shows that the individual periodicities do correspond to equation 3.1

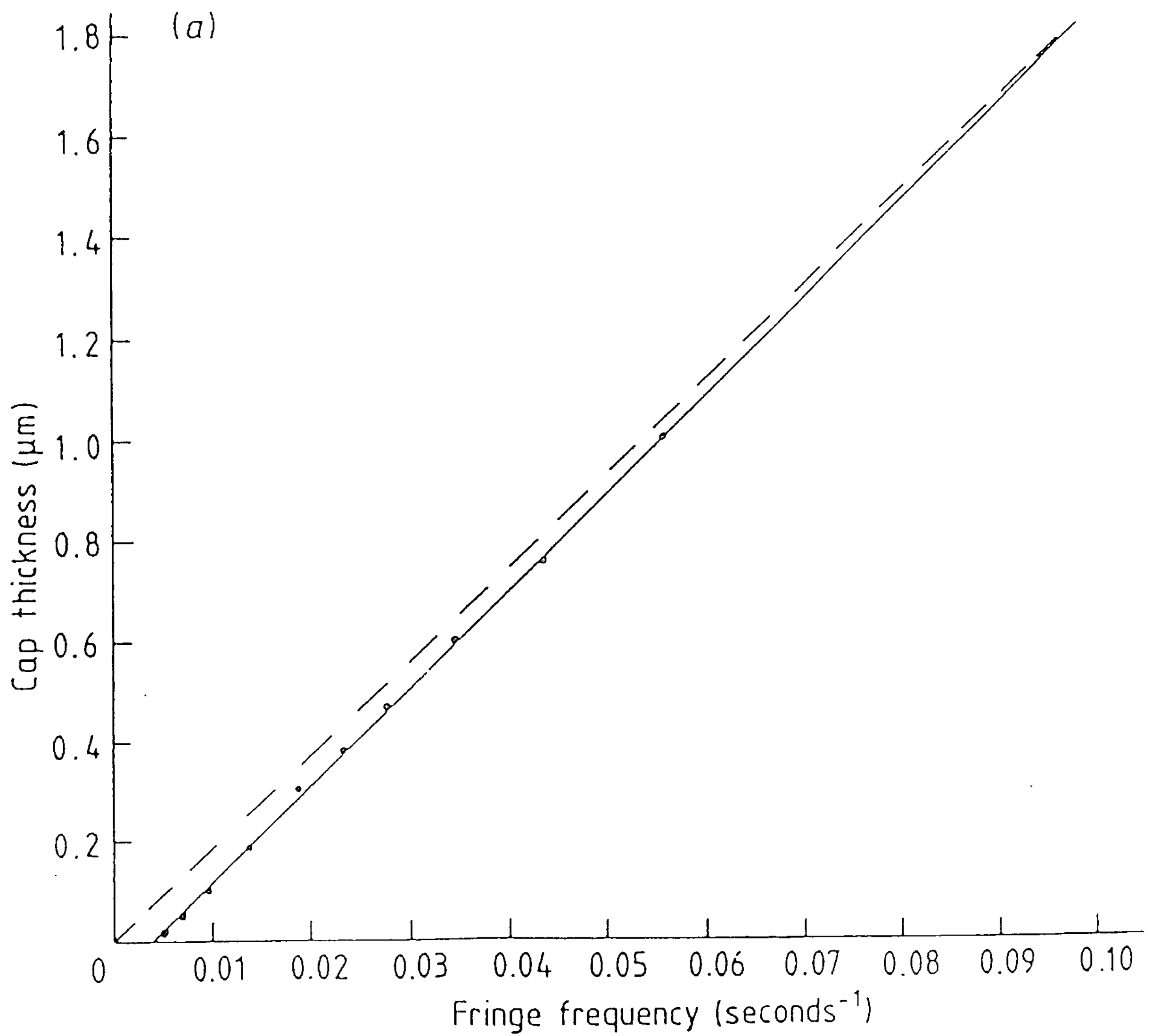

Figure 3.1:
The gradient is not corresponding to the Pendellosung. This arise because of the beating of the two periods when cap and layers thickness become nearly equal.

(After Halliwell)

The interference fringe period can sometimes provide us with sub-monolayer resolution[9]. That is because the position of the interference peak is extremely sensitive to the phase shift which arises from the layer B.

Considering a specimen of structure ABA; the regions of material A, with identical spacing d (say GaAs), contain N_1 and N_2 planes respectively. Layer B separates the two regions A; it has different lattice spacing from A and thickness nd+Δd.

If $\Delta d = 0$, $\alpha = \frac{\Delta d}{d} = 0$ which we call the **in-phase** condition

However there is no interference effect from the cap layer.

If $\alpha = \frac{1}{2m}$ we call that the **out-of-phase** condition

(m is the order of the Bragg reflection)

Holloway[10] examined, according to the above, two types of structure based on the outer (cladding) layers thickness, when they are different (structure A) or the same (structure B). Experimentally, in both structures the cap layer should be thick enough to give a Bragg peak with reasonably intensity and sharpness and thin enough to transmit a substantial fraction of the incident energy to the underlying thick cladding layer. It is worth noting that fringe visibility in systems containing only very thin layers, is low.[11]

By using the kinematical approach, the interference effect is elucidated. In the two structures that Holloway discussed, the dynamical theory is approximated by simple kinematical theory (Fig. 3.2). The most significant difference is a shift of the profiles to slightly larger incident angles. This occurs because of the phase change on scattering that gives refractive index, which is not calculated in the kinematical approach.

It should be mentioned that irrespective of the thickness of the two interfering regions, the diffraction patterns repeat themselves when the

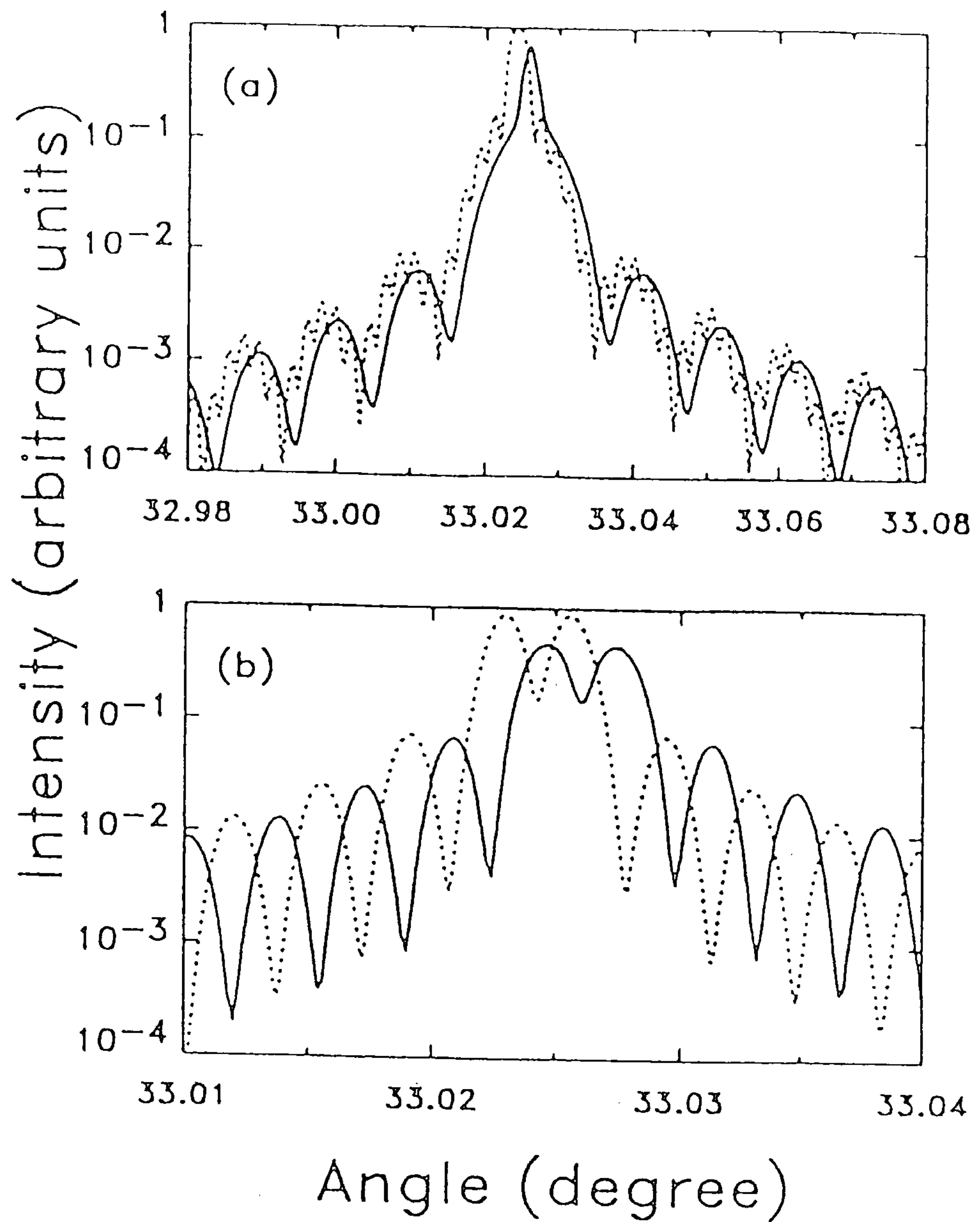

Figure 3.2:

Comparison of kinematical (dashed line) Darwin-Prins (solid line) calculations for (400) reflections from two structures in the out-of phase condition.

(a) Structure A.

(b) Sructure B.

(After Holloway)

separator is increased by multiples of d/m. For (004) reflection $d/m = a_o/4$, and a_o is the lattice constant (of GaAs in this case).

The transition from the in-plane condition (Figure 3.3) shows how sensitive the rocking curve profile can be to the phase shift. In the structure A, we can see clearly the two sorts of fringes. The spacing of the subsidiary maxima of the long period fringes does not depend on the thickness of the separator layer[8], on the other hand the visibility of these fringes is a periodic function of the phase shift of the separator layer[10].

In structure B the transition from the one condition to the other puts a notch into the convoluted profile at the main Bragg peak. Additionally, this transition causes a doubling of the spacing of the subsidiary maxima from that corresponding to a combined set of 2N planes to that corresponding to the individual region with N planes.

As we can see in Figure 3.4, by increasing the thickness of the separator, the two GaAs regions diffract out-of-phase; there is an evident reduction of the sensitivity of the peak profile when the thickness of the separator is changed.

Examining the sensitivity to the precision of the separator's thickness measurement, we can consider the worst and best cases.

In what can be called the best case, we assume that we do not have broad features such as Compton and diffuse thermal scattering and that there is not significant masking by background scattering. The sensitivity of the method is limited by the experimental uncertainty to a change in separator thickness that will give a root-mean-square (rms) change of σ in the calculated log intensity

$$\sigma = \log\left(1 + \frac{1}{\sqrt{N}}\right) \tag{3.2}$$

where N the number of counts at each point.

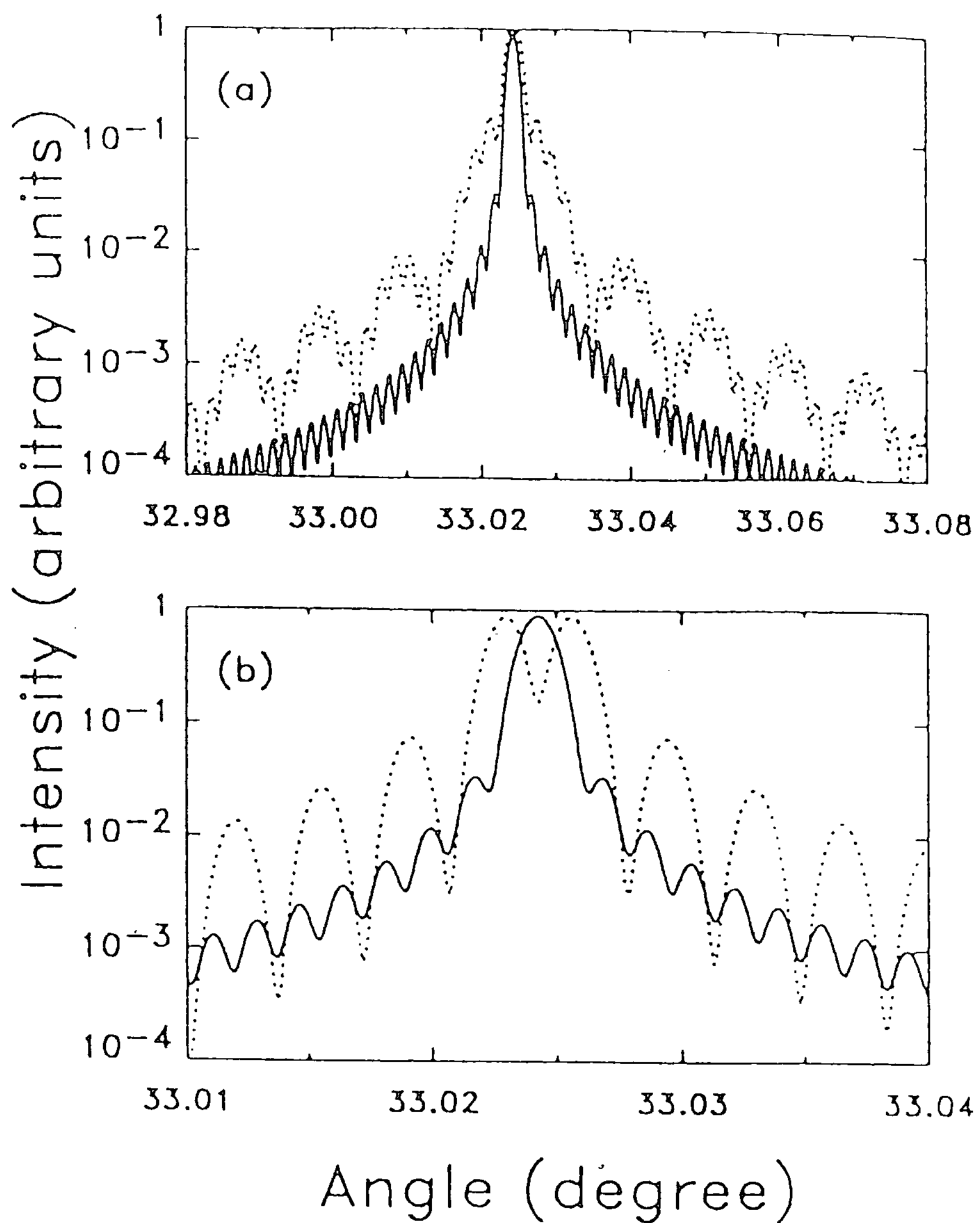

Figure 3.3:
Kinematic calculations of (400) reflections from two structures. The solid lines are for the in-phase condition and the dashed lines are for the out-of-phase condition.
(a) Structure A.
(b) Sructure B.

(After Holloway)

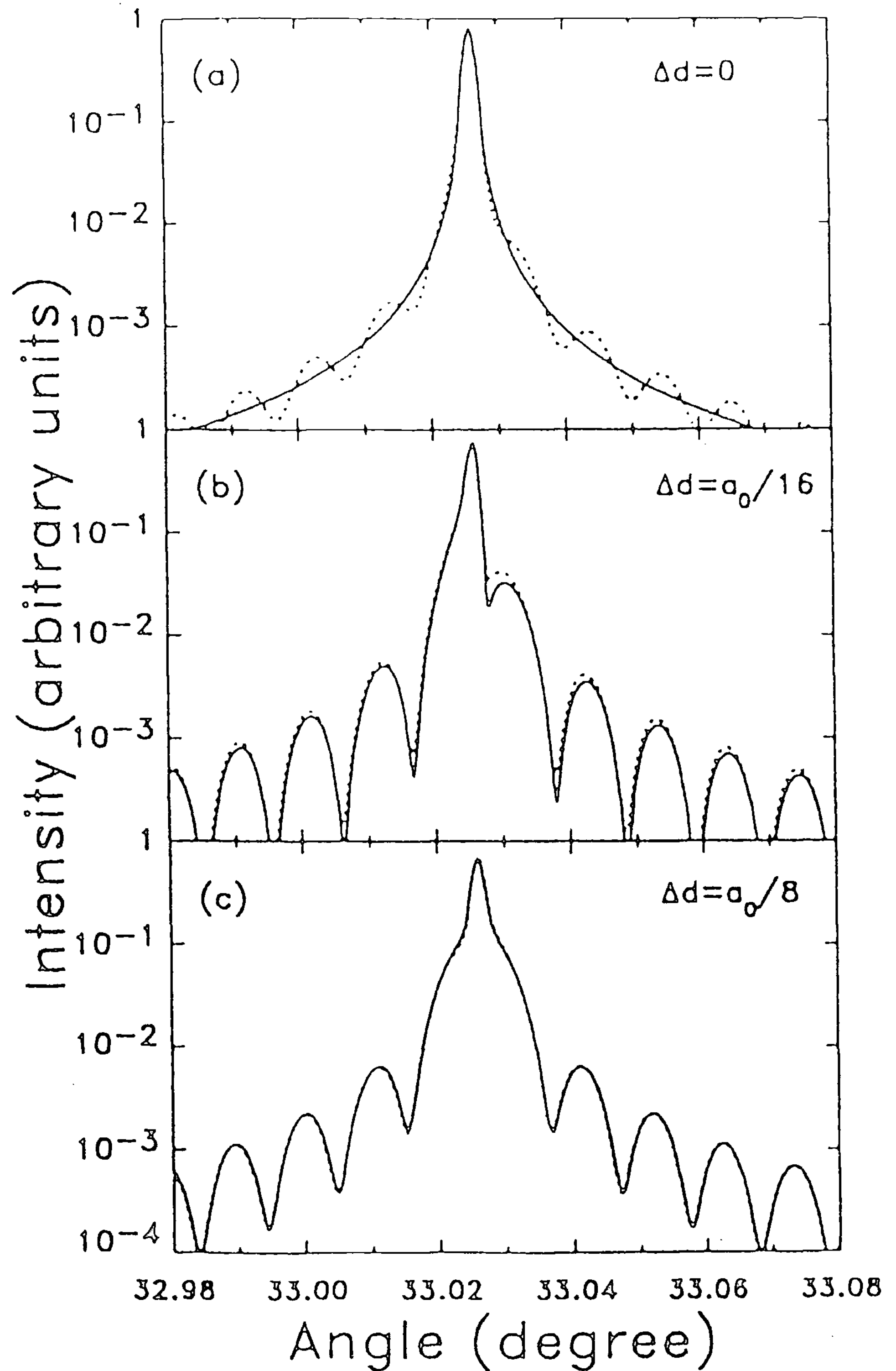

Figure 3.4:
Darwin-Prins calculations for (400) reflections from structure A. In each case the solid line is for the nominal value of the separator, Δd, and the dashed line is for an increase in Δd by 0.01.

(a) Δd=0

(b) Δd=α_0/16

(c) Δd=α_0/8. The two curves are almost coincident. (After Holloway)

By definition, the worst case is when we can just make the distinction between the in-phase and the out-of-phase condition. As it is mentioned above, the fringe effect is periodic in relation to the change of the separator of d/m. So we may expect to measure separations of some fraction of this value. Although the precision of the measurement of the separator's thickness is $\pm d/4m$ there is an uncertainty of some multiples d/m. The latter statement should not trouble us at all when the numbers of planes in the separator layer are precisely known (RHEED oscillations during the growing or with transmission electron microscopy).

If the lattice spacing of the separator is $d_{sep} = d + \delta d$ then each plane of separator contributes $m\left(1+\frac{\delta d}{d}\right)$ period to the change in the diffraction pattern. That means that for every new period $\Delta t_{sep} = \frac{d/m}{\delta d/d}$ thickness is required. The magnitude $(\delta d/d) \ll 1$ will be related to the lattice mismatch. In other words, a Bragg plane spacing of the separation is equivalent to a thickness $d(1+m^*)$ where m^* is the effective mismatch and $\Delta t_{sep} = d/4m^*$.

The connection of Bragg interferometer theory with the effective mismatch gives a new meaning to the topic. Most of the devices which use the interferometer system contain a very highly mismatched spacer layer and resulting misfit dislocations are very significant for the lifetime and the transport properties of the devices.

The strain energy due to a coherent interface increases with epilayer thickness but when the thickness exceeds a critical amount, relaxation of the strained layer may occur. The percentage of the relaxation affects the characteristics of the rocking curve dramatically. Both the positions of the Bragg peaks of the thin strained layers and the capping layer are changed.

Consider two regions of GaAs separated by a thin layer of $In_xGa_{1-x}As$ (x=0.2)[10]. The lattice spacing of InGaAs (relaxed 5.7345Å) is greater than that of GaAs (relaxed a_{oGaAs}=5.6535Å). When the sample is completely unrelaxed

the InGaAs expands normal to the interface. The lattice constant parallel to the interface is $a_{//} = a_{oGaAs}$ =5.6535Å and the lattice constant perpendicular to the interface is $a_{\perp}$ =5.8103[12]. For a symmetric (004) reflection the InGaAs Bragg peak occurs at a lower angle from that of the GaAs substrate and cap peak. The lattice misfit is quite modest (1.4%) according to other commercial systems. When the sample is relaxed either fully or partially the Bragg plane peaks start to move to higher angles.

The mismatched layer in an interferometer structure specimen leads to the "alliasing" effect described above. Because of this, in near matched systems of AlGaAs on GaAs, low sensitivities to thickness changes have been reported[13,14]

These expansions or contractions of the lattice spacing normal to the interface alter the thickness of the separator layer. For a fully relaxed separator, the above phenomenon gives an increase of 0.014 a_{oGaAs} for each unit cell of alloy of the intermediate layer. For a fully unrelaxed separator it doubles the amount. In estimations like the above, we need to know accurately the relaxed lattice constant of the separator, which is a function of the composition of the separator. In the previous example an uncertainty of 1% of the In composition (x=0.2±0.01) corresponds to an uncertainty of 5% to the lattice constant[10].

It is possible to have a rocking curve with two GaAs peaks; one from the cap peak and one from the substrate, when one of the two interfaces in ABA structure is fully relaxed and the other is almost conformally strained. Of course, in order to have a better view of the relaxation of the sample, it is necessary to use asymmetric reflections. However, the presence of the two peaks from the GaAs is a "valuable indication of the presence of the phenomenon"[9].

In some interferometer structures a weak system of fringes has been reported. This system of fringes has been attributed to the effect of a thin damaged layer between the substrate and the buffer layer. Tapfer and Ploog[15]

have reported the above phenomenon in a study of thin sandwiched strained layers of InGaAs on GaAs. Green, Tanner and Kightley[11] having studied a more complicated structure of AlGaAs, InGaAs and GaAs observed this system of finges and attributed it to the existence of a thin (1nm) mismatched layer of $GaC_{0.016}As_{0.984}$ located at the interface of the GaAs buffer layer and the GaAs substrate.

In the majority of the cases the above mentioned layer is created under some conditions of MOVPE growth[16]. The presence of this thin interface layer was observed independently by using transmission electron microscopy[11].

A very clear view of the phenomenon can be given by a theoretical example which can be found in the paper by Tanner[9] of a 0.5μm InGaAS on a substrate of InP and capped by 0.5μm of InP. In figure 3.5, we can see two profiles of the sample. The dashed curve comes from the diffraction of the above sample with abrupt interfaces. The solid curve takes place when a sample has 0.3nm of InGaAs at the interface between the epitaxial layers.

In all the above examples the major change in the rocking curve occurs in the modulation of the substrate peak.

The analysis with the best accuracy, particularly for an indefinitely thick substrate, is achieved by simulating the experimental profile. The RADS simulation program from Bede Scientific is based on the Takaki-Taupin theory (see next chapter). In other works[10], Darwin-Prins equations dynamical theory has been applied. Also, Fourier transformation analysis has been applied, in order to extract the periodicity of the fringes. Macander and his co-workers[17] have done this in logarithmic scale. Fourier analysis is a very useful tool especially when we can not have precise determination of the layer's thickness. Hudson[21,22] has studied the precision and problem of this approach in some detail.

The precision in experimental devices seems to be quite satisfactory. Chu and Tanner determined the spacer layer thickness to ±100Å for 1000Å

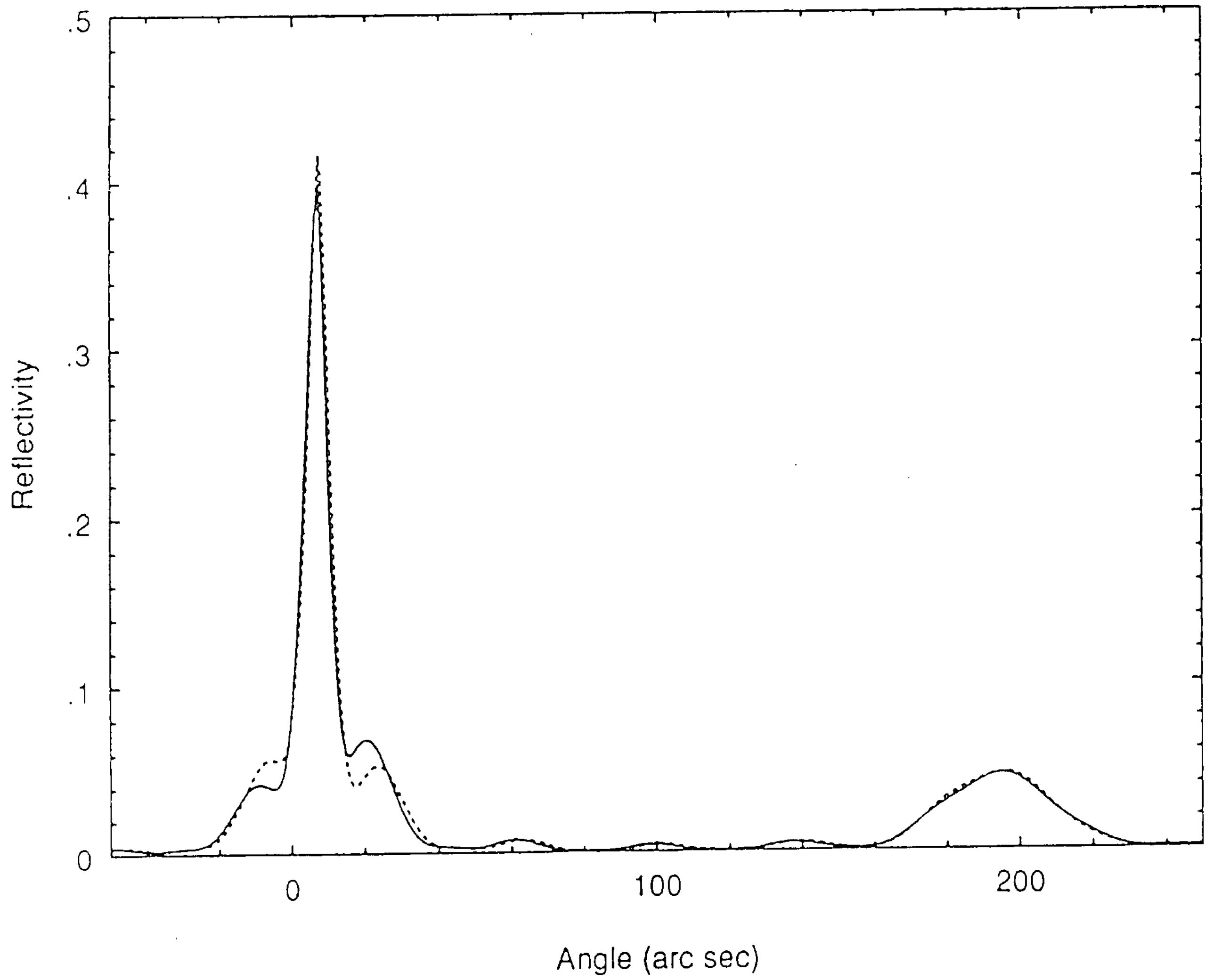

Figure 3.5

GaAlAs in 1986[13] and to ±50Å for a 2500Å GaInAs layer in 1987[18]. The new theoretical works make provision for sub-monolayer accuracy. For a small change of $\pi/16$ in phase to a coherent $In_xGa_{1-x}As$ layer sandwiched between GaAs regions of substrate and cap, we can detect significant differences in the rocking curve, which can provide one atomic change in thickness of the separator (practically that can indeed happen for $x>0.2$)[11]. The theoretical provision also for the best and the worst case that has been mentioned above is ±0.02Å and 0.1Å, respectively.

In order to examine a big area of a specimen with interference structure, Bragg case Moïre topography could be applied. In some cases (like the theoretical prediction that we shall see in the next chapter), the change of the reflectivity can be also so strong that we can have topographs which reveal monolayer precision for the thickness of the separator.

Several attempts have been made by the Durham group in this direction. Chu and Tanner[13] observed contrast changes along thickness fringe contours in an interferometer structure formed by different AlGaAs composition. The fringes that appeared in the spatially extended rocking curve of a topograph were called Moïre fringes because the phenomenon was attributed to the Moïre effects. Cockerton in 1992[19] studied the same phenomenon of Moïre fringes while the specimen was rotated. His results were consistent with the original interpretation.

If the specimen is curved (something very often for strained layer systems) a series of stripes will appear, due to the varying orientation of the specimen. We must emphasise that only curvature in the incidence plane will appear on the topographic plate. There is thus the possibility of distinguishing easily between the changes of intensity which take place either due to interference effects or to the varying orientation of the specimen. However, despite all the above attempts and the theoretical predictions, atomic layer sensitivity topography has not been reported.

Chapter 4

Experiments

The philosophy of these experiments is based on a theoretical example from Tanner's (1993) paper[1].In that example a specimen was considered which consisted of two layers of $Al_{0.3}Ga_{0.7}As$ grown on a substrate of GaAs and separated by a 3nm or 4nm layer of $In_{0.2}Ga_{0.8}As$. A change of 1nm in the separator layer results in a significant change of the diffraction pattern.(Fig. 4.1)

In both cases the peak of the layer splits. The dominant difference between the two rocking curves (dashed-solid) is the great change of reflectivity in both parts of the peak. In the 3nm InGaAs case the above splitting gives the impression of two well separated peaks of almost equal intensity which could easily be considered to come from two thick $Al_xGa_{1-x}As$ layers of different compositions. When such an ambiguity appears in the experimental results, the presence of strong interference fringes on the shoulder of the layer peak removes any doubt.

The samples which are examined in this discussion are MBE-grown samples obtained from the MBE Research Group of University of Glasgow. The samples called B231 and B232 were grown with almost the same structure as the structure of the theoretical example. In addition, there are two thin, 3 monolayer (ML), GaAs layers at the interfaces of the separator which has a thickness of nominally 3nm. These two thin layers of GaAs were grown there in order to have well separated layers and sharp interfaces between them. The difference between the two samples lies in the rotation of one (B232) during

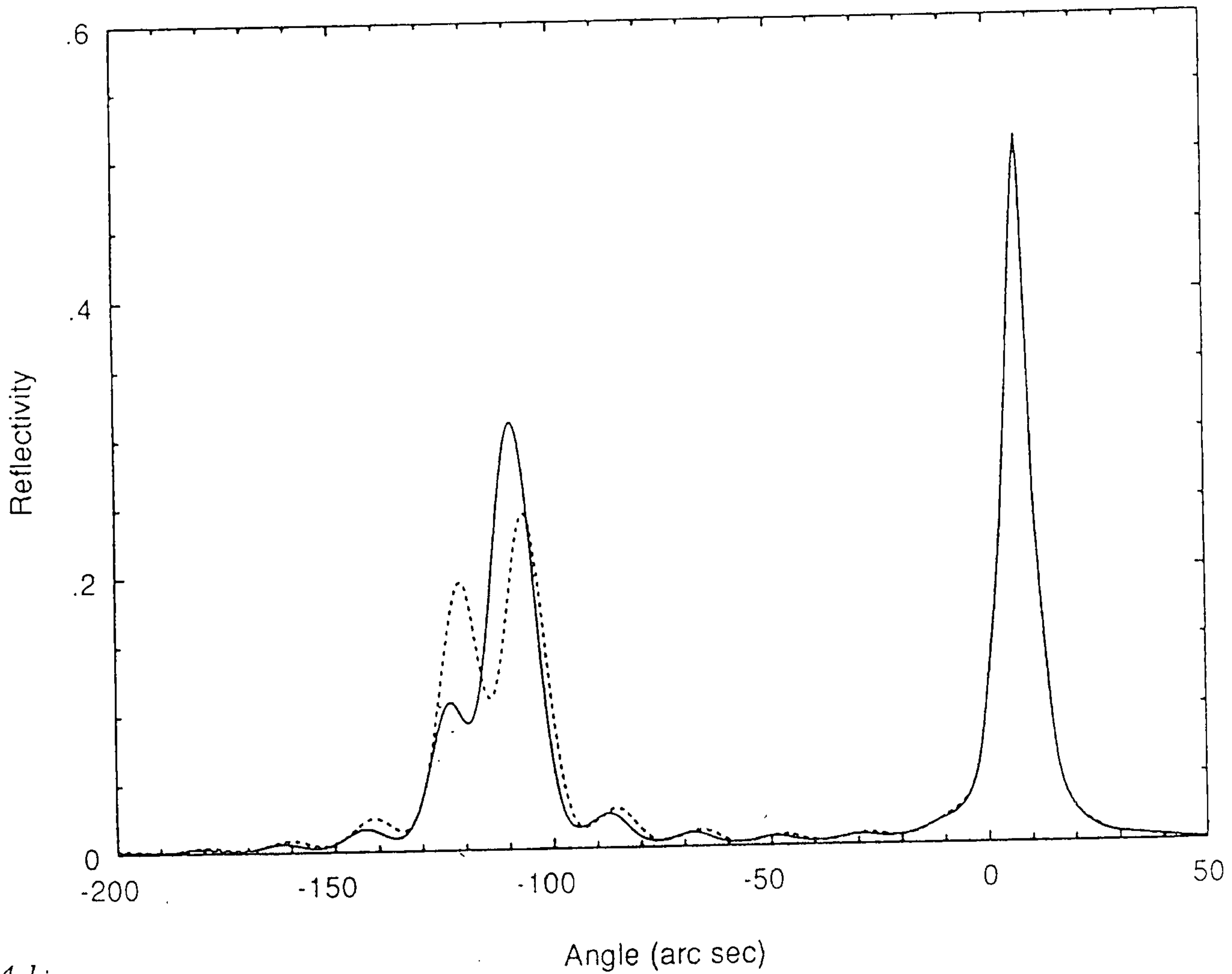

Figure 4.1:
The change of 1*nm* in the separator layer results in a significant change of the diffraction pattern.

the growing of the InGaAs layer. This rotation usually improves the uniformity of the thickness of the layer. Logically the B231 sample is expected to be more suitable for the detection of differences in the thickness of the separator layer.

A check of the reliability of the diffractometer had been accomplished before the experiments started. The check consisted of changing the values of intensity (mA) of the X-ray generator and measuring the intensity of the GaAs substrate peak This procedure was done by scanning first from left to right and then by scanning from right to left. The resulting lines (Fig.4.2) were very linear and from that we could come to a conclusion, namely that the behaviour of the diffractometer was more than satisfactory.

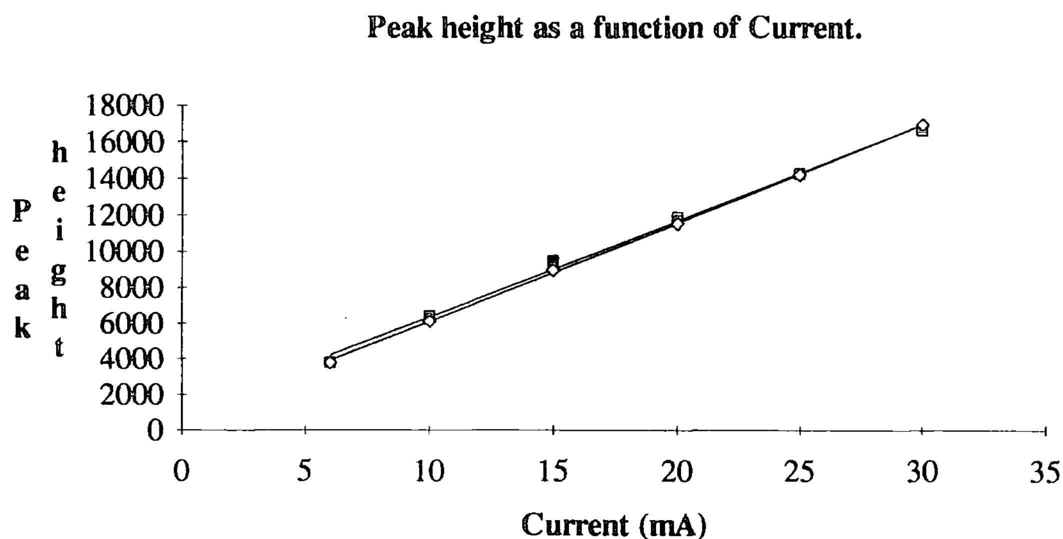

Figure 4.2

4.1 Diffractions

First we obtained a scattering map from the B231 sample. The area being examined was a 25mm×25mm square in the middle of the sample. Thirty eight diffraction profiles were recorded. The distance between adjacent points was 5mm. The counting time was 2 sec per point and the scanning was in steps of 0.5 arcsec. All plots were taken with CuKα radiation and a GaAs reference crystal in the (+,-) parallel geometry. The 004 reflection was used throughout.

The interference behaviour of the samples is obvious from figure 4.3, where a typical rocking curve is illustrated. The Bragg peak of the InGaAs layer did not appear during all the experiments as the scan range was limited. It can be said that the absorption of this layer is negligible. This is one of the most important assumptions in order to take good interferometer results.[2] A strong modulation in the peak of AlGaAs exists in all the rocking curves and a clear split of the peak occurs in many of the profiles. A significant change of the reflectivity which could lead to a complete separation of the two parts of the peak was not recorded. The greatest difference of the modulation of the peak appeared between the rocking curves B231×58 and B231×78. (Figure 4.4) The distance between these two points on the sample was about 28mm ($20\sqrt{2}$).

Using the RADS simulation program from Bede Scientific (based on Takagi-Taupin dynamical theory equations)[3] some very detailed simulations have been performed.(Fig. 4.5) The fit between the experimental and the simulation curves at some points is excellent. From those simulations we saw that:

- The composition of AlGaAs and of InGaAs at all the points of the sample is very constant

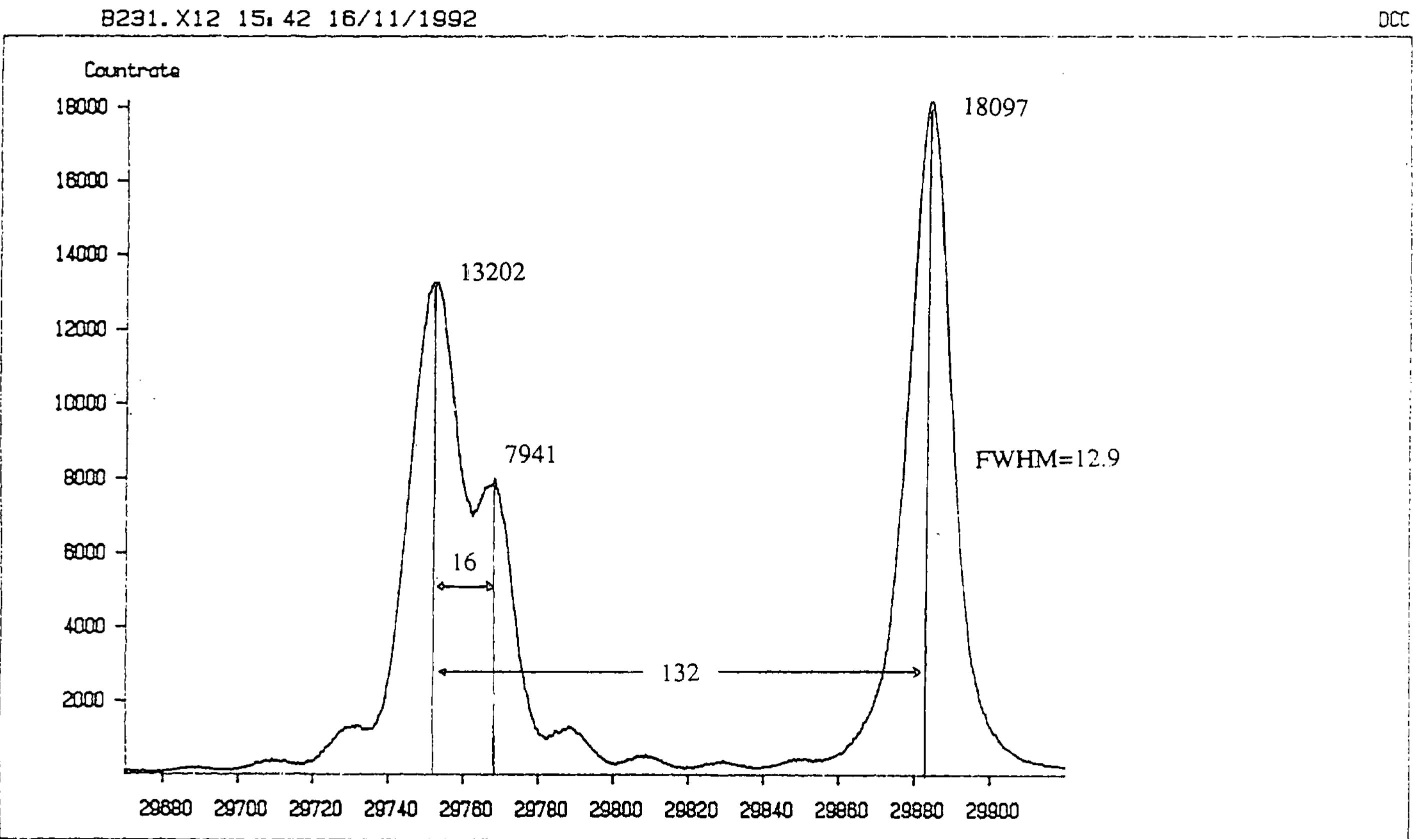

Figure 4.3:
A typical rocking curve of the sample B231 (004 reflection)

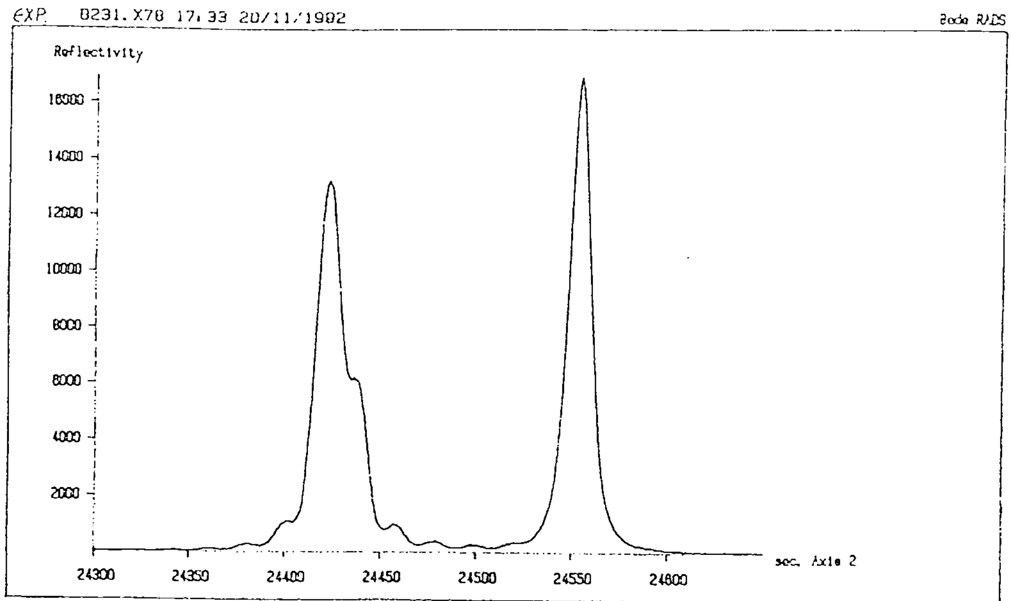

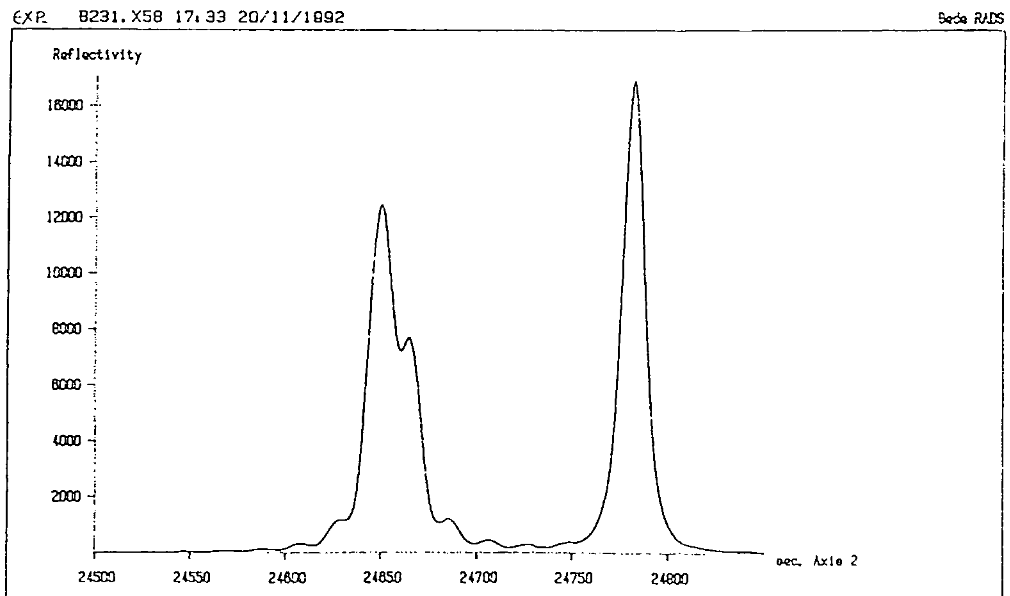

Figure 4.4 i):
Sample B231
Experimental rocking curves B231×78 and B231×58

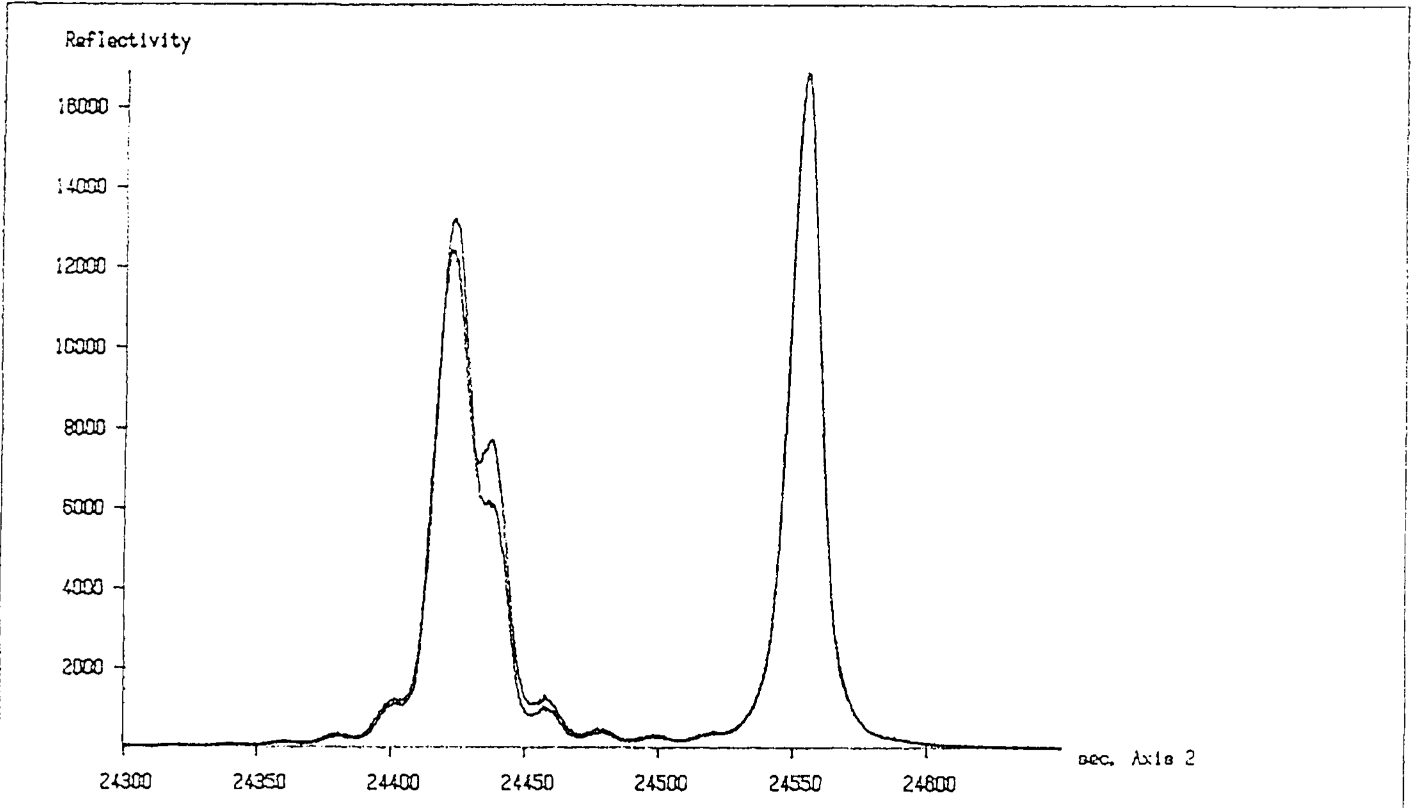

Figure 4.4 ii):
Sample B231
The greatest difference of the modulation of the peak appeared between the rocking curves B231×58 and B231×78

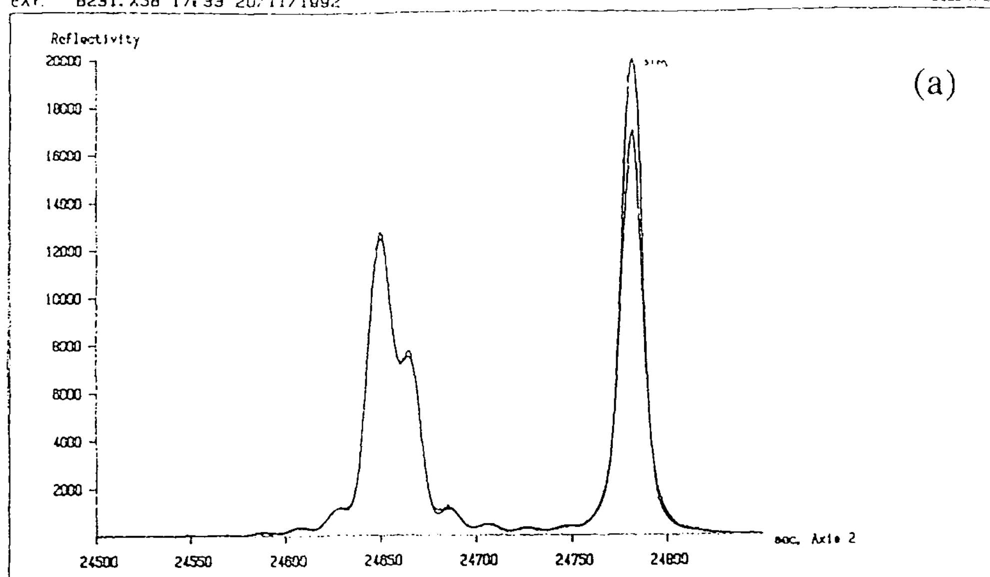

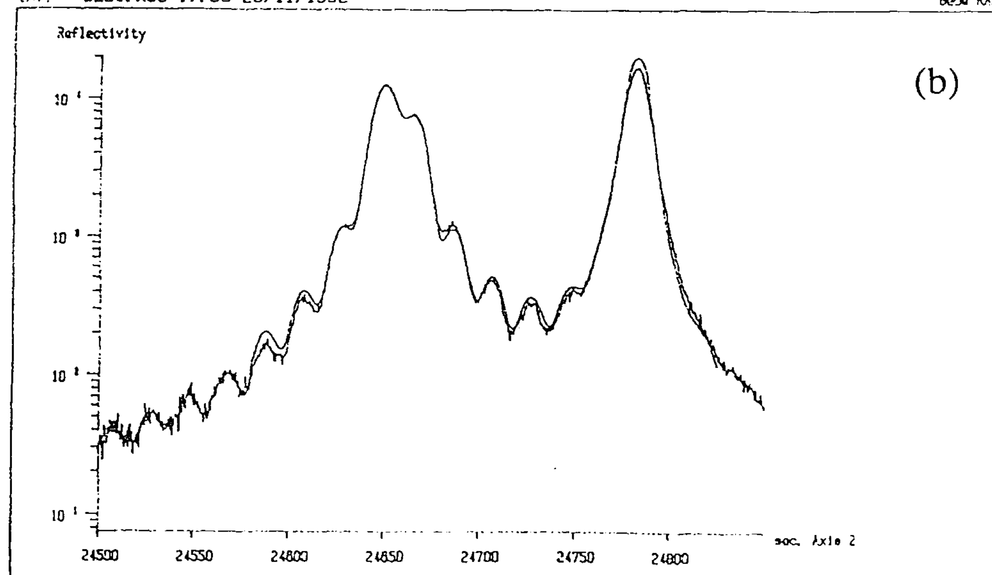

Figure 4.5 i) :

Rocking curves B231×58

Fit between experimental and simulated rocking curve.

a)linear scale

b)logarithmic scale

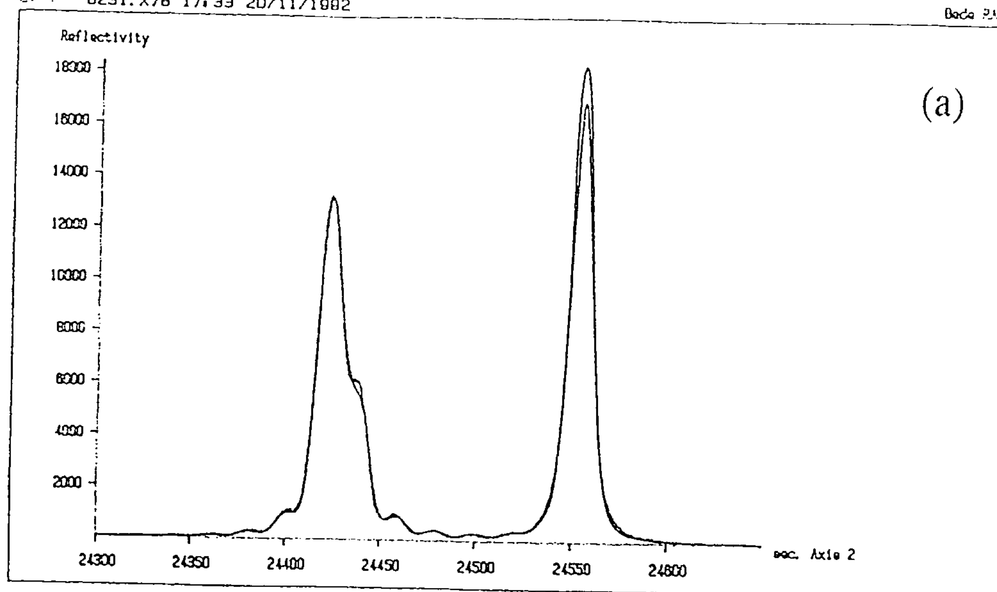

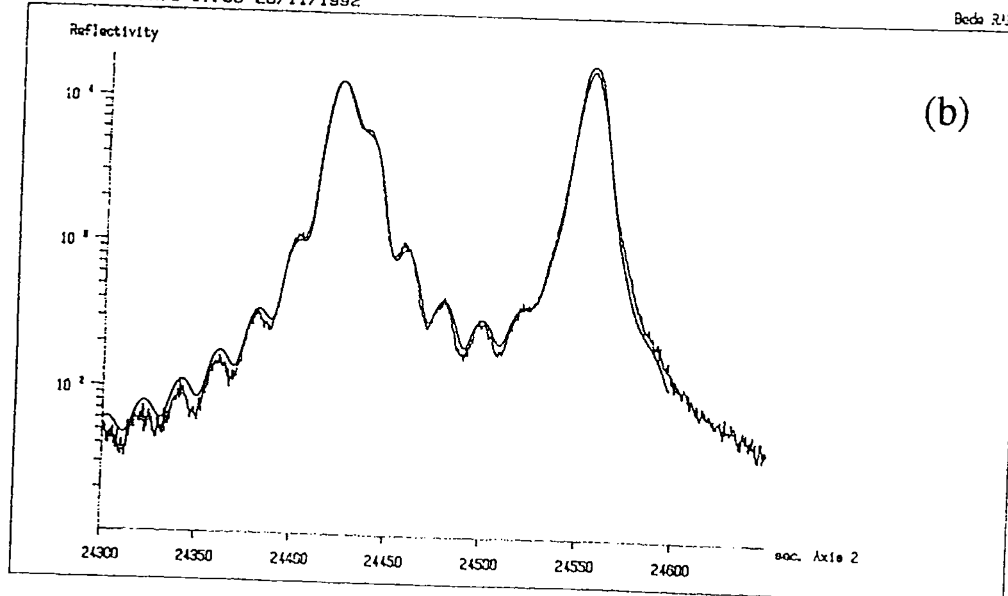

Figure 4.5 ii) :

Rocking curves B231×78

Fit between experimental and simulated rocking curve.

a)linear scale

b)logarithmic scale

- AlGaAs contains 31.5±0.5% Al and its thickness varies from 0.95±0.005 to 0.96±0.005μm
- InGaAs contains 21.75±0.1% In

Simulations of the points with the greatest difference of modulation (B231×58 and B231×78), show that the thickness of the GaAs layers is the same for both of the points (22.65Å≅ 4monolayer) to within ±0.1Å

The only significant reason for the change on the peak modulation is a small variation of the thickness of InGaAs. Very accurate fits of the simulation curves show that the thickness of the separation layer at the point of B231×58 is between 20.6-21.0Å. At the B231×78 point the thickness appeared between 17.0-18.8Å. So the difference in the separator thickness between the two points with the greatest difference in modulation there seems to be submonolayer. The thickness of the separator layer is very uniform indeed. The results from the simulation for these two points is presented in Table 4.1. The accuracy of the dynamical theory predictions in such scale of structure makes the above estimation a time-consuming procedure and gives the limit on the measurement precision.

Table 4.1

	POINT B231×58		POINT B231×78	
layers	thickness (nm)	x	thickness (nm)	x
$Al_xGa_{1-x}As$	970	0 .315	960	0.315
GaAs	2.265	-	2.265	-
$In_xGa_{1-x}As$	2.06-2.10	0.2175	1.70-1.88	0.2175
curvature	264 m		233 m	

Mapping the FWHM of the GaAs peak (Fig. 4.6) it is obvious that the quality of the substrate does not vary substantially. The GaAs FWHM has a range between 15.51 and 13.13 arcsec. Having done the same map for the AlGaAs peak we could observe that the quality of the AlGaAs was

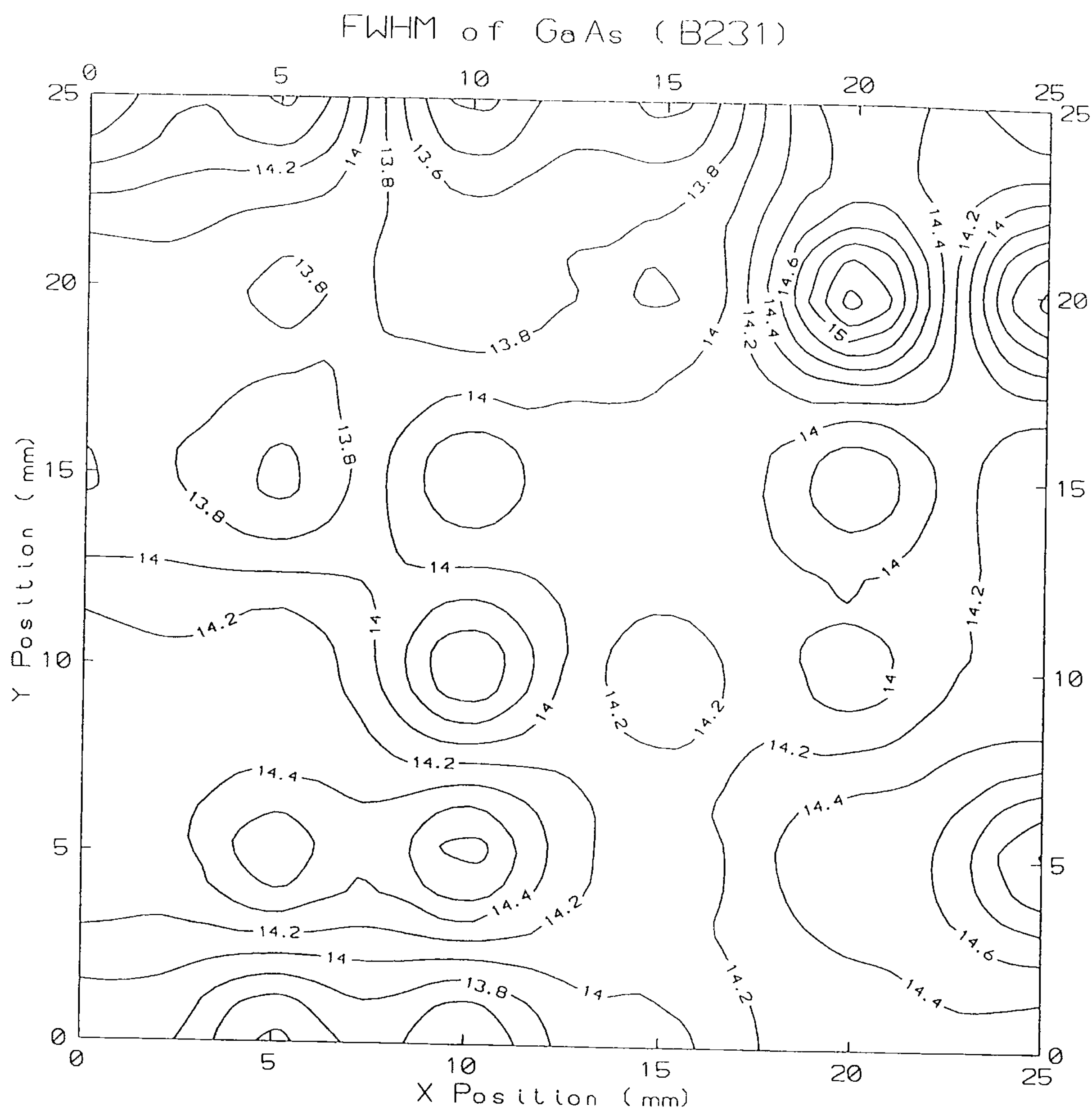

Figure 4.6:
Sample B231. FWHM of the GaAs peak
The quality of the substrate does not vary substantially

progressively changing from one side of the sample to the other.(Fig. 4.7) Since we are aware of the good quality of both the substrate and the separator, we deduce that the irregularity must exist on the highest one of the AlGaAs layers. It is suggested that the lack of a GaAs cap layer at the top of the sample admitted the oxygen of the atmosphere to oxidise the Al of the top layer, but even in that case the oxidation might be expected to be the same across the whole sample surface.

Finally, in order to have a view of the curvature of the sample, a map was drawn plotting the relevant positions of the GaAs peak from point to point.(Fig. 4.8) The sample curvature was found to be very low. The angular distance that the GaAs peak "travelled" during the multiple scanning was 267 arcsec. It is noteworthy, that the area where considerable changes in curvature occur almost coincides with that area where changes occur in the FWHM of the AlGaAs.

The same experiment was carried out on the B232 sample. On this occasion the counting time was shorter (1.3sec) and the scanning was in steps of 0.9 arc sec. The interferometer behaviour of this sample was not so strong as in the previous one, and at many points interference fringes did not appear at all. As the analysis shows the results mentioned above have nothing to do with the rotation during the growth of the separator at the sample B232. It is probably related to the structure of the rest of the sample.

It must be highlighted that at the points of B232 where an interference phenomenon appeared, the rocking curves were similar to the rocking curves from the B231 sample. From these points, the greatest difference at the modulation of the peak was between the rocking curve B232×01 and the rocking curve B232×15 (Fig. 4.9). The distance between these two points is $10\sqrt{2}$ mm.

By simulating many rocking curves from various points from the sample B232 it came up that again the separator layer InGaAs was very uniform. The

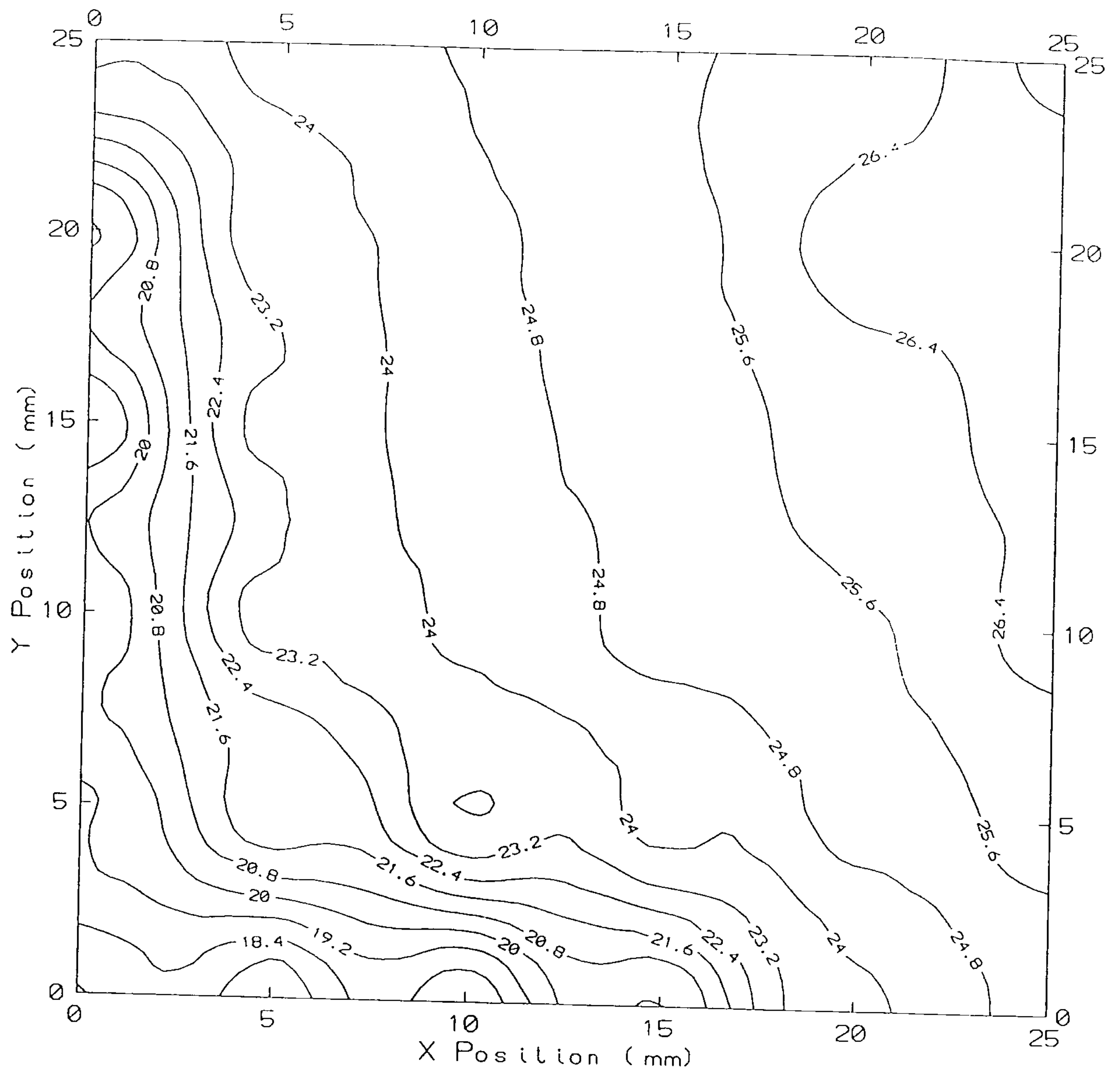

Figure 4.7:
Sample B231. FWHM of the AlGaAs peak
The quality of the AlGaAs was progressively changing from one side of the sample to the other.

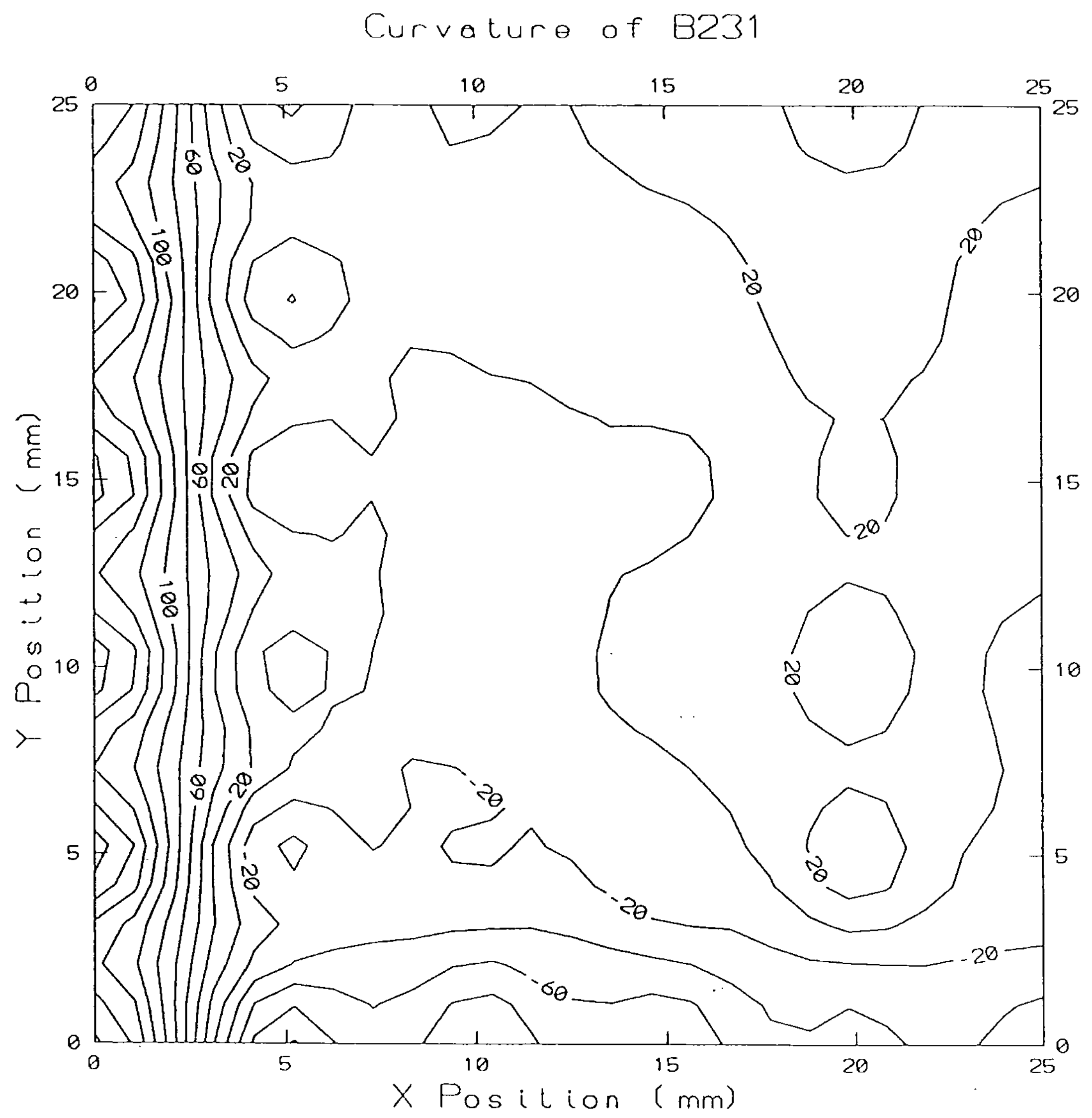

Figure 4.8:
Curvature of the sample B231

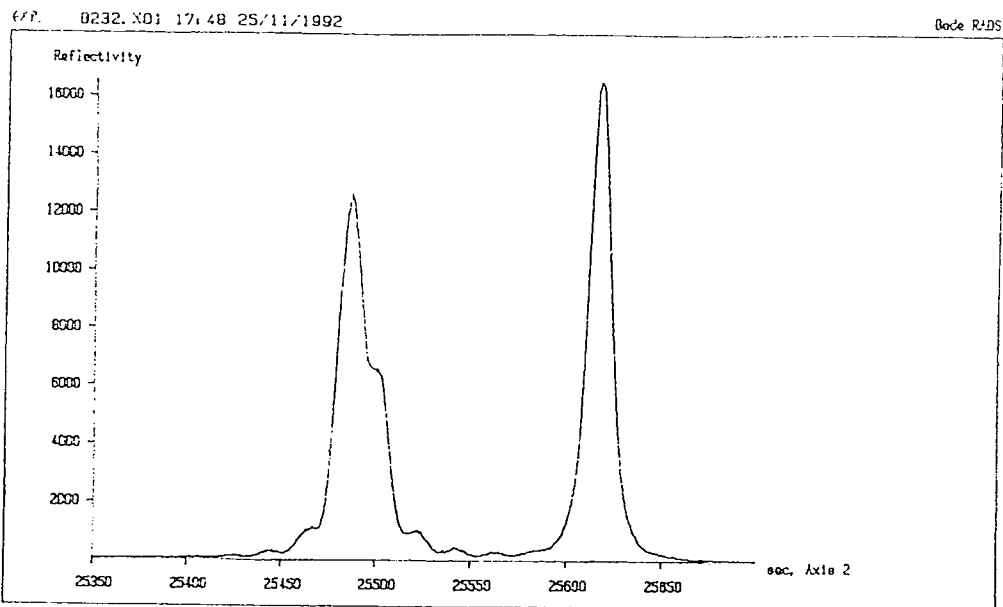

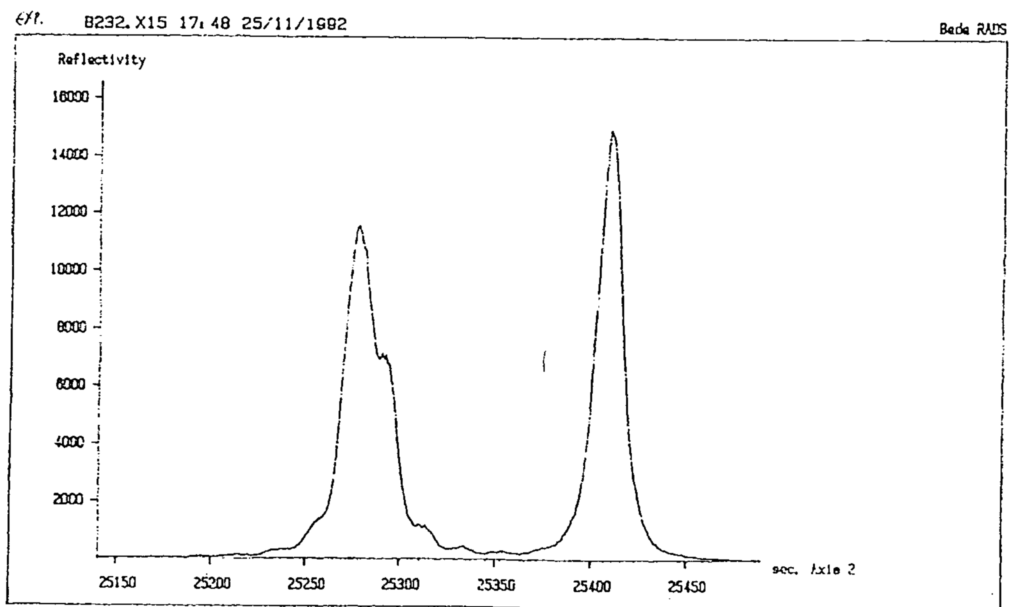

Figure 4.9 i):
Sample B232
Experimental rocking curves B232×01 and B232×15

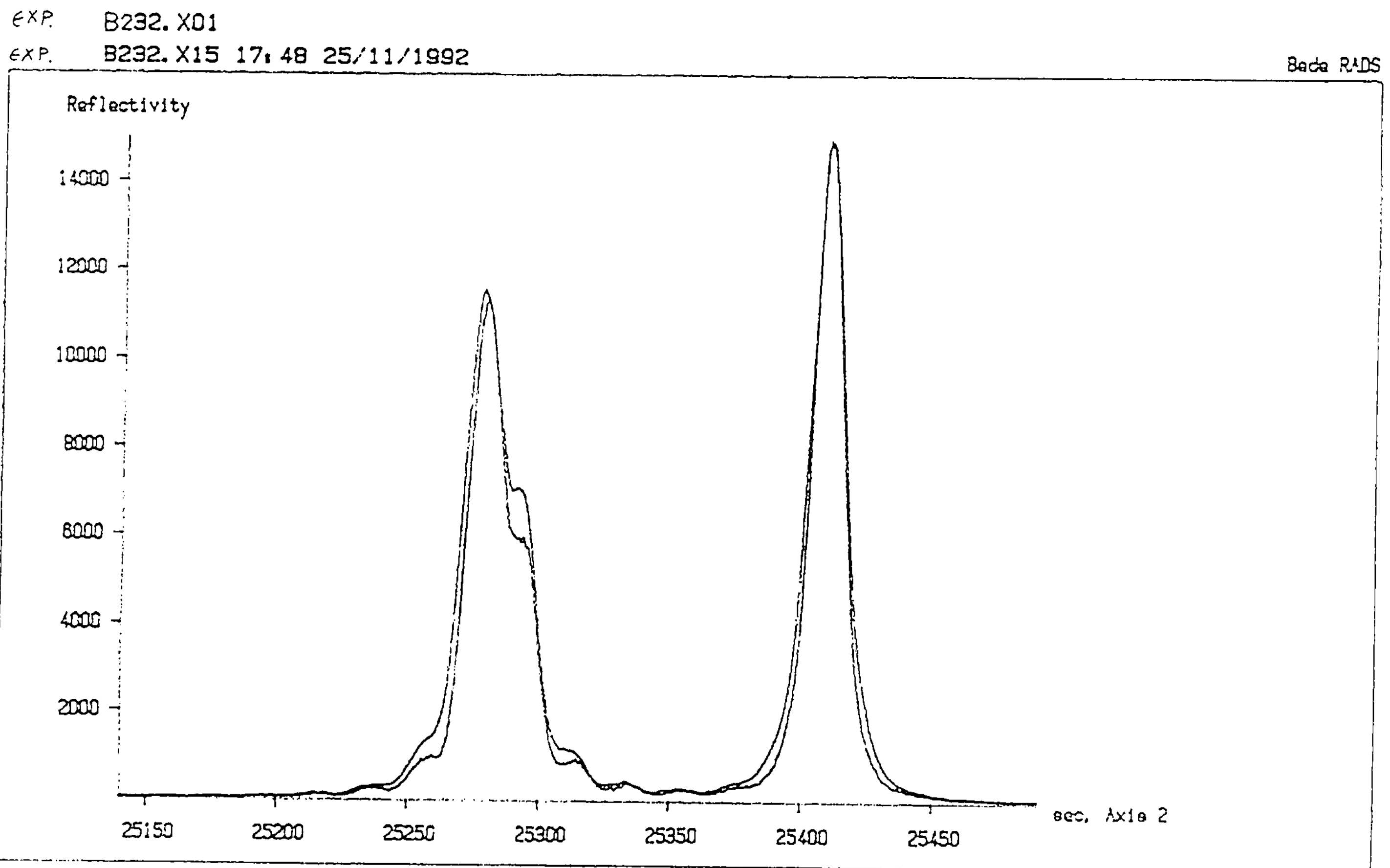

Figure 4.9 ii):
Sample B232
The greatest difference of the modulation of the peak appeared between the rocking curves B232×01 and B232×15

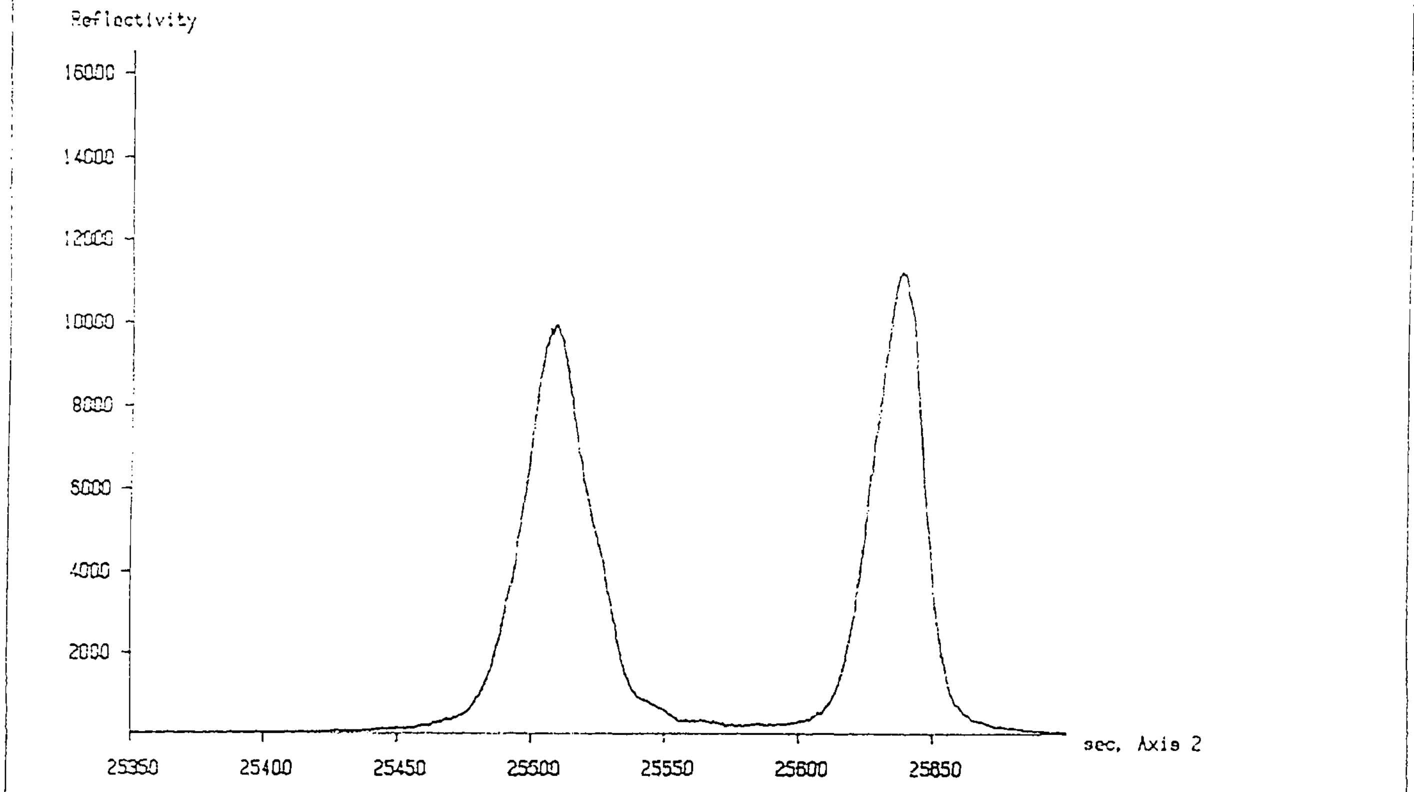

Figure 4.9 iii)
Rocking curve without interference fringes from the sample B232.
There are not interference fringes at the one third of the points on the B232 sample.

range of variation of the thickness of this layer that appeared during the simulation was less than a half monolayer. That was to be expected because of the rotation of the sample during the growth of this layer.

Despite the uniformity of this layer the thickness of all the other layers changed from point to point. The thickness of the two layers of GaAs, that were highly uniform at the B231 sample, 4ML (monolayer), varied from 0 to 3ML in this sample. The lack of interference fringes at one third of the points on the sample can be caused by having layers that are not well defined, and therefore, there are no sharp interfaces between the layers. All those can be explained by the variation of the thickness of the GaAs layers.(Figure 4.9iii, Table 4.3)

Compared to the B231 sample not even the thickness of the AlGaAs layers is constant (0.94-0.97μm). However the contents of the compounds, AlGaAs and InGaAs, are hightly uniform (0.315±0.005 and 0.2175±0.001 respectively).

The differences of the structure at the two points of the figure 4.9ii are shown at next table:

Table 4.2

	POINT B232×01		POINT B232×15	
layers	thickness (nm)	x	thickness (nm)	x
$Al_xGa_{1-x}As$	960	0.3155	940	0.315
GaAs	1.7	-	1.1	-
$In_xGa_{1-x}As$	1.85	0.2175	2.0	0.2175
curvature	264 m		233 m	

Table 4.3

	POINT B232×06	
layers	thickness (nm)	x
$Al_xGa_{1-x}As$	970	0.315
GaAs	0.6	-
$In_xGa_{1-x}As$	1.3-2.0	0.22
curvature	150m	

The fit between the experimental curves and the theoretical curves at points B232×01, B232×15 is shown in figure 4.10

The map of the FWHM of the GaAs peaks (figure 4.11) makes it clear that the substrate quality was rather poor. It is also very interesting that the area of the sample where the FWHM of the GaAs is more than 18arcsec almost coincides with the area in which interferometer fringes did not appear. The best fit structure to these points remains similar to that of the other points. (Tables 4.2,4.3)In figure 4.12 we can see the FWHM of AlGaAs map. It has the same trends as the GaAs FWHM map but is obviously more uniform.

Also a map of the position of the peak of AlGaAs has been drawn. The curvature, as it is seen from the map, is definitely bigger than the curvature at the sample B231. The sample strains in the horizontal direction and remains straight in the vertical direction.(Figure 4.13). However, the diffraction geometry is not sensitive to curvature out of the incidence plane, and thus only twists will appear in the plot.

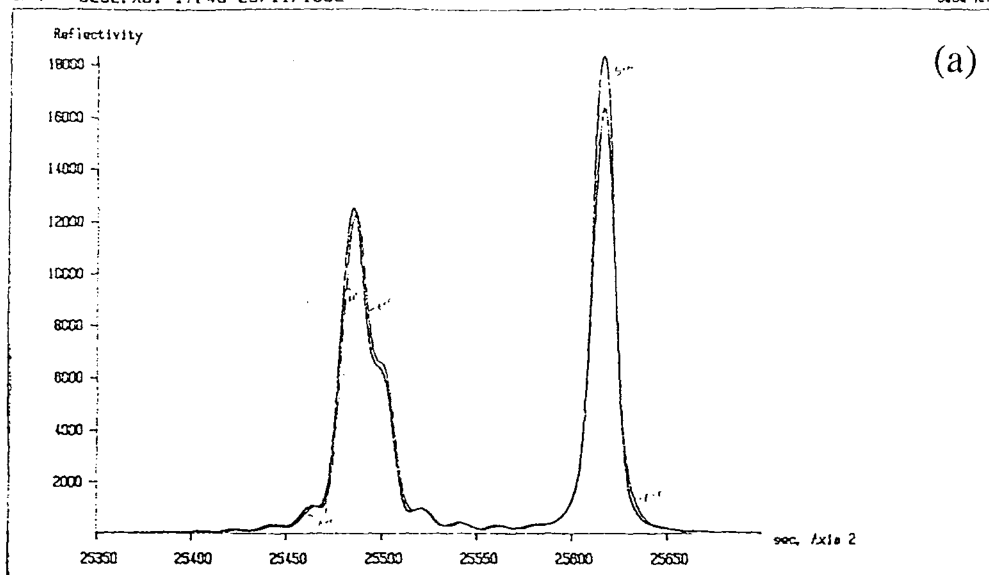

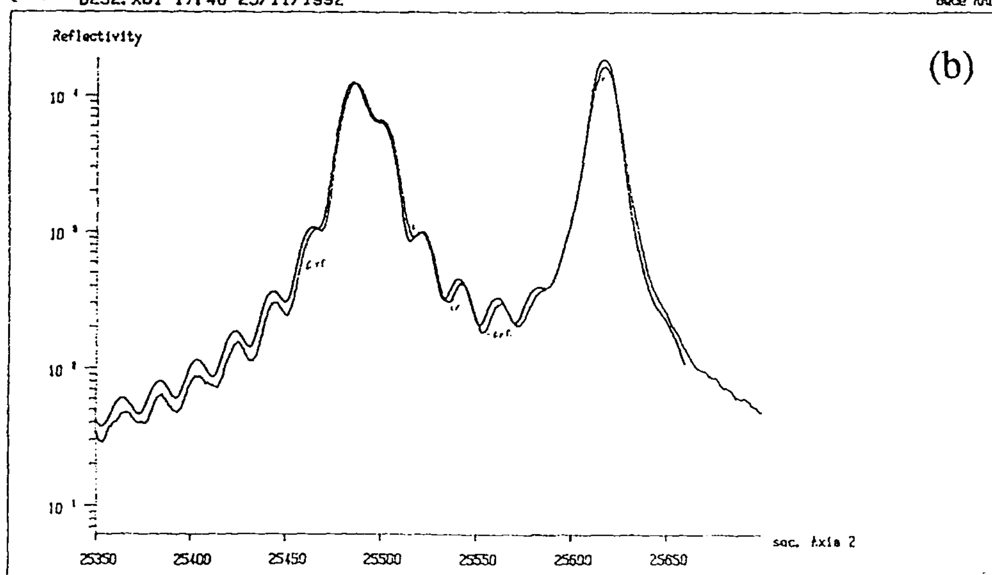

Figure 4.10 i) :

Rocking curves B232×01

Fit between experimental and simulated rocking curve.

a)linear scale

b)logarithmic scale

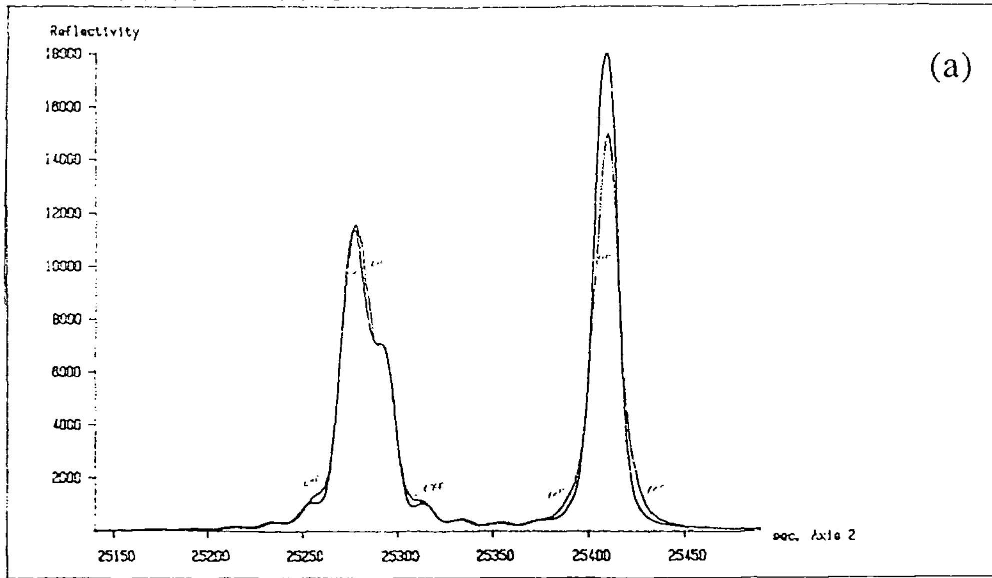

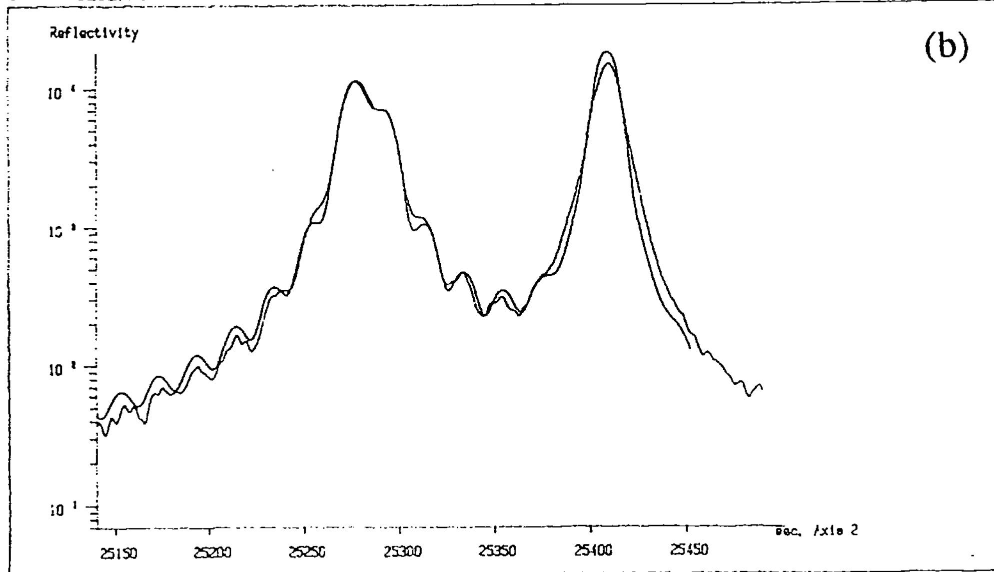

Figure 4.10 ii) :

Rocking curves B232×15

Fit between experimental and simulated rocking curve.

a)linear scale

b)logarithmic scale

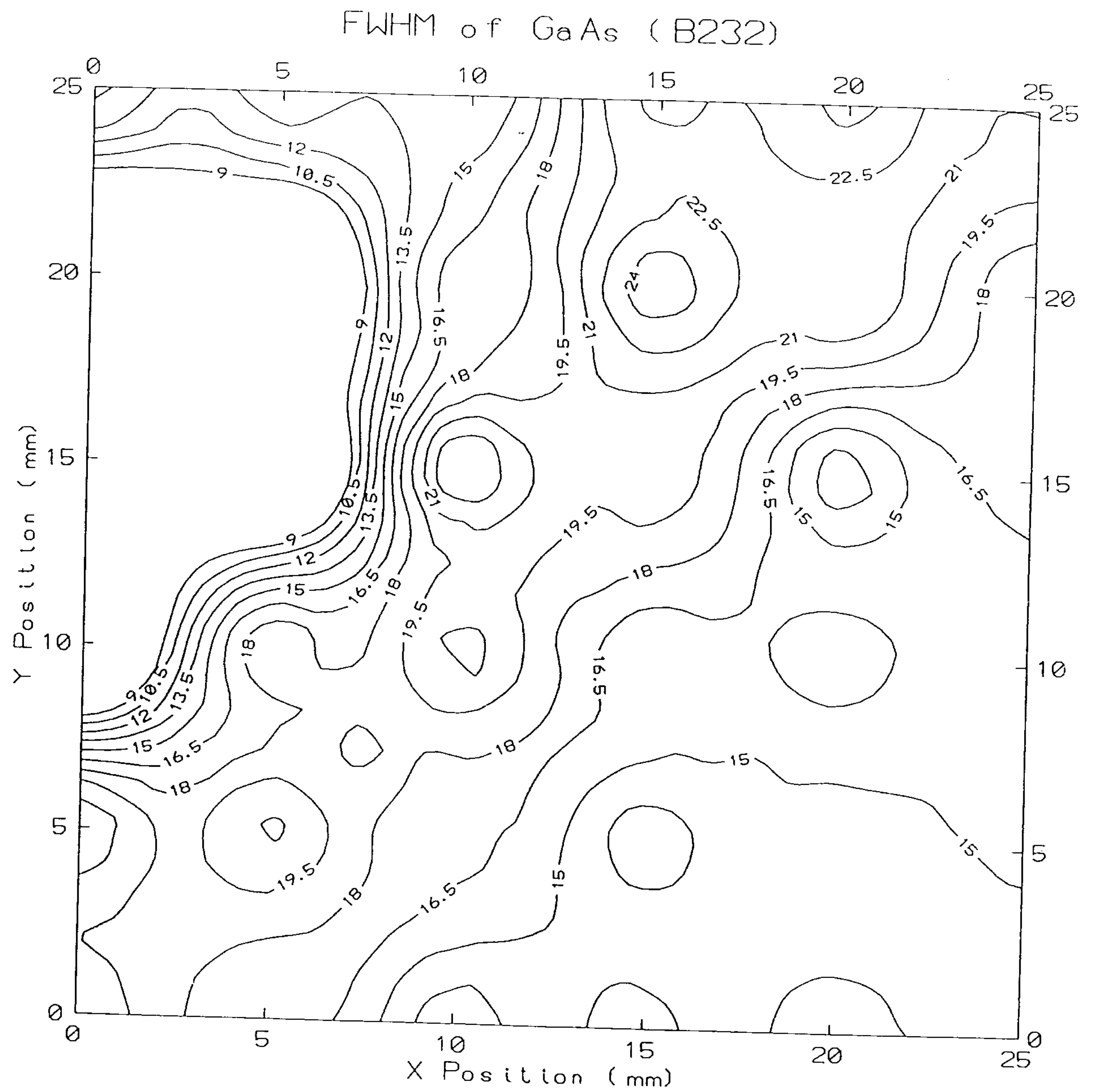

Figure 4.11:
Sample B232. FWHM of the GaAs peak.
The substrate quality is rather poor.

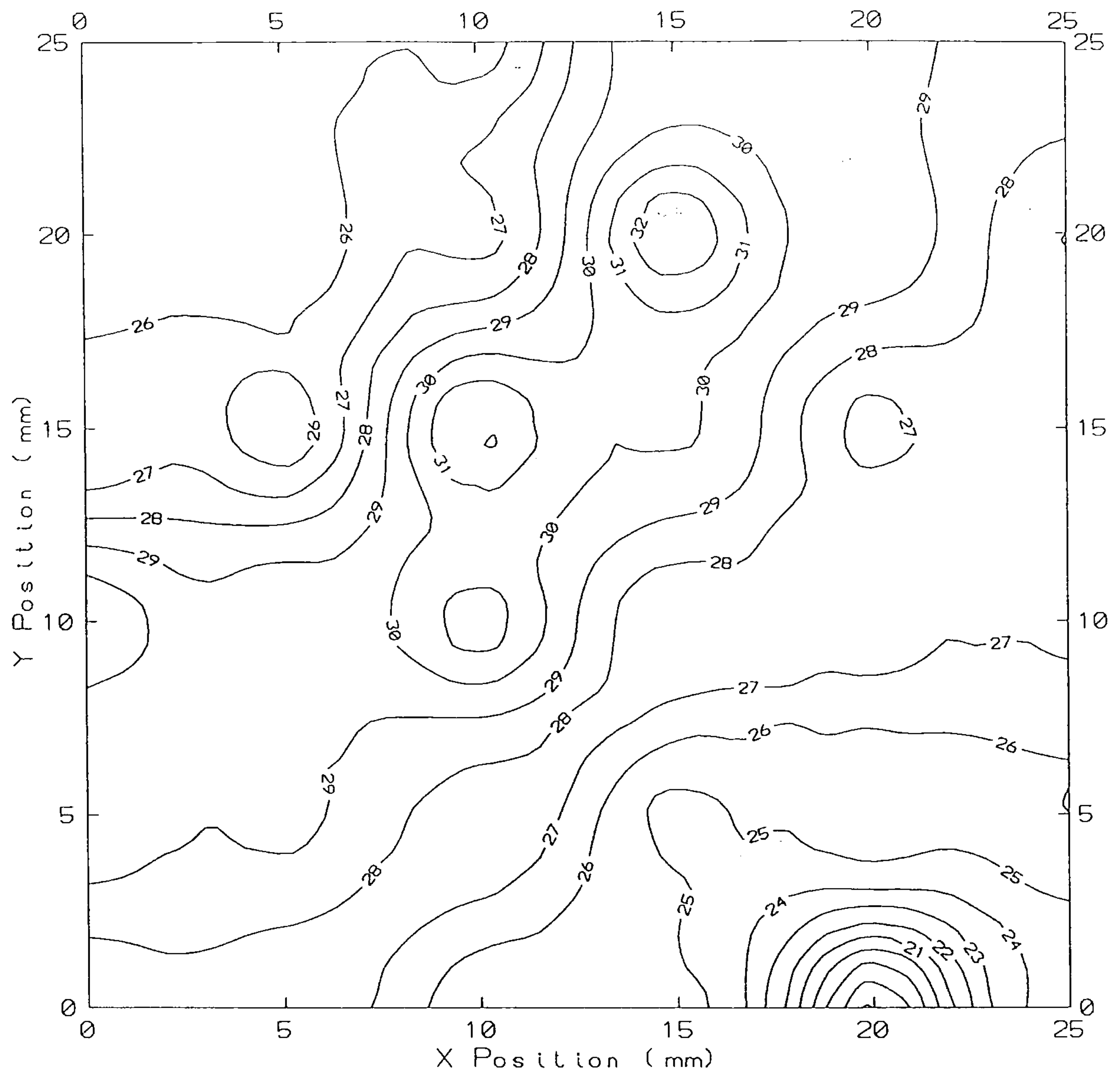

Figure 4.12:
Sample B232. FWHM of the AlGaAs peak.

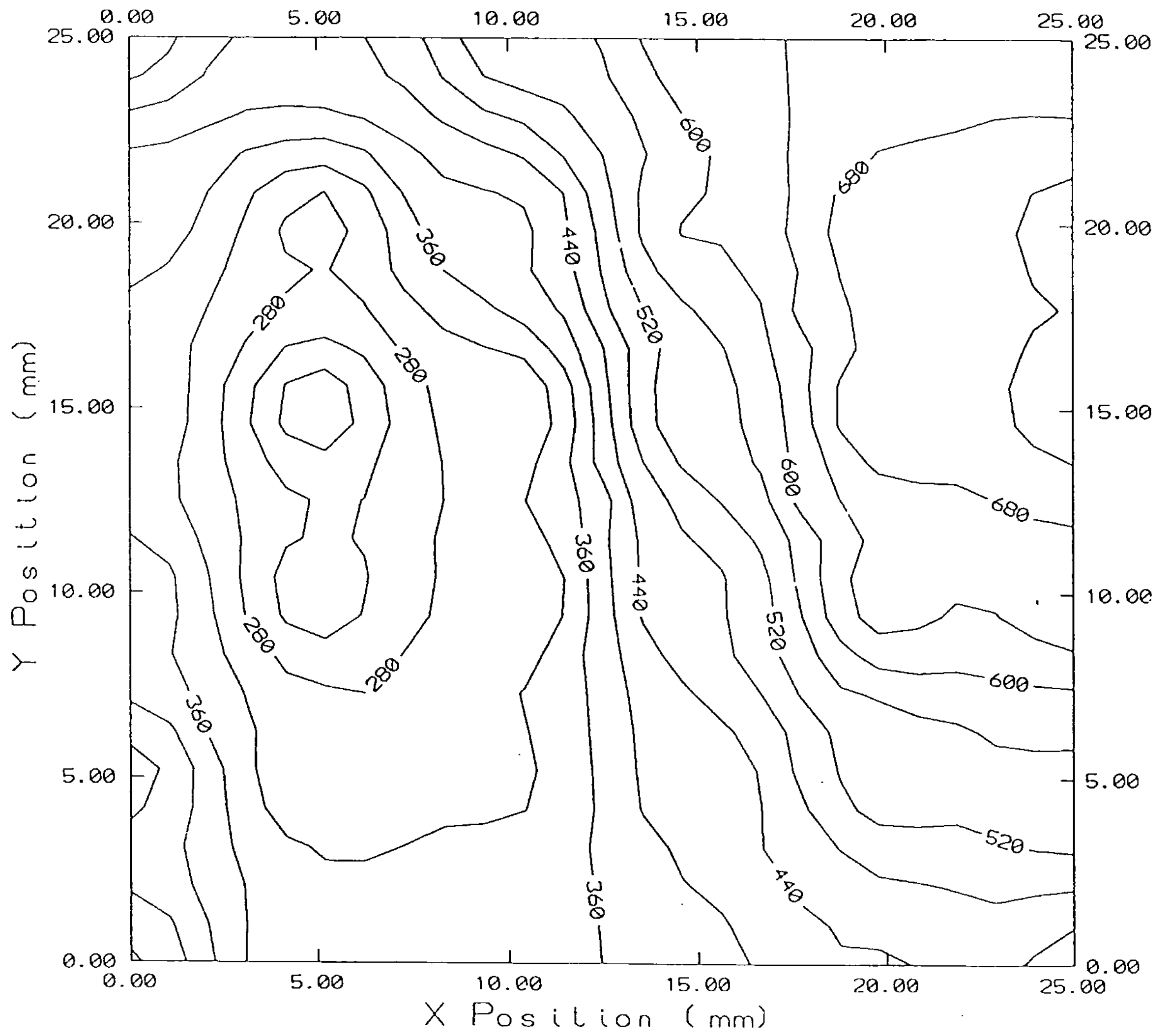

Figure 4.13:
Curvature of the sample B232

Topography

While diffractometer measurements indicated a great uniformity in the separator layer, there was hope that an examination on a bigger area might result in a significant change of the reflectivity. X-ray topography was therefore undertaken at the Synchrotron Radiation Station 7.6 at Daresbury Laboratory of SERC.

We obtained a 333 reflection using a Si(111) crystal as a monochromator. The wavelength, used at this occasion was the same used in the diffractions at the laboratory (λ = 1.541Å). By using Polaroid, we aligned the sample so that the beam struck the sample. That was the point where the only unfortunate event took place during the whole course of the experiments. The computer did not plot points on the screen, so we took the rocking curve by hand. The peak separation between AlGaAs and GaAs was approximately 100arcsec. (At the 004 diffraction in Durham diffractometer it was about 131arcsec.) The slits of the beam were tuned so that the effective cross-section of the resulting beam was finally a rectangle of 40mm$\times$15mm.

For recording the topographs ILFORD L4 plates were used. The exposure time was 10 min and the range of the beam was from 137mA at the first topograph to 123mA at the last one.

The first plate, labelled B231-3 was taken on the AlGaAs peak. Then, in order to have an AlGaAs peak from another part of the sample, we rocked the sample by 45arcsec. This plate was labelled B231-4. In order to take topographs of the GaAs peaks we rocked again the sample in the opposite direction as described in figure 4.14 and recorded the plates B231-6 and B231-7.

Figure 4.14

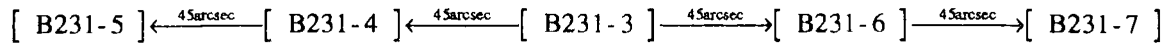

On the area of those plates a two dimensional map has been recorded. This map represents the spatial distribution of the intensity of the diffracted beam. By using a microdensitometer, a rocking curve as from Double Crystal Diffractometry can be taken from the plates. In this experiment the JOYCE-LOEBL 3CS MICRODENSITOMETER was used. Microdensitometry can provide graphical views and measurements of the optical density on photographic films, plates and other transparencies. The principle of the operation is based on a true double-beam light system. These two beams, both produced from a single light source, are switched alternately to a single photomultiplier. When the two beams possess different intensity there is a signal produced by the photomultiplier which, having been amplified, will cause a servo motor to move an optical attenuator, so that the intensity difference will be dropped to zero. As the one beam is scanning the examined plate a continuously null balancing system is obtained. Using the position of the optical attenuator we can record the density at any particular part of a specimen.

The graphs taken from the microdensitometer were very difficult to simulate. Nevertheless, the theoretical peak from a 333 reflection which was taken by using the RADS programme is very similar to the peaks of the microdensitometer graphs. (Figure 4.15)

Our purpose was again to examine GaAs and AlGaAs peaks which have been taken from almost the same area on the sample. Therefore, we examine the plates in pairs. The plate B231-3 contains the reflection of the

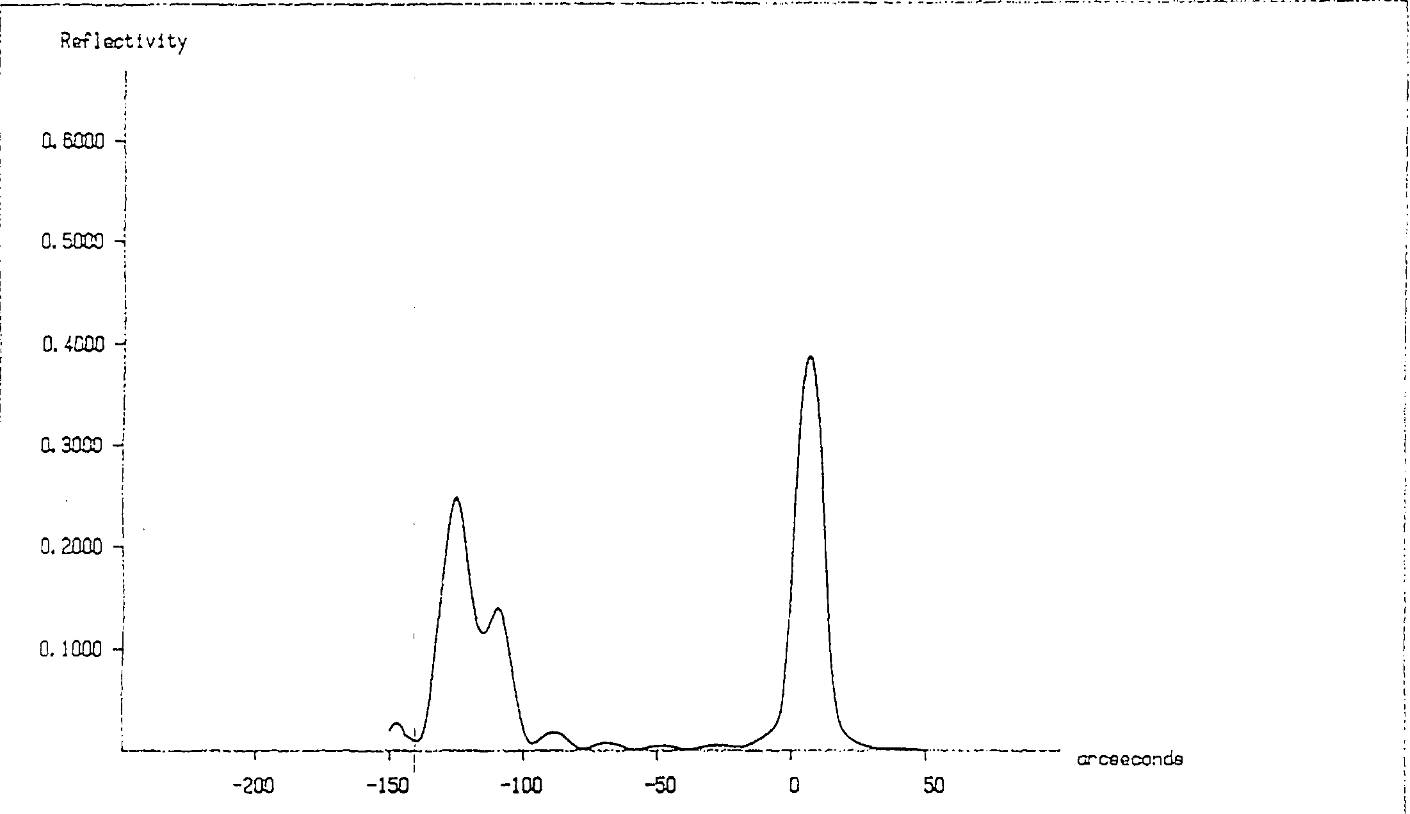

Figure 4.15:
Theoretical peak from a 333 reflection which was taken by using the RADS programme. It is very similar to the peaks of the microdensitometer graphs.

AlGaAs peak. This plate was examined with the B231-7 plate which contains the reflection of the GaAs peak from almost the same area. In the same way, the plates B231-4 and B231-6 contain the peaks of AlGaAs and GaAs from the same area, respectively.

Measurements were done at every 2.5mm on both of the plates of each pair. Great attention has been given to having measurements on the same area of the sample for both of the plates.

In order to avoid the random errors and have a better view of the results, the measurements were recorded using two different sizes of beam (0.2,0.3mm) Unfortunately, the changing of the scanning point of the plate was done manually, and therefore we cannot be sure whether the point, examined with the 0.3mm beam is exactly the same as the one examined with the 0.2mm beam.

The reproducibility of the instrument was fairly good, although there was a slight progressive change in the parameters of the instrument. Thus a continuous checking of the buttons was necessary.

Results from the measurements are presented in Tables 4.4, 4.5, 4.6, 4.7. In the first column, the points where the measurements were taken are indicated with capital letters. The second column, contains the height of the peak from the GaAs. The third and the fifth show the height of the two peaks of AlGaAs indicated "big" and "small", respectively. It is obvious that those numbers represent the relative height of the peaks according to the calibration of the instrument and they do not have an absolute physical meaning. The physical meaning of the measurements can be found in the rest of the columns. In the fourth and the sixth columns are the ratios of the height between the "big" AlGaAs and the GaAs and the "small" AlGaAs and the GaAs, respectively. The last columns represents the ratio between the height of the "small" and the "big" peaks.

Table : 4.4
Sample : B231
Plates : B231-3 , B231-7

Microdensitometer beam size : 0.3 mm

	B231-7	B231-3				0.3mm
		AlGaAs				
Points	GaAs	Big	Big/GaAs	Small	Small/GaAs	Small/Big
A	83	82	0.988	50	0.602	61
B	95	88	0.926	56	0.589	63.6
C	96	102	1.062	59	0.615	57.8
D	104	104	1	65	0.625	62.5
E	115.5	100	0.866	73	0.632	73
F	112.5	-		-	-	-
G	117	100	0.855	64	0.547	64
H	108	85	0.787	63	0.583	74
I	104	91	0.875	64	0.615	70.6
J	111	97	0.874	68.5	0.617	70
K	92	95	1.033	54	0.587	56.8
L	109	85	0.780	59	0.541	69.4
M	81	82	1.012	32	0.395	39
N	89	70	0.787	39	0.438	55.7
O	70	67	0.957	37	0.529	55.2
P	82	82	1	-	-	-

Table : 4.5
Sample : B231
Plates : B231-3 , B231-7

Microdensitometer beam size : 0.2 mm

	B231-7	B231-3				0.2mm
		AlGaAs				
Points	GaAs	**Big**	**Big/GaAs**	**Small**	**Small/GaAs**	**Small/Big**
A	80	82	1.025	52	0.65	63.4
B	86	88	1.023	60	0.698	68.2
C	96	101	1.052	64	0.666	63.4
D	93	106.5	1.145	71	0.763	66.6
E	110	101	0.958	76.5	0.695	74.7
F	105	-	-	-	-	-
G	104	100	0.961	70	0.673	70
H	102	90	0.882	69	0.676	76.6
I	105	93	0.886	71	0.676	76.3
J	105	100	0.952	73	0.695	73
K	88	99	1.125	62	0.705	62.6
L	99	88	0.888	67	0.676	76.1
M	74.5	81	1.087	42	0.564	48.3
N	71	-	-	-	-	-
O	70	74	1.057	46	0.657	62.2
P	77	82	1.065	-	-	-

Table : 4.6
Sample : B231
Plates : B231-6 , B231-4

Microdensitometer beam size : 0.3 mm

	B231-6	B231-4				0.3mm
		AlGaAs				
Points	GaAs	**Big**	**Big/GaAs**	**Small**	**Small/GaAs**	**Small/Big**
A	116	123	1.06	115	0.991	93.5
B	123	120	0.976	111	0.902	92.5
C	112	124	1.107	85	0.759	68.5
D	-	-	-	-	-	-
E	89	107	1.202	64	0.719	60
F	97.5	108	1.108	70	0.718	64.8
G	87	116	1.333	72	0.828	62.1
H	78	112	1.436	66	0.846	58.9
I	70,5	114	1.617	65	0.922	57
J	81	103	1.272	52	0.642	50.5
K	112	115	1.027	66	0.589	57.4
L	99	117	1.182	75	0.757	64.1
M	115	125	1.087	88	0.765	70.4
N	103	-	-	-	-	-

Table : 4.7
Sample : B231
Plates : B231-6 , B231-4
Microdensitometer beam size : 0.2 mm

	B231-6	B231-4				0.2mm
		AlGaAs				
Points	GaAs	**Big**	**Big/GaAs**	**Small**	**Small/GaAs**	**Small/Big**
A	126	132	1.048	127	1.008	96.2
B	128	126	0.984	120	0.937	95.2
C	121	133	1.099	98	0.810	73.7
D	-	-	-	-	-	-
E	97	114	1.175	73	0.753	64
F	106	117	1.104	76	0.717	65
G	98	123.5	1.260	83	0.847	67.2
H	89	117	1.315	70	0.787	60
I	86	122	1.419	70	0.814	57.4
J	89	110	1.236	58	0.652	52.7
K	123	126	1.024	76	0.618	60.3
L	110	126	1.145	85	0.773	67.5
M	122	134	1.098	106	0.869	79.1
N	113	-	-	-	-	-

From the Tables 4.4, 4.5 we drew the following graphs, which clearly represent all the results of the whole experiment. Figure 4.16 shows the relative height of the GaAs peak at the corresponding spatial points (Plate B231-7). Figure 4.17 represents the equivalent height from the "Big" and "Small" components of the AlGaAs peak from the plate B231-3. For all the graphs there are two curves. One for the 0.2mm size of the microdensitometer beam and another one for the 0.3mm. The ratios between the height of the AlGaAs branches peak and the height of the GaAs (fourth and sixth columns, Tables 4.4, 4.5) are presented in figure 4.18. Finally the ratio between the "Big" and the "Small" components (last column Tables 4.4, 4.5) are also represented in figure 4.19.

It obvious that the shape of the GaAs curve is almost the same as that of the AlGaAs curves. This shows that the small variations in the curves have nothing to do with the change of the thickness of the separator layer (InGaAs) but are related to other defects in the structure of the sample. Also from figure 4.19 it is obvious that the reflectivity between the two parts of the AlGaAs is very stable.

For the pair of plates B231-4 and B231-6 (Tables 4.6, 4.7) we drew the graphs of the figure 4.20 and 4.21. The first one represents the relative height of the GaAs peak (Plate B231-6) and the second one the height of the two parts of the AlGaAs peak (Plate B231-4) The topographs of these plates were taken from the edge of the sample. It was not surprising that in this area of the sample there were more defects. Also the figure 4.20 (GaAs height) shows that the quality of the sample in this area must not be satisfactory. Furthermore from the shape of the line on the B231-6,B231-4 plates we can understand that the measurements taken from below the "L" point cannot be trusted. The curve for the ratio between the height of the AlGaAs branches and the GaAs peak (fourth and sixth column Tables 4.6, 4.7) has many variations (Figure 4.22)

The most valuable results can been taken from the last figure ; the ratio between the height of the two parts of the AlGaAs peak, figure 4.23. This line is not as stable as the one in the figure 4.19. The difference of the ratios between the points "A" and "B" and the rest is the only trace we have that reveals a change of the reflectivity between the two branches of the AlGaAs peak.

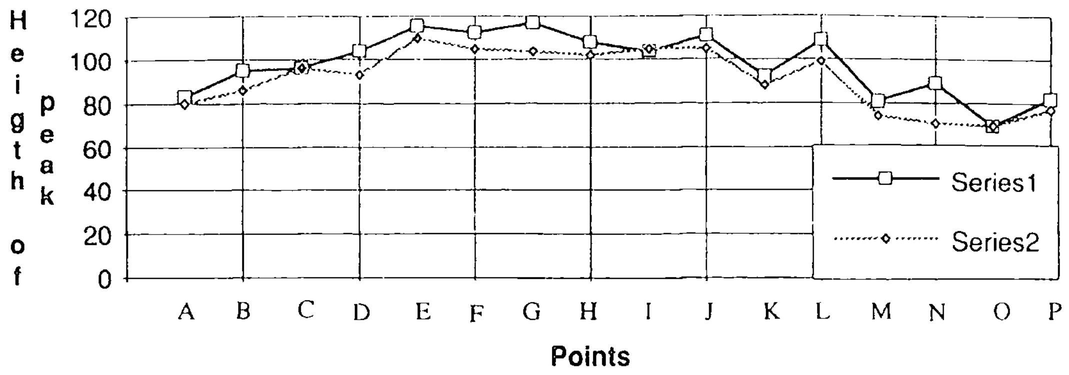

Figure 4.16
Series1: 0.3 mm beam diameter
Series2: 0.2 mm beam diameter

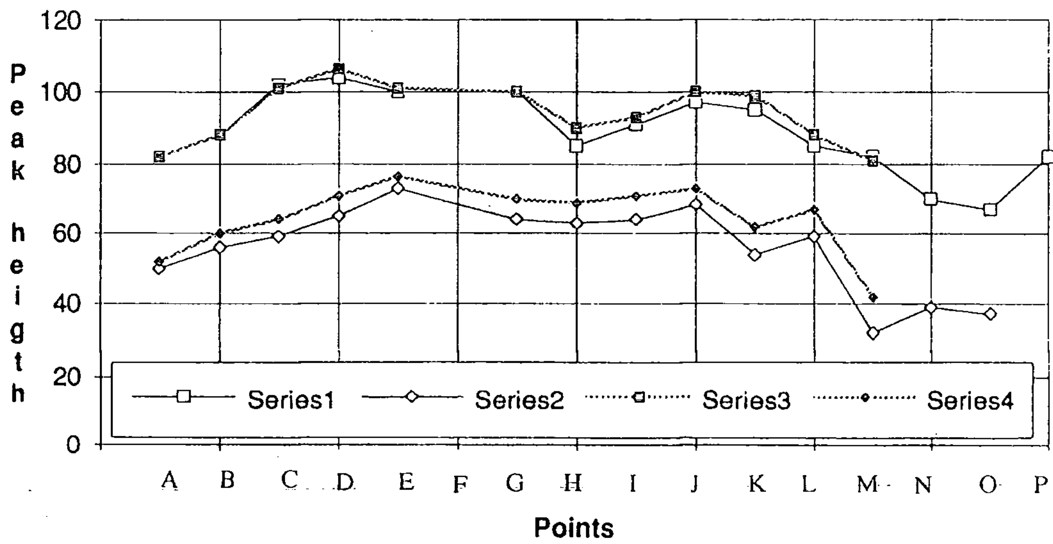

Figure 4.17

0.3mm beam diameter	Series1 "Big" branch	Series2 "Small" branch
0.2mm beam diameter	Series3 "Big" branch	Series4 "Small" branch

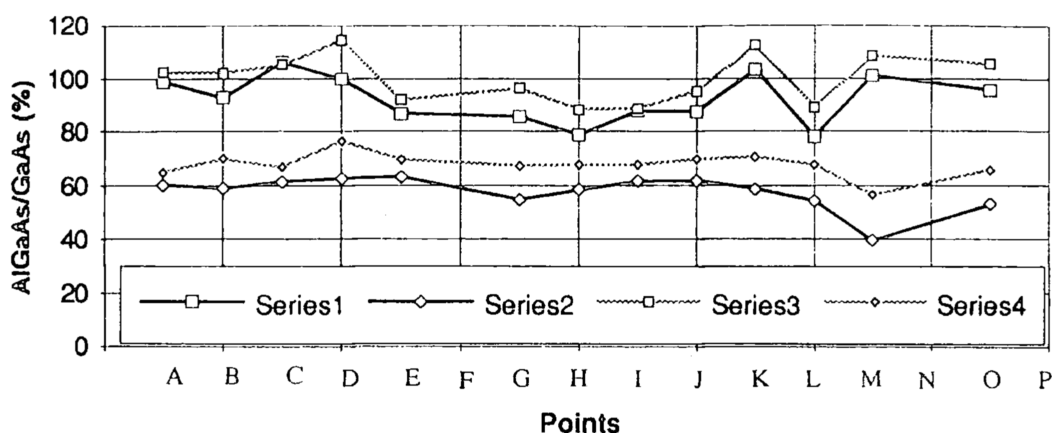

Figure 4.18

0.3mm beam diameter	Series1 "Big" branch	Series2 "Small" branch
0.2mm beam diameter	Series3 "Big" branch	Series4 "Small" branch

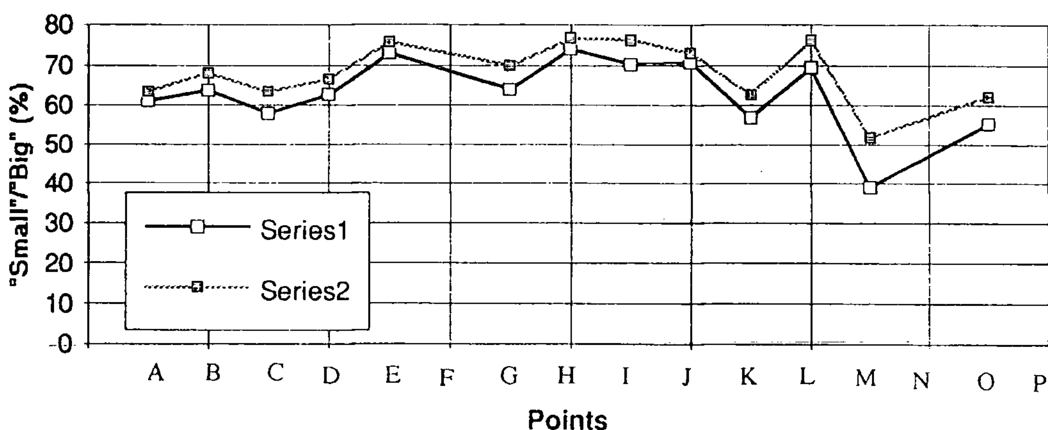

Figure 4.19

Series1: 0.3 mm beam diameter

Series2: 0.2 mm beam diameter

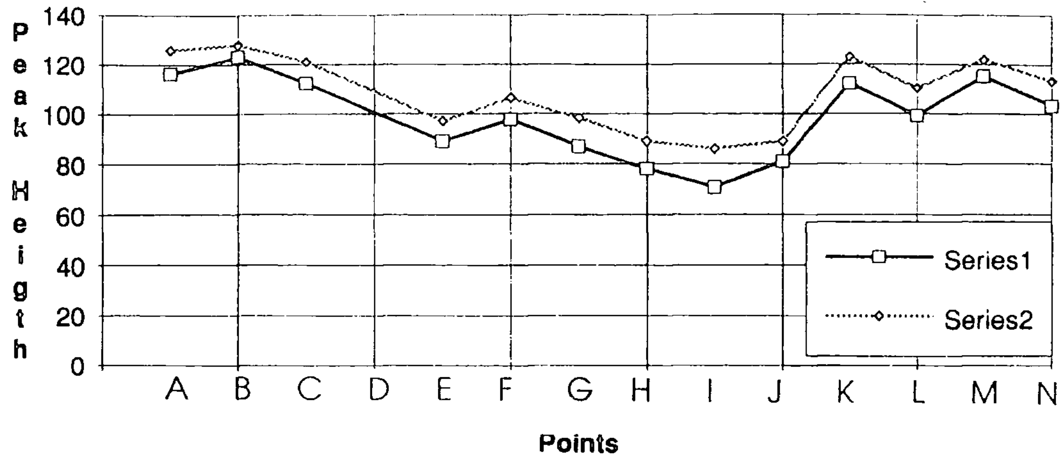

Figure 4.20
Series1: 0.3 mm beam diameter
Series2: 0.2 mm beam diameter

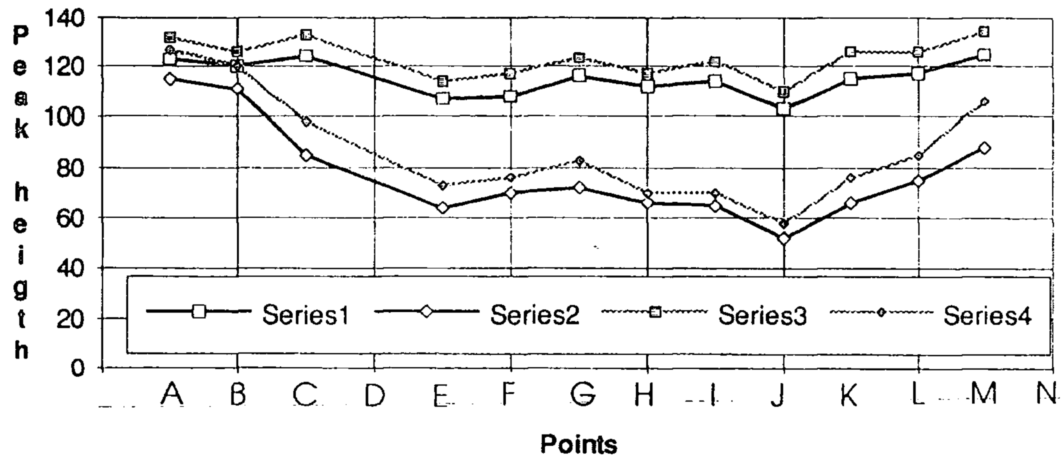

Figure 4.21

0.3mm beam diameter	Series1 "Big" branch	Series2 "Small" branch
0.2mm beam diameter	Series3 "Big" branch	Series4 "Small" branch

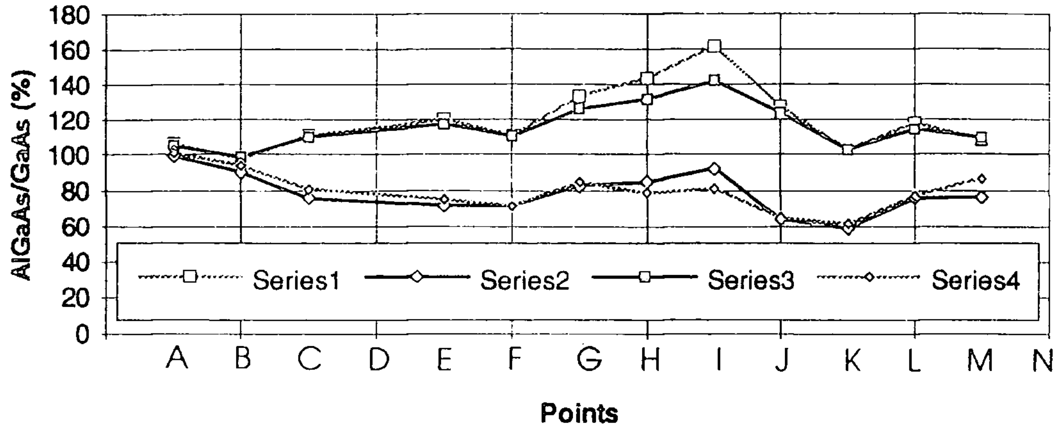

Figure 4.22

0.3mm beam diameter	Series1 "Big" branch	Series2 "Small" branch
0.2mm beam diameter	Series3 "Big" branch	Series4 "Small" branch

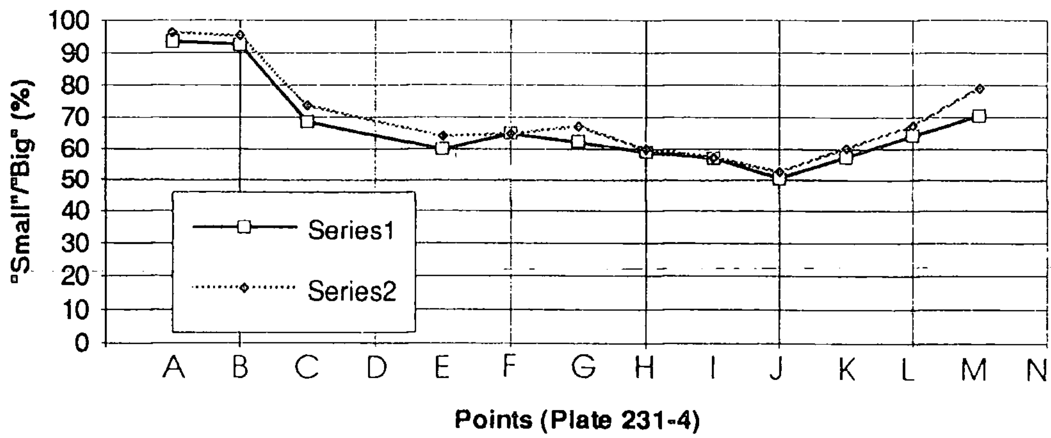

Figure 4.23
Series1: 0.3 mm beam diameter
Series2: 0.2 mm beam diameter

Conclusions and suggestions for further work

Through the theoretical and the experimental work described in the previous pages we were able to see some of the major applications of X-ray diffraction and topography methods for the characterisation of semiconductors. It was shown that recently there have been developed techniques which can provide extremely high resolution measurements.

The reliability of the diffractometer was verified and the results were more than satisfactory. In the analysis of the measurements, simulation programs based on the Dynamical Theory are the most accurate. In this project, by using the RADS program, the fit between the experimental and the simulation rocking curves was excellent.

From the literature research as well as from the experimental results it was found that for the characterisation of an ABA structure device, X-ray diffraction methods are very powerful tools.

The experiments in this thesis were based on a theoretical prediction of dynamical theory. According to this prediction, High Resolution X-ray Diffraction is capable of thickness measurements of monolayer precision. From the discussion during the presentation of the experimental results in chapter 4 we can highlight the following conclusions.

Firstly, the peak splitting at the AlGaAs peak is clear and the structure of the sample agrees with the structure of the theoretical model. By scanning point to point, we detect a rather little variation in the thickness and composition of the layers. In a way, it is unfortunate that the MBE Research Group of University of Glasgow did an "excellent job". The thickness of the separator was extremely uniform and thus no significant changes of the diffraction pattern appeared. However on the other hand, this shows that the separator layer thickness varied by less than half a monolayer atomic spacing across the wafer. The accuracy of the dynamical theory predictions on such a scale of structure makes, of course, the above estimation a time consuming procedure and gives the results a significant uncertainty. In any case it is a remarkable achievement.

In more detail, at the sample B231 we detected that the thickness of the layers of $Al_xGa_{1-x}As$ varied from 0.95 to 0.96 μm with a precision of 0.005 μm and the composition was very constant: 31.5±0.5% Al. The separator layer $In_xGa_{1-x}As$ contained 21.75±0.1% In and its thickness varied less than a monolayer. At the points with the greatest difference (B231×58 and B231× 78) the thickness of the separator differed about 4Å at the worst of the cases (Table 4.1). The thickness of the GaAs layers was constant 22.65Å≅4ML within 0.1Å. Finally, the quality of the substrate did not vary substantially and the sample curvature was found to be very low.

The sample B232 appeared without interference fringes at the rocking curves in one third of its points. At the points of B232, where an interference phenomenon appeared, the rocking curves were similar to the rocking curves from the B231 sample. The separator layer InGaAs was again very uniform. The range of the thickness variation of this layer was less than half a monolayer (1.85-2nm)(Table 4.2) and the composition was again 21.75±0.1% In. The layer of $Al_xGa_{1-x}As$ varied from 0.94-0.97μm with a precision of 0.005μm. The thickness of the two layers of GaAs, that were highly uniform

at the B231 sample, varied from 0 to 3ML in B232. The lack of interference fringes in one third of the points on the sample, could have been caused by having layers that were not well defined, and therefore, there were no sharp interfaces between the layers. All those effects can be explained by the variation of the thickness of the GaAs layers. The substrate quality was rather poor and that is also related with the lack of fringes. Finally, the curvature was bigger than the curvature at the sample B231.

Topographs from the B231 sample did not show any serious variation of the thickness of the "separator" layer across the sample, confirming the rocking curve data. The topographic plates were examined by using a microdensitometer and in recording measurements two different sizes of beam (0.2mm, 0.3mm) were used. The results in both cases have consistent trends. Two different sets of plates were examined from different areas of the sample. First set: Plates B231-3, B231-7. (Tables 4.4, 4.5, Figures 4.16, 4.17, 4.18, 4.19) Figure 4.16 shows the relative height of the GaAs peak at the corresponding spatial points. There are only small changes in the absolute peak height which mean good substrate quality and agreement with the rocking curve data. Figure 4.17 represents the equivalent height from the "Big" and "Small" components of the AlGaAs peak. The variations are similar between the two components and similar to the substrate. This indicates that there is no variation at the thickness of the separator but they are related to other defects in the structure of the sample. The above is confirmed in figure 4.18 where the ratios between the height of the AlGaAs branches peak and the height of the GaAs are presented. Also in figure 4.19 (the ratio between the "Big" and the "Small" components) is obvious that the reflectivity between the two parts of AlGaAs is stable. At point M the sample has a defect and so the change beyond that point is dubious.

Second set: Plates B231-4, B231-6. (Tables 4.6, 4.7, Figures 4.20, 4.21, 4.22, 4.23) The topographs of these plates were taken from the edge of the sample,

so measurements taken from below the "L" point cannot be trusted. It was not surprising that in this area of the sample there were more defects. Figure 4.20 (GaAs height) shows that the quality of the sample in this area is not satisfactory. Figure 4.21 presents the relative height of the two parts of the AlGaAs peak. The variation is again similar to the substrate. Finally, figure 4.23 (ratio between the height of the two parts of the AlGaAs peak) does show tentative evidence of a thickness change between the points A, B and the others. If this is confirmed, it is the first time that atomic-layer sensitivity X-ray topography has been reported.

For developing the technique, MOVPE grown samples could be further examined. This technique of growth gives larger variations across the sample. Also samples grown under non-rotation condition, non uniform flux, or offset sources should be further attempted. (Leeds MBE group have successfully grown wedges of CuCo multilayer by MBE. It should be possible)

Following the way of this thesis simulation programs must be used to look for other possible structures of Bragg case interferometers on which to experiment.

Finally Moire topography still seems possible. This experiments have not shown it to be impossible, neither has it proved it is successful.

Reference

Chapter 1

Diffraction

1 B.K.Tanner, 1990, Adv.X-ray Analysis (Plenum), 33:1
2 B.K.Tanner, D.K.Bowen, 1992, Journal of Crystal Growth, 126:1
3 B.K.Tanner, 1989, J. Electrochem. Soc., 136:3438
4 J.DuMond, 1937, Phys. Rev., 52:872
5 J.H.Beanmont, M.Hart, 1974, J. Phys. E : Sci. Inst., 7:823
6 D.K.Bowen, S.T.Davies, 1983, Nucl. Inst. Meth., 208:725
7 W.J.Bartels, 1983, J. Vac. Sci. Technol., B1:338
8 W.J.Bartels, 1986, U.S. Patent No : 4567605
9 A.Iida, K.Kohra, 1979, Phys. Status Solidi (a), 51:533
10 C.A.Lucas, P.D.Hatton, S.Bates, T.W.Ryan, S.Miles, B.K.Tanner, 1988, J. Appl. Phys., 63:1936
11 P.F.Fewster, 1989, J. Appl. Cryst., 22:64
12 P.Zaumseil, U.Winter, F.Cembali, M.Servidof, Z.Sourek, 1987, Phys. Status Solidi (a), 100:95
13 P.D.Hatton,S.Bates, 1987, Semicond. Sci. Technol., 2:241
14 C.A.Lucas, P.D.Hatton, S.Bates, T.W.Ryan, S.Miles, B.K.Tanner, 1988, J. Appl. Phys., 63:1936
15 P.F.Fewster, 1989, Electrochem.Soc.Symp.Proc., 89-5:278
16 P.F.Fewster, 1989, J. Appl. Cryst., 22:64
17 B.M.Paine, 1986, Mater.Res.Soc.Symp.Proc., 69:39
18 B.K.Tanner, 1988, Electrochem.Soc.Symp.Proc., 88-20:133
19 A.Segmuller, 1986, Adv.X-ray Analysis (Plenum), 29:353
20 B.K.Tanner, 1989, J. Electrochem. Soc., 136:3438
21 P.F.Fewster, 1984, J. Appl. Cryst., 17:426
22 S.N.G.Chu, A.T.Macrander, K.E.Strege,W.D.Johnston, 1985, J. Appl. Phys., 57:249
23 M.A.G.Halliwell, M.H.Lyons, S.T.Davey, M.Hockly, C.G.Tuppen, C.J.Gibbings, 1989, Semicond. Sci. Technol., 4:10
24 M.A.G.Halliwell, M.H.Lyons, M.J.Hill, 1984, Journal of Crystal Growth, 68:523
25 I.C.Bassagnana, C.C.Tann, 1989, J. Appl. Cryst., 22:269
26 A.Tanaka, Y.Masa, S.Seto, T.Kawasaki , 1987, Mater.Res.Soc.Symp.Proc., 90:111
27 N.Matsumura, N.Tsubokura, J.Saraie, Y.Yodogawa, 1988, Journal of Crystal Growth, 86:311
28 H.Kim, Y.Kim, M.-S.Kim, S.K.Min, 1988, Journal of Crystal Growth, 92:507
29 E.Yamaguchi, I.Takayasu, T.Minato, M.Kawashim, 1987, J. Appl. Phys., 62:885
30 I.B.Bhat, N.R.Taskar, J.Ayers, K.Patel, S.K.Ghandhi, 1987, Mater. Res. Soc. Symp. Proc., 90:471
31 M.A.G.Halliwell, M.H.Lyons,B.K.Tanner, P.Ilczyszyn, 1983, Journal of Crystal Growth, 10:287

Topograhpy

1 U.Bonse, M.Hart, J.B.Newkirk, 1967, Adv.X-ray Analysis (Plenum), 10:1
2 A.R.Lang, 1970, Modern Diffraction and Imaging Techniques (ed. Amelincks et.al.) p.407 North-Holland,
3 B.J.Isherwood, C.A.Wallance, 1974, Phys. in T echnology, 5:244
4 B.K.Tanner, 1975, X-ray Diffraction and Topography (Pergamon Oxford),
5 B.K.Tanner, D.K.Bowen, 1980, Characterization of Crystal Growth Defects by X-ray Methods (Plenum N.York),
6 C.S.Barrett, 1945, Trans AIME, 161:15
7 W.FBerg, 1931, Naturwissenschaften, 19:391
8 A.R.Lang, 1958, J. Appl. Phys., 29:597
9 A.R.Lang, 1959, Acta Cryst., 12:249
10 L.Gerward,A.Lindegaard Anderson, 1974, Phys. Stat. Sol.(a), 23:537
11 Y.Epelboin, 1985, Mater. Sci. Eng., 73:1
12 K.Haruta, 1965, J. Appl. Phys., 36:1739
13 C.A.Wallance, R.C.C.Ward, 1975, J. Appl. Cryst., 8:281
14 R.E.Green Jr., 1971, Adv.X-ray Analysis (Plenum), 14:311
15 B.K.Tanner, J.K.Cringean, 1987, Prog. Crystal Growth and Charact., 14:403
16 B.K.Tanner, 1990, Jour. of Gryst. Growth, 99:1315
17 U.Bonse, 1962, Direct Observation of Imperfection in Crystals (eds.Newkirk and Wernick, Wiley N.York, p431,
18 W.L.Bond, J.Andrus, 1952, Am. Mineralogist, 37:622
19 U.Bonse, E.Kappler, 1958, Z. Naturforschung, 13a:348
20 M.Hart, 1968, Science Progress.(Oxford), 56:429
21 K.Kohra, H.Hashizume, J.Yoshimura, 1970, Jap. J. Appl. Phys., 9:1099
22 K.Nakayama, H.Hashizume, A.Miyoshi, K.Kikuta, K.Kohra, 1973, Z.Naturforschung, 28a:632
23 K.Kikuta, K.Kohra, 1970, J. Phys. Soc. Japan, 29:1322
24 K.Kikuta, 1971, J. Phys. Soc. Japan, 30:222
25 S.T.Barnett, B.K.Tanner, G.T.Brown, 1985, Mater. Res. Soc Symp. Proc., 41:88
26 S.T.Barnett, G.T.Brown, B.K.Tanner, 1987, Inst. Phys. Conf. Ser., 87:615
27 T.Ishikawa, T.Kitano, J.Matsui, 1987, J. Appl. Cryst., 20:344
28 M.Hart, 1969, Proc. Roy. Soc. A, 309:281
29 J.Bak-Misiuk, J.Gronkowski, J.Hariwig, W.Wierzchowski, 1987, Phys. Stat. Sol.(a), 41:83
30 A.Guinier, J.Tennevin, 1949, Acta Cryst., 2:133
31 T.Tuomi, K.Naukkarinen, P.Rabe, 1974, Phys. Stat. Sol.(a), 25:93

Chapter 2

1 R.W.James, 1948, "Optical Principals of the Diffraction of X-Ray" (Bell London)
2 Z.G.Pinsker, 1978, "Dynamical Scattering of X-Rays in Crystals" (Springer-Verlag, Berlin)
3 W.J.Bartels, 1987, Inst. Phys. Conf. Ser., 87:599
4 L.Tapfer and K.Ploog, 1986, Phys. Rev. B, 33:5565
5 B.K.Tanner, 1975, "X-ray Diffraction Topography" (Pergamon Press, Oxford)

Chapter 3

1 P.F.Fewster, C.J.Curling, 1987, J. Appl. Phys, 62:10
2 B.W.Batterman, G.Hildebrandt, 1968, Acta Cryst. A, 24:150
3 W.T.Stacy, M.M.Jansen, 1974, J. Cryst. Growth, 27:282
4 W.J.Bartels, W.Nijman, 1978, J. Cryst. Growth, 44:518
5 A.T.Macrander, K.E.Strege, 1986, J. Appl. Phys, 59:442
6 U.Bonse, M.Hart, 1965, Appl. Phys. Letts., 7:99
7 T.W.Barbee Jr., J.H.Underwood, 1983, Opt. Comm., 48:161
8 B.K.Tanner, M.A.G.Halliwell, 1988, Semicond. Sci. Tech., 3:967
9 B.K.Tanner, 1993, J. Phys. D : Appl. Phys., 26:A151
10 H.Holloway, 1990, J. Appl. Phys, 67:6229
11 G.S.Green, B.K.Tanner, P.Kightley, 1991, Mat. Res. Soc. Symp. Proc., 208:315
12 J.Hornstra, W.J.Bartels, 1978, J. Cryst. Growth, 44:513
13 X.Chu, B.K.Tanner, 1986, Appl. Phys. Letts., 49:1773
14 M.Goorsky, T.F.Kench, 1991, Mat. Res. Soc. Symp. Proc., 208:237
15 L.Tapfer, K.Ploog, 1989, Phys. Rev. B, 40:9802
16 M.H.Lyons, 1989, J. Cryst. Growth, 96:339
17 A.T.Macrander, S.Lau, K.E.Strege, S.N.G.Chu, 1988, Appl. Phys. Letts., 52:1985
18 X.Chu, B.K.Tanner, 1987, Semicond. Sci. Tech., 2:745
19 S.Cockerton, 1992, Ph.D. Thesis Durham University
20 S.J.Miles, 1989, Ph.D. Thesis Durham University
21 J.M.Hudson, 1993, Ph.D. Thesis Durham University
21 J.M.Hudson, B.K.Tanner, R.Blunt, 1994, Adv.X-ray Analysis (Plenum), 37:

Chapter 4

1 B.K.Tanner, 1993, J. Phys. D : Appl. Phys., 26:A151
2 H.Holloway, 1990, J. Appl. Phys, 67:6229
3 D.K.Bowen, N.Loxley, B.K.Tanner, L.Cooke, M.Capano., 1991, M.R.S. Symp. Proc., 208:113